

**DOCTORAL THESIS**

Modification of the  
Optoelectronic Properties of  
 $\text{Sb}_2\text{Se}_3$  Absorber Material for  
Photovoltaic Applications

Mehmet Ender Uslu

TALLINN UNIVERSITY OF TECHNOLOGY  
DOCTORAL THESIS  
65/2024

**Modification of the Optoelectronic  
Properties of  $\text{Sb}_2\text{Se}_3$  Absorber Material  
for Photovoltaic Applications**

MEHMET ENDER USLU



TALLINN UNIVERSITY OF TECHNOLOGY

School of Engineering

Department of Materials and Environmental Technology

This dissertation was accepted for the defence of the degree 07/11/2024

**Supervisor:**

Prof. Maarja Grossberg-Kuusk  
School of Engineering  
Tallinn University of Technology  
Tallinn, Estonia

**Opponents:**

Dr. Stela Canulescu  
Department of Electrical and Photonics Engineering  
Technical University of Denmark  
Roskilde, Denmark

Prof. Marco Kirm  
Institute of Physics  
University of Tartu  
Tartu, Estonia

**Defence of the thesis:** 16/12/2024, Tallinn

**Declaration:**

Hereby I declare that this doctoral thesis, my original investigation and achievement, submitted for the doctoral degree at Tallinn University of Technology has not been submitted for doctoral or equivalent academic degree.

Mehmet Ender Uslu

-----  
signature



European Union  
European Regional  
Development Fund



Investing  
in your future

Copyright: Mehmet Ender Uslu, 2024

ISSN 2585-6898 (publication)

ISBN 978-9916-80-229-8 (publication)

ISSN 2585-6901 (PDF)

ISBN 978-9916-80-230-4 (PDF)

DOI <https://doi.org/10.23658/taltech.65/2024>

Printed by Koopia Niini & Rauam

Uslu, M. E. (2024). *Modification of the Optoelectronic Properties of Sb<sub>2</sub>Se<sub>3</sub> Absorber Material for Photovoltaic Applications* [TalTech Press]. <https://doi.org/10.23658/taltech.65/2024>

TALLINNA TEHNIKAÜLIKOOL  
DOKTORITÖÖ  
65/2024

**Päikeseplatari absorbermaterjali  
 $Sb_2Se_3$  optoelektronsete  
omaduste muutmine**

MEHMET ENDER USLU





# Contents

List of publications .....	7
Author's contribution to the publications .....	8
Introduction .....	9
Abbreviations and symbols .....	11
1.1 Photovoltaic solar cell technologies.....	13
1.2 Antimony selenide ( $\text{Sb}_2\text{Se}_3$ ) based thin film solar cell.....	15
1.2.1 Architecture of $\text{Sb}_2\text{Se}_3$ -based thin film solar cell.....	17
1.3 Properties of $\text{Sb}_2\text{Se}_3$ .....	18
1.3.1 Structural properties .....	18
1.3.2 Point defects in $\text{Sb}_2\text{Se}_3$ .....	20
1.3.3 Charge carrier concentration and defect density in $\text{Sb}_2\text{Se}_3$ .....	20
1.4 Deposition of $\text{Sb}_2\text{Se}_3$ thin films.....	21
1.5 Doping strategies in $\text{Sb}_2\text{Se}_3$ .....	24
1.6 Antimony selenosulphide ( $\text{Sb}_2(\text{Se}, \text{S})_3$ ) solar cells .....	24
1.7 Summary of literature review and aim of the study .....	25
2 Experimental .....	27
2.1 Synthesis of $\text{Sb}_2(\text{Se}_{1-x}\text{S}_x)_3$ ( $x = 0-1$ ) polycrystalline materials.....	27
2.2 Sn-doping of $\text{Sb}_2\text{Se}_3$ polycrystalline materials.....	27
2.3 Fabrication of $\text{Sb}_2\text{Se}_3$ thin films by magnetron sputtering and selenization.....	28
2.4 CdS buffer layer and ZnO window layer deposition.....	29
2.5 Applied characterization methods.....	30
2.5.1 Scanning electron microscopy (SEM) and energy dispersive x-ray spectroscopy (EDS).....	30
2.5.2 Micro-Raman spectroscopy .....	30
2.5.3 X-ray diffraction spectroscopy (XRD) .....	30
2.5.4 Ultraviolet-visible spectroscopy (UV-Vis).....	30
2.5.5 X-ray photoelectron spectroscopy (XPS).....	30
2.5.6 Ultraviolet photoelectron spectroscopy (UPS) .....	30
2.5.7 Photoluminescence spectroscopy (PL) .....	31
2.5.8 I-V characteristics and external quantum efficiency (EQE).....	31
3 Results and discussion.....	32
3.1 Optical properties of $\text{Sb}_2(\text{Se}_{1-x}\text{S}_x)_3$ ( $x= 0-1$ ) polycrystalline materials.....	32
3.1.1 Elemental and phase composition of $\text{Sb}_2(\text{Se}_{1-x}\text{S}_x)_3$ polycrystals.....	32
3.1.2 Optical properties of $\text{Sb}_2(\text{Se}_{1-x}\text{S}_x)_3$ polycrystals .....	34
3.2 Electronic band structure of Sn-doped $\text{Sb}_2\text{Se}_3$ polycrystals .....	38
3.2.1 Compositional properties of Sn-doped $\text{Sb}_2\text{Se}_3$ polycrystals.....	38
3.2.2 Electronic band structure of Sn-doped $\text{Sb}_2\text{Se}_3$ by UPS.....	41
3.3 Enhanced control of the grain orientation in $\text{Sb}_2\text{Se}_3$ thin films.....	45
3.3.1 Composition and morphology of the $\text{Sb}_2\text{Se}_3$ thin films.....	45
3.3.2 Grain orientation in the $\text{Sb}_2\text{Se}_3$ thin film .....	49
Conclusions .....	53
References .....	54
Acknowledgements.....	65
Abstract.....	66

Lühikokkuvõte.....	68
Appendix 1 .....	71
Appendix 2 .....	79
Appendix 3 .....	87
Curriculum vitae.....	96
Elulookirjeldus.....	97

## List of publications

The list of author's publications, on the basis of which the thesis has been prepared:

- I **M. E. Uslu**, R. Kondrotas, R. Nedzinskas, O. Volobujeva, K. Timmo, M. Kauk-Kuusik, J. Krustok, M. Grossberg, „Study of the optical properties of  $\text{Sb}_2(\text{Se}_{1-x}\text{S}_x)_3$  ( $x = 0-1$ ) solid solutions”, Material Science in Semiconductor Processing 144 (2022) 106571, <https://doi.org/10.1016/j.mssp.2022.106571>
- II **M. E. Uslu**, M. Danilson, K. Timmo, M. Grossberg-Kuusik, „The effect of tin doping on the band structure and optical properties of polycrystalline antimony selenide”, Physica B: Condensed Matter, 678 (2024) 415744, <https://doi.org/10.1016/j.physb.2024.415744>
- III **M. E. Uslu**, K. Muska, M. Pilvet, S. Bereznev, V. Mikli, M. Kauk-Kuusik, M. Grossberg-Kuusik, „Enhanced grain orientation in  $\text{Sb}_2\text{Se}_3$  thin films deposited on Mo/BSG substrates via RF-sputtering and selenization”, Materials Science in Semiconductor Processing, 184 (2024) 108835, <https://doi.org/10.1016/j.mssp.2024.108835>

## Author's contribution to the publications

Contribution to the papers in this thesis are:

- I The author synthesized the  $\text{Sb}_2(\text{Se}_{1-x}\text{S}_x)_3$  ( $x = 0-1$ ) polycrystals, performed the Raman spectroscopy and photoluminescence spectroscopy measurements and analysis, interpreted the X-ray diffraction (XRD) and scanning electron microscopy/energy dispersive X-ray spectroscopy (SEM/EDX) data, and wrote the paper together with co-authors.
- II The author synthesized the  $\text{Sb}_2\text{Se}_3$  polycrystals and developed the Sn doping process for these polycrystals, performed ultraviolet-visible (UV-Vis) spectroscopy measurements and analysis, analysed the ultraviolet photoelectron spectroscopy (UPS), SEM/EDX, and XRD data, and wrote the paper together with co-authors.
- III The author deposited the Mo back contact layer and Sb thin films by magnetron sputtering and performed the following selenization under different conditions, conducted the Raman spectroscopy measurements and analysis, analysed the XRD and SEM/EDX data. The author performed the current-voltage (I-V) and external quantum efficiency (EQE) measurements on the complete ZnO: Al/CdS/Sb<sub>2</sub>Se<sub>3</sub>/Mo/BSG solar cell devices, and wrote the paper together with co-authors.

## Introduction

Photovoltaics (PV) are recognized as a clean, cost-effective, and sustainable solution for electricity generation, driving the global shift towards solar power. Indeed, solar energetics is the fastest growing renewable energy sector [1]. The installed PV capacity reached 1.6 TW in 2023 [2]. The growing demand for the renewable electricity drives the research and development of new materials and applications of PV. The next generation PV technologies should possess environmentally friendly properties as well enable new applications such as building integrated PV (BIPV), being lightweight, semi-transparent, and mechanically flexible.

Among the emerging PV materials, antimony selenide ( $\text{Sb}_2\text{Se}_3$ ) has emerged as a promising absorber material for thin-film solar cells, thanks to its optimal bandgap for solar energy conversion ( $\sim 1.16$  eV at room temperature) [3], high absorption coefficient ( $> 10^4 \text{ cm}^{-1}$  in the visible spectrum) [4], long minority carrier lifetime ( $\sim 60$  ns) [4], and the fact that its constituent elements are abundant and relatively non-toxic [5]. Therefore,  $\text{Sb}_2\text{Se}_3$  is an attractive material for BIPV enabling semi-transparent thin film PV for window integration, for example. Additionally, the low melting point of  $\text{Sb}_2\text{Se}_3$  of 885 K enables low-temperature deposition, which would allow the reduction of the fabrication costs of thin films for PV [5].

Recent studies have demonstrated power conversion efficiency (PCE) of  $\text{Sb}_2\text{Se}_3$ -based solar cells close to 11% [6][7], with antimony selenosulphide  $\text{Sb}_2(\text{S,Se})_3$ -based PV cells achieving the highest PCEs among the antimony chalcogenides [8].  $\text{Sb}_2\text{Se}_3$ -based PV has shown faster progress in PCE improvement compared to leading chalcogenide PV technologies like  $\text{Cu}(\text{In,Ga})(\text{S,Se})_2$  (CIGSSe) and  $\text{Cu}_2\text{ZnSn}(\text{S,Se})_4$  (CZTSSe) over the past decade [9]. However, the  $\text{Sb}_2\text{Se}_3$  thin film PV technology still faces challenges on the way to high PCE, primarily a significant open-circuit voltage ( $V_{oc}$ ) deficit, which is caused by the recombination of light-induced charge carriers in the bulk of the absorber, at grain boundaries, and at the PV device interfaces [10][11].

Several thin film deposition techniques, such as vapor transport deposition (VTD), rapid thermal evaporation (RTE), close-spaced sublimation (CSS), and magnetron sputtering, have been used to deposit  $\text{Sb}_2\text{Se}_3$  thin films. The crystallinity and the optoelectronic properties of the  $\text{Sb}_2\text{Se}_3$  thin films are significantly influenced by the growth conditions, including substrate type, deposition and post-treatment temperature and the chemical environment. These factors also impact the performance of solar cell device. Despite the progress,  $\text{Sb}_2\text{Se}_3$  solar cells have achieved PCEs of 9.2% [10], 10.12% [7], and 10.57% [6]), which is only about one-third of the theoretically predicted maximum PCE.

$\text{Sb}_2\text{Se}_3$  is a binary inorganic semiconductor with a highly anisotropic quasi-one-dimensional (Q1D) nanoribbon structure composed of  $[\text{Sb}_4\text{Se}_6]_n$  units [12]. These ribbons are structured with covalent bonds but held together by weak van der Waals forces, resulting in anisotropic electrical properties. Moreover, the unit cell of  $\text{Sb}_2\text{Se}_3$  contains 20 atoms, resulting in a complex defect structure related to two distinct Sb atomic sites and three distinct Se atomic sites [13][14]. This makes defect engineering in  $\text{Sb}_2\text{Se}_3$  rather challenging. Additionally, the grain orientation, particularly in the [001] crystallographic direction, where the c-axis of the unit cell is perpendicular to the (001) plane's surface, plays a critical role in enhancing the PCE of  $\text{Sb}_2\text{Se}_3$  solar cells [15].

In recent years, researchers have explored the fundamental properties of  $\text{Sb}_2\text{Se}_3$  and developed several strategies to improve its optoelectronic characteristics as well as the

grain orientation of the  $\text{Sb}_2\text{Se}_3$  thin films in the favoured [001] crystallographic direction. For example, by applying different interlayers, such as seed layers or hole transport layers (HTL), prior to deposition of the  $\text{Sb}_2\text{Se}_3$  absorber layer, improvement in the grain orientation along the [001] direction has been demonstrated, enhancing also the charge carrier transport [16]. To overcome the issue of anisotropic carrier transport and low charge carrier concentration in  $\text{Sb}_2\text{Se}_3$ , several deposition strategies have been tested, such as post-selenization [17], adding 2D  $\text{WS}_2$  interlayer [18], employing  $\text{SnO}_2$  buffer layer [19], and doping with Cl [20]. In addition, Sn-doping has been shown to be efficient to improve the p-type conductivity of  $\text{Sb}_2\text{Se}_3$  [21]. However, there is still a need for a better understanding of the properties of  $\text{Sb}_2\text{Se}_3$ , as well as opportunities to improve its structural and optoelectronic properties, to achieve higher efficiencies with thin film PV devices.

This thesis focuses on the investigation of the structural and optoelectronic properties limiting the PCE of  $\text{Sb}_2\text{Se}_3$  solar cells. This is approached through alloying and doping strategies of  $\text{Sb}_2\text{Se}_3$  polycrystalline materials, and through developing a novel fabrication approach for high-quality  $\text{Sb}_2\text{Se}_3$  thin films for solar cell applications. Namely, the changes in the optical properties of  $\text{Sb}_2\text{Se}_3$  polycrystalline material upon sulphur alloying e.g. the  $\text{Sb}_2(\text{Se}_{1-x}\text{S}_x)_3$  solid solutions with  $x$  changing from 0 to 1, are investigated for the first time by temperature and power dependent photoluminescence spectroscopy (PL). The effect of Sn-doping on the electronic structure of  $\text{Sb}_2\text{Se}_3$  polycrystals is investigated using the ultraviolet photoelectron spectroscopy (UPS) providing new insights into the impact of Sn-doping. Last but not least, a controllable method for depositing  $\text{Sb}_2\text{Se}_3$  thin films with highly oriented grains along the c-axis and a compact morphology is developed combining the magnetron sputtering with post-deposition isothermal selenization.

In this thesis, the first chapter provides a relevant literature review, which establishes the basis for the thesis objectives. The second chapter describes the experimental methods applied for the materials and device fabrication, along with their characterization. The third chapter presents the results and discussion of three studies conducted within the scope of this thesis including the study of the optical properties of  $\text{Sb}_2(\text{Se}_{1-x}\text{S}_x)_3$  ( $x = 0-1$ ) solid solutions, the effect of Sn-doping on the band structure and optical properties of polycrystalline  $\text{Sb}_2\text{Se}_3$ , and the development of a controllable fabrication method for  $\text{Sb}_2\text{Se}_3$  thin films with enhanced grain orientation. The thesis is based on three peer-reviewed publications.

## Abbreviations and symbols

AS	Admittance spectroscopy
AZO	Aluminium doped zinc oxide
BIPV	Building integrated photovoltaics
BSG	Borosilicate glass
CBM	Conduction band minimum
CBD	Chemical bath deposition
C-V	Capacitance-voltage
CSS	Close space sublimation
CZ-TA	(9-octylcarbazole-1,3,6,8-tetrayl) tetrakis(N,N-bis(4-methoxyphenyl)aniline)
CZTS	Copper zinc tin sulphide
DA	Deep acceptor
DAP	Donor-acceptor pair
DD	Deep donor
DFT	Density functional theory
DLTS	Deep level transient spectroscopy
DLCP	Deep level capacitance profiling
$E_a$	Activation energy
EDS	Energy dispersive X-ray spectroscopy
$E_g$	Bandgap energy
$E_c$	Conduction band energy
$E_f$	Fermi energy
$E_{ph}$	Phonon energy
$E_v$	Valence band energy
EHP	Electron-hole pairs
EQE	External quantum efficiency
ETL	Electron transport layer
FF	Fill factor
FTO	Fluorine doped tin oxide
FWHM	Full width at half maximum
CIGSSe	Copper indium gallium selenosulphide
HTL	Hole transport layer
ITO	Indium tin oxide
I-V	Current-voltage
IVD	Injected vapor deposition
$J_{sc}$	Short-circuit current density
LO	Longitudinal optical
P	Power
PV	Photovoltaic

PCE	Power conversion efficiency
PL	Photoluminescence
PLD	Pulsed laser deposition
Q1D	Quasi-one-dimensional
RF	Radio frequency
RT	Room temperature
RTE	Rapid thermal evaporation
S	Huang-Rhys factor
sccm	standard cubic centimetres per minute
Spiro-OMeTAD	$C_{81}H_{68}N_4O_8$
T	Temperature
TAS	Thermal admittance spectroscopy
UPS	Ultraviolet photoelectron spectroscopy
$V_{oc}$	Open-circuit voltage
VBM	Valence band maximum
VTD	Vapor transport deposition
XPS	X-ray photoelectron spectroscopy
XRD	X-ray diffraction
Å	Angstrom = $10^{-10}$ meters
$\alpha$	Absorption coefficient
$\lambda$	Wavelength
$\Phi$	Work function
$\mu_h$	Hole mobility
$\mu_e$	Electron mobility
2D	Two-dimensional

# 1. Literature review

## 1.1 Photovoltaic solar cell technologies

Solar energetics is the main growing renewable energy sector [1]. The globally installed PV capacity reached 1.6 TW in 2023 [2]. Photovoltaic (PV) solar cells as the cornerstone of solar energetics enable direct conversion of sunlight into electricity. Photovoltaics represent a clean, affordable, and sustainable source for electricity generation, making the world to increasingly turn to solar power as a key renewable energy source. These solar cells, based on a light-absorbing semiconductor absorber material, operate by initiating the induction of electron-hole pairs (EHP) upon exposure to sunlight. This phenomenon, known as the photoelectric effect, sets in motion the flow of an external current through the load. The resulting output power is a direct consequence of this photoelectric current flow propelled by the internally generated photoelectric field. To ensure optimal photon absorption, the energy of the incident photons must exceed the bandgap energy threshold of the semiconducting photo absorber material. Optimal absorber band gap together with the optimized optoelectronic and structural properties of the absorber and other constituent materials in the solar cell device combined with the optimal band alignment enables efficient conversion of solar energy into usable electrical power.

The first conventional photovoltaic solar cells were produced in the 1950s. Namely, the first silicon (Si) solar cell with a PCE of 6% was demonstrated by Bell laboratories in 1954 [22]. To date, there are three generations of PV technologies, the first one being based on a few hundred micrometers thick mono- and polycrystalline Si absorbers, which rely on wafer technologies with high material and energy consumption. First generation solar cells reach power conversion efficiencies close to the single-junction Shockley-Queisser limit [23]. In contrast, second-generation solar cells, exemplified by thin-film solar cell technologies, aim to offer a more cost-effective alternative. As the name refers, these solar cells are constructed using successively a few micrometers thin layers deposited onto substrate, leading to significantly reduced material consumption, but slightly lower device efficiencies compared to the silicon PV. The third generation includes emerging PV technologies targeting high efficiency, low cost, and advanced concepts enabling versatile PV applications, and efficiencies beyond single-junction limit.

The global installed PV capacity has surpassed 1 TW<sub>dc</sub>, accounting for nearly 5% of total global electricity generation in 2022 [24]. In 2023 alone, 447 GW of PV installations were added to the global capacity [25]. Currently, the PV market is overwhelmingly dominated by crystalline silicon (c-Si) technology, which commands a substantial market share of approximately 95% [26]. The remarkable efficiency growth (record efficiency 26.8% [27]) and a concurrent decline in manufacturing costs of c-Si modules have led to a significant reduction in wholesale module prices, descending to as low as US\$ 0.14/W<sub>dc</sub> in 2023 as reported by National Renewable Energy Laboratory (NREL) in Fall 2023 Solar Industry Update [28]. However, to meet the growing demand for PV electricity, a selection of PV technologies enabling versatile applications is expected on the market. To compete effectively with c-Si and capture a larger market share, alternative PV technologies must demonstrate superior pricing or efficiency metrics while maintaining comparable lifetimes.

Mature thin-film technologies, such as cadmium telluride (CdTe) with PCE of 22.1% [29] and copper indium gallium selenosulphide (CIGSs) with record PCE of 23.6% [30], along with emerging perovskite thin film solar cells boasting a record PCE of 26.9% [31], and perovskite/silicon tandem cells demonstrating a PCE of 34.6% [32], are currently the most competitive technologies in terms of cost-efficiency. However, challenges remain, particularly regarding component toxicity in CdTe, element scarcity in CIGSs, and stability issues in perovskite technologies. On the other hand, III-V semiconductor materials, including gallium arsenide (GaAs) and indium phosphide (InP), exhibit impressive PCEs of 29.1% [33] and 24.2% [34], respectively, but encounter limitations in scalability and cost-effectiveness. Despite several challenges, ongoing advancements in emerging PV technologies, such as perovskite, kesterite, organic, and quantum dot solar cells, present significant growth opportunities for the industry. Perovskite solar cells, in particular, have experienced significant efficiency improvements over the past decade. Perovskite based tandem solar cells can compete with even the more expensive III-V multijunction solar cells. However, challenges related to chemical stability remain substantial barriers to their widespread adoption.

Overall, the PV landscape is evolving rapidly, driven by innovation and technological advancements. Continued research and development efforts hold the promise of unlocking further breakthroughs and driving the solar energy industry towards a more sustainable and efficient future. As the PV landscape continues to evolve, the pursuit of higher efficiencies, lower costs, and enhanced sustainability remains at the forefront of research and development efforts. The trends over decades and the current advancements in PCE in PV technologies are illustrated in Figure 1, based on the absorber materials used, as reported by NREL [35]. Innovations in materials science, device engineering, and manufacturing processes promise to accelerate the transition to a renewable energy future, with solar power playing a pivotal role in addressing global energy challenges.

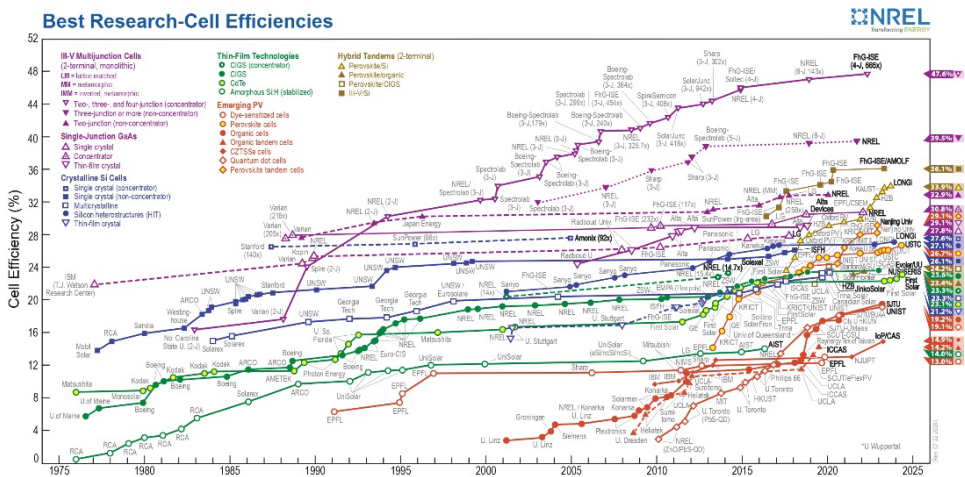


**Figure 1.** The NREL chart of the highest confirmed power conversion efficiencies of research cells for a range of photovoltaic technologies, plotted from 1976 to the present [35].

## 1.2 Antimony selenide ( $\text{Sb}_2\text{Se}_3$ ) based thin film solar cell

In this context, antimony selenide ( $\text{Sb}_2\text{Se}_3$ ) has emerged as a prospective absorber material for thin-film solar cells due to its unique properties.  $\text{Sb}_2\text{Se}_3$  is an inorganic binary semiconductor compound from the V2-VI3 group, characterized by its highly anisotropic properties stemming from its quasi-one-dimensional (Q1D) nanoribbon structure.  $\text{Sb}_2\text{Se}_3$  displays a Q1D structure composed of  $[\text{Sb}_4\text{Se}_6]_n$  ribbons, where ribbons are held together by weak van der Waals forces, while the Sb–Se atoms within the ribbons are covalently bonded. As an emerging absorber material,  $\text{Sb}_2\text{Se}_3$  offers several advantages over the other chalcogenide thin film PV technologies, including low toxicity, abundance of constituent elements, optimal bandgap energy for solar energy conversion (around 1.16 eV at room temperature [3][12]), a high absorption coefficient exceeding  $10^4 \text{ cm}^{-1}$  at visible wavelengths, and a long minority carrier lifetime ( $\approx 60 \text{ ns}$ ) [4]. Moreover,  $\text{Sb}_2\text{Se}_3$  has a low melting point of 885 K and a high vapor pressure ( $> 10^3 \text{ Pa}$  at 723 K [5]) allowing the material deposition at low temperature leading to reduced fabrication cost [36]. In addition, antimony selenide has a single-phase orthorhombic crystal structure without any stable secondary phases, and the stoichiometric deviations manifest as defect levels [37]. Recent advancements have yielded promising results in  $\text{Sb}_2\text{Se}_3$ -based thin film solar cells, with PCEs approaching 11% [6][7], which antimony selenosulphide ( $\text{Sb}_2(\text{S}, \text{Se})_3$ )-based solar cell already achieved [8]. In the first ten years of research and development,  $\text{Sb}_2\text{Se}_3$ -based thin film solar cells exhibited a more pronounced increase in PCE compared to CZTSSe and CIGSSe thin film PV technologies, as illustrated in Figure 2 [9][38]. Similarly to kesterite CZTSSe, the efficiency of  $\text{Sb}_2\text{Se}_3$  solar cells remains low primarily due to a significant open-circuit voltage ( $V_{oc}$ ) deficit resulting from the recombination of the light-induced charge carriers in the bulk of the absorber and at the interfaces.

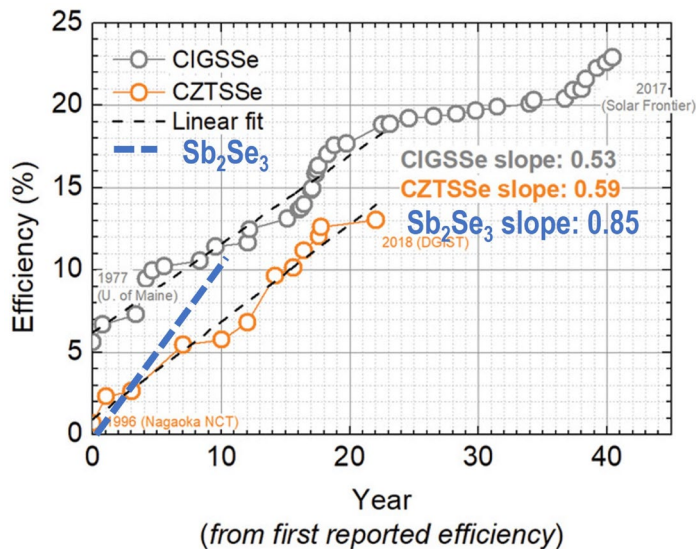


**Figure 2.** Evolution of the power conversion efficiencies of  $\text{Sb}_2\text{Se}_3$ -, CIGSSe-, and CZTSSe-based solar cells, each starting from its respective introduction in the literature by Stefano Rampino et al. [9], and reproduced with further permission from [38] Copyright © 2019, John Wiley & Sons, Inc.

Despite the fast progress in the last decade, three main challenges persist that must be addressed to further enhance the performance of Sb<sub>2</sub>Se<sub>3</sub>-based solar cells. These challenges are:

1. Complex defect chemistry: the unit cell of Sb<sub>2</sub>Se<sub>3</sub> comprises 20 atoms, resulting in a complex defect structure that is not fully understood. Intrinsic defects include point defects on non-equivalent atomic sites of Se and Sb in Sb<sub>2</sub>Se<sub>3</sub> dominated by the cation-replace-anion (Sb<sub>Se</sub>) and anion-replace-cation (Se<sub>Sb</sub>) antisite defects with mid-gap transition levels [39]. These deep defects can act as recombination centers, leading to a reduced carrier lifetime and reduction in the efficiency of photoelectric conversion.
2. Low intrinsic carrier concentration: Sb<sub>2</sub>Se<sub>3</sub> exhibits a relatively low intrinsic carrier concentration of  $1.8 \times 10^{13} \text{ cm}^{-3}$  [40], which is considered insufficient for an efficient photovoltaic absorber material. Introducing extrinsic dopants to the material may help to address this limitation and improve the concentration of charge carriers within the material.
3. Crystal orientation dependant anisotropic electrical properties. The maximum power conversion efficiencies of Sb<sub>2</sub>Se<sub>3</sub>-based solar cells are credited to the increased current density, which stems from the improved alignment of grains in specific crystallographic directions, particularly [221], [211], and most notably [001], due to the 1D ribbon-like grain structure [10]. However, the boundaries between these grains, held together by van der Waals forces, form obstructive spaces that hinder charge carrier transport in the [hk0] directions [11]. As a result, the anisotropic crystal structure is identified as the third limiting factor affecting the energy conversion efficiency of Sb<sub>2</sub>Se<sub>3</sub>-based solar cells.

Addressing these challenges through continued research and development efforts holds the key to unlocking the full potential of Sb<sub>2</sub>Se<sub>3</sub>-based solar cells and further advancing the capabilities of thin-film photovoltaic technology.

Efforts to overcome these challenges are underway through a multifaceted approach that encompasses advanced material characterization, computational modelling, and innovative material and device engineering strategies. By combining these methodologies, researchers aim to gain deeper insights into the complex defect chemistry and intrinsic properties of Sb<sub>2</sub>Se<sub>3</sub> absorber, also determining their impact on the characteristics of the Sb<sub>2</sub>Se<sub>3</sub>-based solar cells. Advanced material characterization techniques, such as SEM, transmission electron microscopy (TEM), XRD, and spectroscopic methods (Raman spectroscopy, PL, XPS, UPS, UV-Vis, etc.), enable to probe the structural, morphological, and optical properties of Sb<sub>2</sub>Se<sub>3</sub> absorber material starting from the nanoscale. These techniques provide valuable information about the distribution and type of defects, electronic structure, crystallographic structure and orientation, and composition of the material, facilitating a better understanding of its behaviour in photovoltaic devices.

In parallel, device engineering strategies focus on optimizing the device architecture, interface engineering, doping and fabrication processes to enhance the performance and stability of Sb<sub>2</sub>Se<sub>3</sub>-based solar cells. Innovations such as interface passivation layers, heterojunction engineering, and defect mitigation techniques are being explored to minimize recombination losses, improve charge carrier transport, and enhance device efficiency. By addressing the challenges of absorber and device structure engineering comprehensively through collaborative research efforts and interdisciplinary approaches, researchers aim to unlock the full potential of Sb<sub>2</sub>Se<sub>3</sub> as a promising absorber material for next-generation thin-film PV.

### 1.2.1 Architecture of $\text{Sb}_2\text{Se}_3$ -based thin film solar cell

Antimony selenide based thin film solar cells have heterojunction architecture with the substrate or the superstrate configuration [7] as shown in Figure 3. In the case of substrate configuration (Figure 3a) a wide band gap ( $E_g \sim 3\text{--}4\text{ eV}$ ) transparent and conductive ZnO:Al (aluminium doped zinc oxide: AZO) is employed as a window layer and front contact, while molybdenum on glass substrate serves as a back conductive layer. Typically, an electron transport layer (ETL) or a buffer layer is employed between the front contact and the  $p$ -type absorber layer for facilitate charge carrier transport and form a  $pn$ -junction with the absorber. CdS is the commonly used  $n$ -type semiconductor for this purpose. In some cases, an additional ultra-thin ( $\sim 20\text{ nm}$ ) intrinsic ZnO ( $i$ -ZnO) layer is used between ZnO:Al and the ETL to prevent a potential aluminium diffusion to the ETL and to improve the band alignment between the  $\text{Sb}_2\text{Se}_3$  absorber and the front contact. Moreover, an additional hole transport layer (HTL) is sometimes used in between the back contact and the absorber layer to enhance the charge carrier transport. In Figure 3b, fluorine doped tin oxide (FTO) or indium tin oxide (ITO) coated conductive transparent glass serves as the window layer and front contact in the solar cell device with superstrate configuration. In the superstrate device architecture, the sequence of the deposition of the constituent layers is the opposite to the substrate configuration, mostly consisting of the same layers.

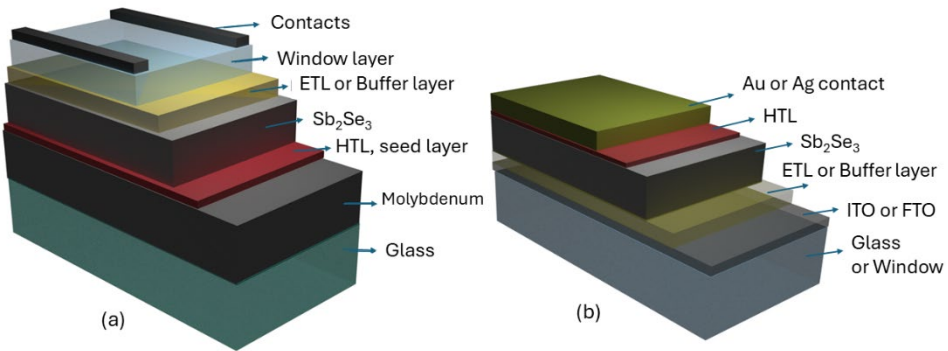


**Figure 3.** Architecture of  $\text{Sb}_2\text{Se}_3$  thin film solar cell as a stack of various functional layers in a) substrate configuration, and b) superstrate configuration. The figures are generated on Blender Software for illustrative purposes.

CdS is extensively used as a buffer layer in  $\text{Sb}_2\text{Se}_3$  solar cells, generating a heterojunction with  $\text{Sb}_2\text{Se}_3$ . Several studies have shown that CdS forms a spike-like band alignment at the conduction band, which is favourable for efficient charge carrier transport in thin film solar cells [41]. However, Tang et al. have found that there is a significant lattice mismatch between CdS and  $\text{Sb}_2\text{Se}_3$ , which was found to lead to a trap-assisted recombination at the  $\text{Sb}_2\text{Se}_3/\text{CdS}$  interface [42]. In addition, interdiffusion of elements between CdS and  $\text{Sb}_2\text{Se}_3$  has been detected. Namely, the interdiffusion of S from CdS into the  $\text{Sb}_2\text{Se}_3$  and Se from the absorber into the CdS buffer was detected, resulting in the formation of  $\text{CdS}_{1-x}\text{Se}_x/\text{Sb}_2\text{Se}_{3-y}\text{S}_y$  alloy at the interface [43]. As contradictory data is available in the literature, it is not clear yet whether this interface modification improves the solar cell device performance or hinders it. Moreover, Cd is a

highly toxic element for the environment and living organisms. Therefore, alternative buffer layer materials such as  $\text{In}_2\text{S}_3$  [44],  $\text{TiO}_2$ , and  $\text{ZnO}$  [45] have been explored. For example, Tang et al. fabricated a  $\text{Sb}_2\text{Se}_3$  solar cell with a PCE of 6% by replacing CdS with  $\text{ZnO}$  deposited by spray pyrolysis [46]. M. Koltsov et al. showed that  $\text{TiO}_2$  stands out as the strongest candidate for replacing the CdS buffer layer in  $\text{Sb}_2\text{Se}_3$ -based solar cells [47]. Recently, Major et al. achieved a record PCE of 8.12% with  $\text{Sb}_2\text{Se}_3$  solar cell by replacing the CdS layer with the  $\text{TiO}_2$  deposited by direct current reactive sputtering [48].

To further enhance charge carrier cultivation by decreasing the recombination of photo-induced electron-hole pairs, utilizing a HTL on the back contact can be essential for  $\text{Sb}_2\text{Se}_3$ -based solar cells. Such an HTL can be a p-type metal oxide, such as  $\text{NiO}_x$  [49],  $\text{WO}_{3-x}$  [50],  $\text{MoS}_3$  [51], or an organic layer [52]. There is still room for the improvement of the front and back interfaces in the  $\text{Sb}_2\text{Se}_3$  thin film solar cell to improve the light-induced charge carrier transport.

## 1.3 Properties of $\text{Sb}_2\text{Se}_3$

### 1.3.1 Structural properties

Although  $\text{Sb}_2\text{Se}_3$  is a single-phase compound with a simple binary chemical composition, its unit cell comprises 20 atoms, leading to a complex and not yet fully understood defect structure. It adopts an orthorhombic crystal structure with space group  $Pnma62$  and lattice parameters  $a = 11.77 \text{ \AA}$ ,  $b = 3.96 \text{ \AA}$ , and  $c = 11.62 \text{ \AA}$  [15]. The ground-state ribbon-like  $\text{Sb}_4\text{Se}_6$  atomic chains in the (a, 0, c) plane, as shown in Figure 4, feature two distinct Sb sites and three distinct Se sites, labelled Sb1, Sb2, and Se1, Se2, Se3, respectively [13][14]. Each atomic site in Figure 4 has a unique chemical bonding environment. When the angle ( $\theta$ ) between the atomic chains and the substrate plane's normal is zero, the c-axis becomes perpendicular to the surface, corresponding to the (001) crystallographic plane [15], as shown in Figure 5. Given the anisotropic crystal structure of  $\text{Sb}_2\text{Se}_3$ , its charge carrier mobilities ( $\mu$ ) possess also anisotropic behaviour. Following electron mobilities in different crystallographic directions at room temperature (RT) are reported  $\mu_{e(020)} = 16.9 \pm 1 \text{ cm}^2/\text{Vs}$ ,  $\mu_{e(120)} = 8.5 \pm 0.6 \text{ cm}^2/\text{Vs}$ ,  $\mu_{e(221)} = 6.2 \pm 0.1 \text{ cm}^2/\text{Vs}$ ; and hole mobilities  $\mu_{h(020)} = 0.69 \text{ cm}^2/\text{Vs}$ ,  $\mu_{h(120)} = 0.81 \text{ cm}^2/\text{Vs}$ ,  $\mu_{h(221)} = 1.21 \text{ cm}^2/\text{Vs}$ ,  $\mu_{h(002)} = 2.59 \text{ cm}^2/\text{Vs}$  [40].

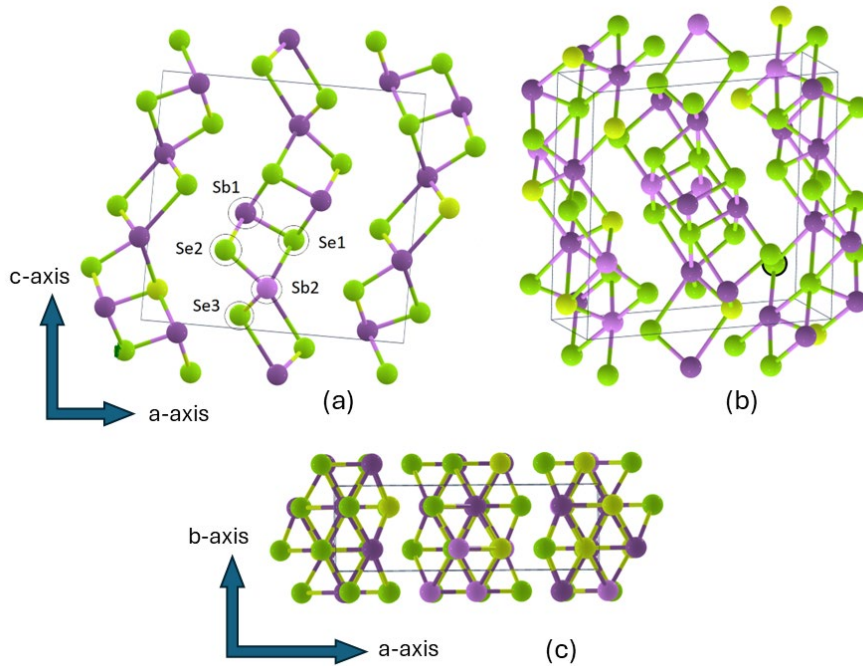


**Figure 4.** a) Ribbon-like crystal structure of  $Sb_2Se_3$ . The non-equivalent Sb and Se atomic sites in an atomic chain are labelled as Sb1, Sb2, and Se1, Se2, and Se3, respectively. The borders of the unit cell are indicated with grey lines. b) 3D model of ground state  $Sb_2Se_3$  unit cell, c)  $Sb_2Se_3$  ribbon view in  $(a, b, 0)$  plane. The figure is adapted from <https://next-gen.materialsproject.org/materials/mp-2160/>.

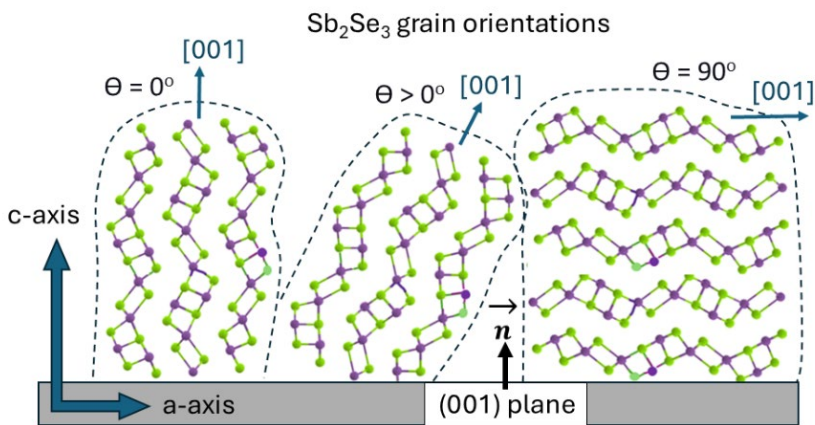


**Figure 5.** A cross-sectional view of  $Sb_2Se_3$  chains stacked together by van der Waals forces represented as three grains grown in different directions regarding the angle ( $\theta$ ) with the  $(001)$  surface plane. The blue dashed lines represent the grain boundaries.

### 1.3.2 Point defects in Sb<sub>2</sub>Se<sub>3</sub>

In a semiconductor, a defect can exist in various charge states by interacting with the electron pool at the Fermi level ( $E_F$ ), and it is essential to calculate and analyse defect formation energies rather than define explicit reactions involving defect pairs [55]. Therefore, computational modelling plays a crucial role in predicting the electronic structure, defect formation energies, and charge carrier transport properties of Sb<sub>2</sub>Se<sub>3</sub>. Density functional theory (DFT) calculations, Monte Carlo simulations, and finite element analysis are employed to simulate the materials properties resulting from different fabrication conditions, providing complementary insights to the experimental studies. In Sb<sub>2</sub>Se<sub>3</sub>, antimony ions can exist in charge states of +5 or +3 with a valence electron configuration of  $5s^25p^3$ . Selenium, in turn, can exhibit oxidation states of +3 and -2, with a valence electron configuration of  $4s^24p^4$ . Ideally, in the absence of defects, Sb1 forms bonds with five neighbouring Se atoms, while Sb2 bonds with three adjacent Se atoms (see Figure 4). According to computational DFT calculations, Sb donates its three  $5p^3$  electrons to neighbouring Se atoms, resulting in unoccupied conduction bands, while hybrid bonds form between Sb-5s states and Se-4p states in the valence band of Sb<sub>2</sub>Se<sub>3</sub> [13]. S. Chen et al. proposed that  $Se_{Sb1}$  and  $Se_{Sb2}$  defect sites carry a charge state of -1, acting as antibonding acceptors near the valence band edge and serving as hole traps [13]. However, Savory et al. suggest that both types of  $Se_{Sb}$  and  $Sb_{Se1}$  sites exhibit amphoteric defects with charge states of +1/-1, potentially acting as recombination centres with mid-band gap transition levels [14]. Building on the findings of Savory et al. [14], T. Chen et al. utilized deep-level transient spectroscopy (DLTS) to demonstrate that  $Sb_{Se}$ , formed in Sb-rich Sb<sub>2</sub>Se<sub>3</sub> acts as an amphoteric defect, capable of trapping both holes and electrons [56]. In addition, T. Chen et al. showed that the Se-rich Sb<sub>2</sub>Se<sub>3</sub> solar cells outperform their Sb-rich counterparts [56]. Depending on the various deposition methods and fabrication conditions of Sb<sub>2</sub>Se<sub>3</sub>, also selenium or antimony vacancies  $V_{Se}$  and  $V_{Sb}$  were found to be amphoteric defects [14][56]. A defect that can trap two charges of the same type, with a higher binding energy for the second one due to overcoming Coulomb repulsion, is named a negative U-center [57]. Walsh et al. suggest based on the DFT calculations that both  $V_{Se}$  and  $V_{Sb}$  can capture or release four electrons, functioning as four-electron negative-U vacancy defects [58]. Grossberg et al. have reported a mid-band gap defect associated with a deep donor – deep acceptor pair recombination experimentally by temperature and power-dependent PL studies on Sb<sub>2</sub>Se<sub>3</sub> [39]. Finally, Walsh et al. found that active Sb-5s lone pairs enable inter-ribbon interactions, potentially leading to stronger chemical binding energies than van der Waals forces [59][60]. Therefore, the defect structure of Sb<sub>2</sub>Se<sub>3</sub> with anisotropic nature is rather complicated and needs better understanding.

### 1.3.3 Charge carrier concentration and defect density in Sb<sub>2</sub>Se<sub>3</sub>

Hall-effect measurements are a reliable method for determining the charge carrier density in thin film semiconductors. Deep-level capacitance profiling (DLCP) and capacitance-voltage (C-V) profiling are powerful tools applied on solar cell devices for determining the defect densities in thin film absorbers. DLCP can screen the bulk defects, while C-V can be responsive to both interface and bulk defects in Sb<sub>2</sub>Se<sub>3</sub>/CdS thin films. Charge carrier densities in the range from  $\sim 10^{13} \text{ cm}^{-3}$  [40] to  $\sim 10^{14} \text{ cm}^{-3}$  [61] are reported in the literature for Sb<sub>2</sub>Se<sub>3</sub>, which is considered low for an optimal photo absorber layer in a thin film solar cell. The low carrier density is linked to a high thin film sheet resistivity around  $10^6 \Omega\text{-cm}$ , resulting in low  $J_{sc}$  values in Sb<sub>2</sub>Se<sub>3</sub>-based solar cells [61]. González et al.

verified the high sheet resistivity of  $10^{16} \Omega \cdot \text{cm}$  in  $\text{Sb}_2\text{Se}_3$  thin film but declared a carrier density of  $\sim 10^{15} \text{ cm}^{-3}$  [62]. Endorsing the  $p$ -type conductivity of  $\text{Sb}_2\text{Se}_3$  thin film prepared by a sputtering process, Cheng et al. reported high deep defect density of  $10^{16} \text{ cm}^{-3}$  and delivered a carrier density of  $\sim 10^{15} \text{ cm}^{-3}$  [63]. On the other hand, T. Chen et al. reported charge carrier density around  $10^{16} \text{ cm}^{-3}$  with a negative Hall coefficient indicating  $n$ -type conductivity of  $\text{Sb}_2\text{Se}_3$  and two kinds of hole traps with densities around  $10^{13} \text{ cm}^{-3}$  [64]. Tang et al. also reported two kinds of hole traps with densities of  $\sim 10^{15} \text{ cm}^{-3}$  and  $\sim 10^{14} \text{ cm}^{-3}$ , respectively, suggesting that the Fermi level is pinned around the defect energy levels due to carrier density lower than defect densities [65]. These hole traps in the middle of the band gap were attributed to  $V_{\text{Sb}}$  and  $\text{Se}_{\text{Sb}}$  [65]. Based on the DFT calculations, Walsh et al. also confirm vacancy and antistites-dominated defects, and rather low density of interstitial defects [66]. The contradicting results about the conductivity type can be attributed to the intrinsic nature of  $\text{Sb}_2\text{Se}_3$  confirmed by the Fermi level position close to the middle of the band gap [65]. Also, different deposition methods of  $\text{Sb}_2\text{Se}_3$  thin films reported in the literature may result in different carrier densities. Table 1 summarizes the defect densities ( $N_T$ ) and their energy levels in  $\text{Sb}_2\text{Se}_3$  reported in the literature.

**Table 1.** Defect densities ( $N_T$ ) and their energy levels in the band gap given as the energetic distance from the valence band ( $E_v$ ) and conduction band ( $E_c$ ) edges in  $\text{Sb}_2\text{Se}_3$ .

Proposed defect type	Energy level (eV)	$N_T$ ( $\text{cm}^{-3}$ )	Method
Undefined defect [40]	$E_v+0.095 \pm 0.008$	$1.3 \times 10^{15}$	TAS
Undefined defect [61]	$E_v+0.42$	$10^{15}$	C-V
Undefined defect [76]	$E_v+0.38$	$2.3 \times 10^{15}$	AS
Undefined defect [61]	$E_v+0.62$	$10^{16}$	C-V
Hole Trap 1 [64]	$E_v+0.55 \pm 0.06$	$(0.23-2.09) \times 10^{13}$	DLTS
Hole Trap 1 [65]	$E_v+0.48 \pm 0.07$	$1.2 \times 10^{15}$	C-V & DLCP
Hole Trap 2 [64]	$E_v+0.66 \pm 0.07$	$(0.07-2.51) \times 10^{13}$	DLTS
Hole Trap 2 [65]	$E_v+0.71 \pm 0.02$	$1.1 \times 10^{14}$	C-V & DLCP
Electron Trap 1 [65]	$E_c-0.61 \pm 0.03$	$2.6 \times 10^{14}$	C-V & DLCP
Electron Trap 1 [7]	$E_c-0.206$	$2.74 \times 10^{14}$	C-V & DLCP
Electron Trap 2 [7]	$E_c-0.569$	$8.02 \times 10^{14}$	C-V & DLCP

## 1.4 Deposition of $\text{Sb}_2\text{Se}_3$ thin films

Antimony selenide exhibits a highly anisotropic crystal structure [15][67], making it challenging to deposit high-quality  $\text{Sb}_2\text{Se}_3$  thin films for solar cell applications, as it promotes anisotropic charge carrier transport [40]. As can be seen in Figure 6, the boundaries between the randomly oriented grains may act as recombination channels due to the active lone pairs (Sb-5s states) of dangling bonds and form inefficient charge carrier paths for the photocurrent in thin film solar cells [60][68]. The literature primarily reports randomly oriented  $\text{Sb}_2\text{Se}_3$  grains on the substrate, with the most effective solar cell devices achieving grain orientation that approach the ideal [001] crystallographic direction. Theoretical approaches suggest that even [221] grain orientation of  $\text{Sb}_2\text{Se}_3$  can cause a loss of power conversion efficiency compared to the [001] orientation with degradation in all the device parameters, not only short current density ( $J_{sc}$ ) but also open circuit voltage ( $V_{oc}$ ), and fill factor ( $FF$ ) [69].

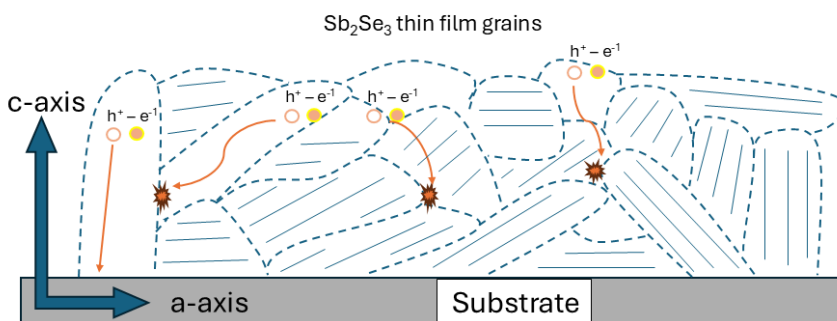


**Figure 6.** Cross-sectional view of randomly oriented  $Sb_2Se_3$  grains on the substrate surface with blue dashed lines representing the grain boundaries, where charge carrier (electron hole pairs:  $h^+e^-$ ) transport is degraded. Orange coloured arrows represent possible charge transport paths.

Various techniques have been employed for depositing  $Sb_2Se_3$  thin films for PV applications, either as single-step or multi-step processes, with or without post-thermal treatment using selenium vapor. The most prominent methods include vapor transport deposition (VTD) [65], rapid thermal evaporation (RTE) [70], close space sublimation (CSS) [10][71], magnetron (RF/DC) sputtering [72][73] and hydrothermal deposition [74]. The VTD method enables independent control of the source and substrate temperatures, using an inert gas flow to efficiently transport vapor flux from the source to the substrate surface. The RTE technique is an advanced thermal evaporation (TE) enabling to achieve a higher deposition rate, whereas the traditional TE typically operates at around  $0.1 \mu\text{m}/\text{min}$  [75]. RTE and CSS methods utilize a short distance between the substrate and the source, along with high vapor pressure, achieving deposition rates of up to  $1 \mu\text{m}/\text{min}$  [75], while the VTD method offers a more adjustable distance, promoting a more uniform gas phase over the substrate [65]. Unlike RTE, the CSS method involves the direct sublimation of the source material without undergoing the melting process. In contrast, magnetron sputtering, and pulsed electron deposition (PED) are physical vapor deposition (PVD) methods that differ from thermally initiated technique. Magnetron sputtering utilizes  $Ar^+$  ions, while PED employs high energy electrons to bombard the source, producing cold plasma that deposits onto the substrate within a high vacuum chamber.

The  $Sb_2Se_3$  thin film solar cells deposited by VTD have achieved a PCE of 7.6% [65]. However, this has recently been surpassed by devices based on  $Sb_2Se_3$  produced through RTE, which demonstrated a PCE of 8.2% using two-step deposition strategy [70]. The CSS method enabled one of the highest PCEs of 9.2% of  $Sb_2Se_3$  solar cell [10]. In addition, solar cells fabricated using DC-magnetron sputtering of Sb followed by rapid thermal evaporation of selenium have achieved a PCE of 3.47% [72]. A solar cell made from RF-magnetron sputtered  $Sb_2Se_3$ , followed by post-thermal selenization, demonstrated a PCE of 6.84% [73]. Another solar cell study, where the  $Sb_2Se_3$  absorber was achieved using a hydrothermal deposition method, reported a PCE of 7.89% [74]. Other methods for depositing  $Sb_2Se_3$  thin films include chemical bath deposition (CBD) [6], and injected vapor deposition (IVD) [7], both of which have resulted in the device efficiencies exceeding 10%. The current record device efficiency for  $Sb_2Se_3$  thin film solar cells, achieved through cost-effective CBD for the absorber deposition, is 10.57% [6]. The PV parameters of efficient  $Sb_2Se_3$  thin film solar cells, which primarily employ a CdS buffer layer, are presented in Table 2 for comparison.

**Table 2.**  $Sb_2Se_3$ -based thin film solar cells fabricated by different deposition methods and their performance parameters in the literature.

Thin film deposition method (with buffer layer or HTL)	$V_{oc}$ (mV)	$J_{sc}$ ( $mA/cm^2$ )	FF (%)	PCE (%)	Reference
VTD (CdS buffer layer)	421	27.8	57.6	6.4	[76]
VTD (CdS buffer layer)	420	29.9	60.4	7.6	[65]
RTE (CdS buffer layer)	400	25.14	55.7	5.6	[77]
RTE (CdS buffer layer)	475	27.7	63.1	8.12	[70]
RTE (ZnO buffer layer)	391	26.2	57.8	5.93	[46]
CSS (CdS buffer layer)	421	28.4	57.1	6.84	[71]
(with CZ-TA HTL)					
CSS (CdS buffer layer)	389	26	55.9	5.64	[71]
CSS (CdS buffer layer)	380	19.5	38	2.82	[61]
CSS (TiO <sub>2</sub> buffer layer)	430	24.6	50	5.28	[61]
CSS (CdS buffer layer)	400	32.58	70	9.2	[10]
CSS (TiO <sub>2</sub> buffer layer)	432	32.5	57.9	8.12	[48]
Magnetron sputtering (CdS buffer layer)	414	16	52	3.47	[72]
Magnetron sputtering (CdS buffer layer)	494	25.91	47.7	6.06	[17]
Magnetron sputtering (CdS buffer layer)	504	24.91	54.47	6.84	[73]
PED (CdS buffer layer)	256	20.28	39.2	2.1	[15]
CBD (CdS buffer layer)	467	33.52	67.64	10.57	[6]
IVD (CdS buffer layer)	488	30.86	67.19	10.12	[7]
Selenization process (CdS buffer layer)	470	31.30	57.3	8.42	[16]
Hydrothermal deposition (CdS buffer layer)	449	28.3	62.1	7.89	[74]

Despite exploration of various deposition methods, achieving high-quality  $Sb_2Se_3$  thin films with grain orientation in the [001] direction and crystallite size that correspond to the grain sizes remain a significant challenge. To address this, several studies have focused on enhancing the crystal quality and controlling the grain orientation by employing additional interlayers between the back contact and the absorber layer. Notable approaches include employing a  $MoSe_2$  interlayer to facilitate the growth of  $Sb_2Se_3$  nanorod arrays [78], growing  $Sb_2Se_3$  nanowires on a two-dimensional (2D)  $WS_2$  monolayer [18], constructing a  $SnO_2/Sb_2Se_3$   $n-p$  heterojunction [19], and applying ultrathin seed layer of  $Sb_2Se_3$  [52][53] or  $Sb_2S_3$  [54] to promote the vertical nucleation of  $Sb_2Se_3$  grains. However, Wen et al. demonstrated that [001]-oriented growth can be adjusted by balancing the kinetic energy of the Se vapour reaching the antimony film (Sb/Mo/Glass) surface: the selenization reaction progresses from the surface downward

along the surface normal (001) because the reaction occurs more rapidly than diffusion once the Se atoms reach the surface of the Sb film [16]. This approach enabled to achieve a PCE of 8.42% of a flexible  $\text{Sb}_2\text{Se}_3$  solar cell [16].

### 1.5 Doping strategies in $\text{Sb}_2\text{Se}_3$

There is a consensus in the literature that  $\text{Sb}_2\text{Se}_3$  exhibits high resistivity due to its low carrier density at RT, and one approach to mitigate this issue is through extrinsic doping. Given the quasi-intrinsic nature of  $\text{Sb}_2\text{Se}_3$  thin films, doping with chlorine (Cl) impurities resulted in n-type conductivity with the carrier density in the range of  $10^{16}$ – $10^{17}$   $\text{cm}^{-3}$  [20]. Tin (Sn) doping has been identified as an effective way to improve the conductivity of  $\text{Sb}_2\text{Se}_3$ . For example, a  $\text{Sb}_2\text{Se}_3$  quasi-homojunction thin film solar cell with configuration of Mo/ $\text{Sb}_2\text{Se}_3$ -Sn/ $\text{Sb}_2\text{Se}_3$ -I/ITO/Ag showed an increase in the carrier density from  $10^{13}$   $\text{cm}^{-3}$  to  $10^{14}$   $\text{cm}^{-3}$  and  $10^{17}$   $\text{cm}^{-3}$  by adding 1% Sn and 10% Sn, respectively, in  $\text{Sb}_2\text{Se}_3$  thin film [79]. While pure  $\text{Sb}_2\text{Se}_3$  crystals were found to exhibit low conductivity at  $2.71 \times 10^{-6}$   $\text{S}\cdot\text{cm}^{-1}$ , Sn-doping significantly enhances the conductivity reaching  $7.50 \times 10^{-2}$   $\text{S}\cdot\text{cm}^{-1}$  at 0.1 % Sn, as well as boosts the charge carrier density to  $2 \times 10^{16}$   $\text{cm}^{-3}$  [21]. Chen et al. suggest that  $\text{Sn}^{4+}$  ions substitute for  $\text{Sb}^{3+}$  in  $\text{Sb}_2\text{Se}_3$  crystals, effectively converting the intrinsic  $\text{Sb}_2\text{Se}_3$  into p-type [21]. Similarly, Patel et al. [80] and Hobson et al. [81] reported enhanced p-type conductivity in Sn-doped  $\text{Sb}_2\text{Se}_3$  crystals, as demonstrated through temperature-dependent resistance and Hall measurements, respectively. In addition to Sn, doping  $\text{Sb}_2\text{Se}_3$  thin films with transition metals such as Fe, Pb, and Cu has been explored. Li et al. explained that Fe-doped  $\text{Sb}_2\text{Se}_3$  thin film shows a slight increase in carrier mobility, with almost no impact on carrier density at RT [82]. Kelvin probe force microscopy and Hall measurements revealed that Fe-doping converts the initially poor p-type  $\text{Sb}_2\text{Se}_3$  thin films to n-type [82].  $\text{PbI}_2$  doping was found to increase the hole concentration in  $\text{Sb}_2\text{Se}_3$  thin film from  $1.6 \times 10^9$  to  $1.7 \times 10^{13}$   $\text{cm}^{-3}$ , although this increase was accompanied by a decrease in mobility [83]. The study suggests that  $\text{Pb}^{2+}$  ions substitute  $\text{Sb}^{3+}$  in the  $\text{Sb}_2\text{Se}_3$  crystal structure [83]. Tang et al. have found that by immersing  $\text{Sb}_2\text{Se}_3$  films in a  $\text{CuCl}_2$  aqueous solution mixed with ammonia at low temperatures promotes the diffusion of  $\text{Cu}^{2+}$  ions along grain boundaries, resulting in an interstitial doping [84]. This was found to reduce nonradiative recombination at the grain boundaries, enhancing carrier collection, and improving the  $V_{oc}$  and  $J_{sc}$  of the  $\text{Sb}_2\text{Se}_3$  solar cell [84].

### 1.6 Antimony selenosulphide ( $\text{Sb}_2(\text{Se}, \text{S})_3$ ) solar cells

Antimony sulphide ( $\text{Sb}_2\text{S}_3$ ) is isomorphous to  $\text{Sb}_2\text{Se}_3$  as both are from the *Pnma62* space group [85]. Antimony sulphide also exhibits a ribbon-like grain structure stacked together by van der Waals forces, like  $\text{Sb}_2\text{Se}_3$ . However, it possesses a wider energy band gap of 1.7–1.8 eV at RT due to the substitution of sulphur atoms for selenium sites, which have smaller ionic radii [86]. Due to the wider band gap,  $\text{Sb}_2\text{S}_3$ -based solar cells show significantly higher values of  $V_{oc}$  reaching up to 700 mV when compared to  $\text{Sb}_2\text{Se}_3$ -based solar cells. However, solar cells based on  $\text{Sb}_2\text{S}_3$ , despite having a similar configuration to those based on  $\text{Sb}_2\text{Se}_3$ , exhibit lower  $J_{sc}$  values [86]. At this point, antimony selenosulfide ( $\text{Sb}_2(\text{Se}, \text{S})_3$ ) solar cells emerge as a solution to optimize the device structure by bridging the properties of  $\text{Sb}_2\text{Se}_3$  and  $\text{Sb}_2\text{S}_3$ , namely tuning the bandgap energy and along with it the  $V_{oc}$  and  $J_{sc}$  of the devices. The VTD method can be employed for the deposition of  $\text{Sb}_2(\text{Se}, \text{S})_3$  thin films for solar cell applications. A basic solar cell configuration of

glass/ITO/CdS/Sb<sub>2</sub>(Se, S)<sub>3</sub> prepared by VTD with a Se/S ratio of 3.0, showed a PCE of 7.6%, along with a  $V_{oc}$  of 485 mV [87]. A double buffer layered glass/FTO/TiO<sub>2</sub>/CdS/Sb<sub>2</sub>(Se, S)<sub>3</sub>/Spiro-OMeTAD/Au solar cell showed a  $V_{oc}$  of 792 mV [88]. Chen et al. demonstrated that a FTO/CdS/Sb<sub>2</sub>(Se, S)<sub>3</sub>/Spiro-OMeTAD/Au solar cell, utilizing Sb<sub>2</sub>(Se, S)<sub>3</sub> deposited via an ethanol (C<sub>2</sub>H<sub>5</sub>OH) assisted hydrothermal method and substituting 30% of Se with S, achieved a record PCE of 10.75 % [89].

However, the changes in the defect structure resulting from alloying Sb<sub>2</sub>Se<sub>3</sub> with S, are rarely studied. Zhang et al. who developed a Sb<sub>2</sub>(S<sub>0.7</sub>Se<sub>0.3</sub>)<sub>3</sub> solar cell with Spiro-OMeTAD and nanoparticle-TiO<sub>2</sub> double buffer layer, demonstrating a PCE of 7.08%, detected two distinct hole traps in the absorber at 0.61 eV and 0.74 eV by DLTS [90]. In another study, Chen et al. also found two different hole traps at 0.52 eV and 0.76 eV, respectively, in a Sb<sub>2</sub>(S, Se)<sub>3</sub> thin film absorber prepared by hydrothermal deposition, using DLTS [91]. Tao et al. suggested a surface post-treatment with potassium iodide (KI) to passivate deep defects in Sb<sub>2</sub>(S, Se)<sub>3</sub> thin films [92].

## 1.7 Summary of literature review and aim of the study

Defects located in the middle of the band gap, identified as hole traps [64][65], pose a significant challenge for Sb<sub>2</sub>Se<sub>3</sub> solar cells, as their large activation energy ( $E_a$ ) limits the contribution of the bulk defects to free charge carrier density to only 2.6% [76]. This effect is evident in the significant difference between the defect density, which is around 10<sup>15</sup> cm<sup>-3</sup>, and the free carrier density at RT, approximately 10<sup>13</sup> cm<sup>-3</sup> [76]. Various doping strategies, including Cl [20], Sn [21], Fe [82], and Pb [83], have been explored to passivate defects acting as recombination centres, and to compensate the low carrier density in Sb<sub>2</sub>Se<sub>3</sub>. Among these, Sn has been identified as the most promising dopant to significantly enhance the p-type conductivity of Sb<sub>2</sub>Se<sub>3</sub>. Alloying with sulphur forming Sb<sub>2</sub>(Se, S)<sub>3</sub> solid solution offers another approach to tune the optoelectronic properties including the band gap energy of Sb<sub>2</sub>Se<sub>3</sub> resulting in the highest device efficiency so far. On the other hand, various deposition methods such as VTD, RTE, CSS, CBD, IVD, and magnetron sputtering, combined with optimized fabrication conditions, have been employed to enhance the quality of the thin film absorbers, including promoting grain orientation in the favoured [001] crystallographic direction.

The variations in solar cell efficiencies, defect densities and charge carrier densities resulting from these deposition techniques (as shown in Table 2) are likely attributable to the highly anisotropic nature of Sb<sub>2</sub>Se<sub>3</sub>. While three different Sb<sub>2</sub>Se<sub>3</sub> solar cells in the literature have reached power conversion efficiencies of 9.2% [10], 10.12% [7], and 10.57% [6], these figures are still insufficient for the commercialization of Sb<sub>2</sub>Se<sub>3</sub> solar cells when considering the levelized cost of energy (LCOE) and in comparison to other thin film technologies, such as CdTe, and CIGSSe. Most other Sb<sub>2</sub>Se<sub>3</sub> solar cells fall short of these three performance levels.

In response, many recent studies have investigated the use of additional interlayers, such as seed layers and organic or metal oxide HTL, applied prior to depositing the Sb<sub>2</sub>Se<sub>3</sub> absorber layer to control grain orientation, aiming for the preferred [001] direction. Two step deposition techniques have improved the preferred grain orientation [001] to some extent [16]. However, the outcomes remain unsatisfactory in achieving higher power conversion efficiencies of Sb<sub>2</sub>Se<sub>3</sub> solar cells that surpass 10%.

Thus, the aim of this thesis is to tune the optoelectronic and structural properties of Sb<sub>2</sub>Se<sub>3</sub>, which have been identified as limiting factors for the power conversion efficiency of solar cells. This will be approached through alloying and doping strategies, building on

existing literature, and developing a novel fabrication approach for  $\text{Sb}_2\text{Se}_3$  thin film to achieve higher crystalline quality for solar cell applications. More precisely, the objectives are the following:

1. To prepare antimony selenosulphide  $\text{Sb}_2(\text{Se}_{1-x}\text{S}_x)_3$  ( $x = 0-1$ ) polycrystalline materials aiming at bridging the properties of  $\text{Sb}_2\text{Se}_3$  and  $\text{Sb}_2\text{S}_3$ , and to study the changes in the defect structure and optical properties of  $\text{Sb}_2\text{Se}_3$  upon the formation of the solid solution by using photoluminescence spectroscopy.
2. To apply Sn-doping on the  $\text{Sb}_2\text{Se}_3$  polycrystalline material aiming at improved  $p$ -type conductivity, and to analyse the changes in the electronic band structure of intrinsic  $\text{Sb}_2\text{Se}_3$  resulting from Sn-doping by using ultraviolet photoelectron spectroscopy.
3. To develop a fabrication approach for  $\text{Sb}_2\text{Se}_3$  thin film absorbers that combines RF-magnetron sputtering and post-thermal selenization in an inert gas at elevated pressures, aimed at enhancing [001] grain orientation in  $\text{Sb}_2\text{Se}_3$  thin films for solar cell applications.

## 2 Experimental

This chapter describes the experimental methods applied for the synthesis of  $\text{Sb}_2(\text{Se}_{1-x}\text{S}_x)_3$  solid solutions and Sn-doped  $\text{Sb}_2\text{Se}_3$  polycrystalline samples (Papers I, II), as well as the magnetron sputtering method used for depositing  $\text{Sb}_2\text{Se}_3$  thin films (Paper III). Additionally, the analysis methods used for the characterization of developed materials and devices are introduced.

### 2.1 Synthesis of $\text{Sb}_2(\text{Se}_{1-x}\text{S}_x)_3$ ( $x = 0-1$ ) polycrystalline materials

Polycrystalline  $\text{Sb}_2(\text{Se}_{1-x}\text{S}_x)_3$  solid solutions with  $x = 0, 0.2, 0.4, 0.6, 0.8$  and  $1$  were synthesized from 5 N purity Sb, Se and S (Alfa Aesar) elemental precursors under the same synthesis conditions (Paper I). The precursors were weighed in the desired amounts and ratios, mixed and ground in an agate mortar before being loaded into quartz ampoules, which were then degassed and sealed under dynamic vacuum. A two-step isothermal annealing process in a chamber furnace was used for the synthesis. All six samples together were heated up from RT to  $200\text{ }^\circ\text{C}$  within 1 h. After maintaining this temperature for one week, the temperature was increased from  $200\text{ }^\circ\text{C}$  to  $500\text{ }^\circ\text{C}$  within 1 h, where the samples were kept for an additional week. After two weeks, the synthesis-growth processes were stopped by removing the ampoules from the furnace and allowing them to cool naturally in air to room temperature.

### 2.2 Sn-doping of $\text{Sb}_2\text{Se}_3$ polycrystalline materials

Polycrystalline  $\text{Sb}_2\text{Se}_3$  was synthesized from 5 N purity Sb and Se elemental precursors from Alfa Aesar at  $500\text{ }^\circ\text{C}$  in degassed and sealed quartz ampoules (Paper II). From the synthesized polycrystalline  $\text{Sb}_2\text{Se}_3$  powder, 200 mg portions of material were extracted for Sn doping, which was achieved by isothermal post-annealing of four portions of  $\text{Sb}_2\text{Se}_3$  material at  $350\text{ }^\circ\text{C}$ ,  $400\text{ }^\circ\text{C}$ ,  $450\text{ }^\circ\text{C}$ ,  $500\text{ }^\circ\text{C}$ , respectively, along with 0.04 g of  $\text{SnSe}_2$  pellets (self-synthesized) for 30 minutes in degassed and sealed quartz ampoules with 0.06 m in length.  $\text{Sb}_2\text{Se}_3$  and  $\text{SnSe}_2$  were placed non-attached at a distance of 0.05 m within the ampoules. The Sn-doping process is schematically illustrated in Figure 7.

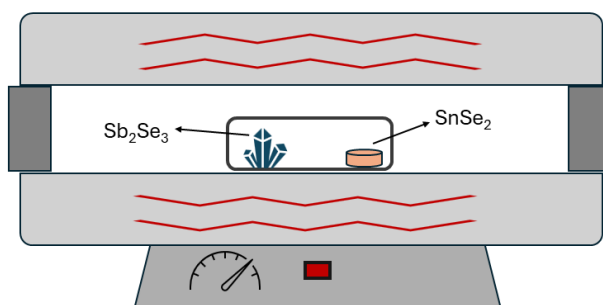


**Figure 7.** Schematic illustration of Sn-doping of  $\text{Sb}_2\text{Se}_3$  by isothermal post-annealing of the polycrystals together with  $\text{SnSe}_2$  pellets in degassed and sealed quartz ampoules in the cylindrical furnace (Paper II).

## 2.3 Fabrication of $\text{Sb}_2\text{Se}_3$ thin films by magnetron sputtering and selenization

Magnetron sputtering is a physical vapour deposition method conducted in an ultra-high vacuum environment, supported by a cryogenic pumping sub-system. The target holder is magnetized by an RF or DC power supply, enabling so that  $\text{Ar}^+$  ions, released into the chamber at a controlled rate measured in standard cubic centimetres per minute (sccm), to collide inelastically with the target surface. This interaction generates cold plasma, which subsequently deposits onto the substrate located at a controlled distance within the chamber. This technology is widely used for depositing metals and semiconductor thin films, offering a controllable deposition rate ( $\text{\AA}/\text{s}$ ). The working principle of the magnetron sputtering system is illustrated in Figure 8.

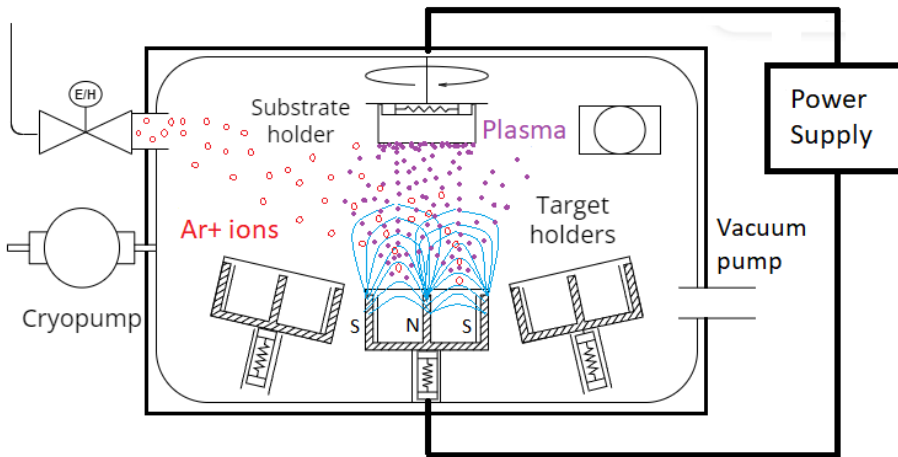


**Figure 8.** Illustration of the working principle of magnetron sputtering.

Molybdenum (Mo) and Sb thin films were deposited using an Angstrom Engineering Evovac 030 magnetron sputtering system equipped with three sputtering sources with glow discharge (Paper III). Mo and Sb targets with 99.99% purity from Testbourne Inc. were used. At first, a  $1.2\ \mu\text{m}$  thick Mo thin film was sputtered onto borosilicate glass (BSG) using a DC power of 200 W, a substrate temperature of  $300\ ^\circ\text{C}$  and an ionized argon ( $\text{Ar}^+$  gas) pressure of  $5 \times 10^{-3}$  Torr in a chamber. After reference deposition of Mo, the sheet resistance of the  $10 \times 10\ \text{cm}^2$  Mo/BSG thin film was measured to be only a few ohms across the entire surface. The Sb sputtering process was conducted continuously under high vacuum without removing the Mo/BSG substrate from the vacuum chamber of the magnetron sputtering system, following a one-day cooling period of the substrate temperature to RT. Sb was sputtered with an RF power of 60 W onto Mo/BSG substrate ( $10 \times 10\ \text{cm}^2$ ) at RT, an  $\text{Ar}^+$  gas flow of 20 sccm, and pressure of  $5 \times 10^{-6}$  Torr. The  $100\ \text{cm}^2$  Sb/Mo/BSG thin film was then removed from the deposition chamber and cut into  $1\ \text{cm}^2$  pieces, which subsequently underwent the selenization process in sealed quartz ampoules at various temperatures. For the selenization process, the Sb/Mo/BSG thin films were placed into 8 cm-long quartz ampoules together with the elemental Se beads

of 5N purity from Alfa Aesar. The quartz ampoules were then degassed and filled with argon gas at different pressures at RT before being sealed. A cylindrical furnace was used for the isothermal selenization process to ensure uniform heat distribution across the thin film samples. The distance between a Se bead and the Sb/Mo/BSG thin film inside the ampoule was maintained at 7 cm, identical for all the samples. The samples in the closed ampoules were placed individually in the furnace preheated to the target temperature. The selenization time was kept constant at 30 minutes, while the selenization temperature and argon gas pressure were varied. After 30 minutes of selenization, the ampoules containing the samples were removed from the furnace and allowed to cool naturally to room temperature. The described technological route is illustrated in Figure 9.

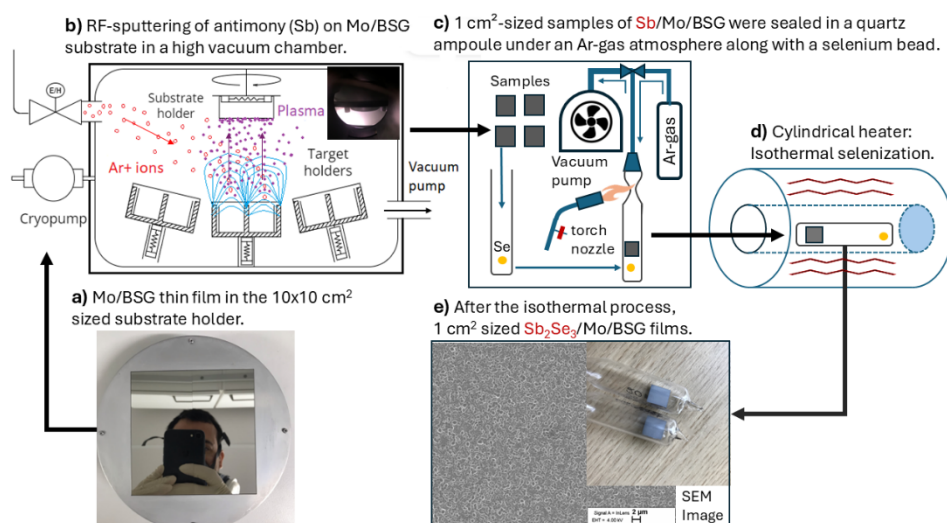


**Figure 9.** Technological route developed for the preparation of Sb<sub>2</sub>Se<sub>3</sub> thin films (Paper III).

## 2.4 CdS buffer layer and ZnO window layer deposition

To test the developed Sb<sub>2</sub>Se<sub>3</sub> thin films in a solar cell device (Paper III), a pulsed laser deposition (PLD) system by Neocera, equipped with a COMPex laser with  $\lambda = 248$  nm was employed to deposit a 50 nm CdS buffer layer on top of the Sb<sub>2</sub>Se<sub>3</sub>/Mo/BSG thin films. The deposition was conducted at a substrate temperature of 200 °C and deposition pressure of  $2 \times 10^{-3}$  Torr, using 3000 pulses at a frequency of 10 Hz, with each pulse delivering 200 mJ of energy. To complete the solar cell devices, 350 nm ZnO:Al was deposited on top of the CdS by RF magnetron sputtering.

## 2.5 Applied characterization methods

### 2.5.1 Scanning electron microscopy (SEM) and energy dispersive x-ray spectroscopy (EDS)

The elemental compositions of the  $\text{Sb}_2(\text{Se}_{1-x}\text{S}_x)_3$  solid solutions,  $\text{Sb}_2\text{Se}_3$  polycrystals and thin films were determined by energy-dispersive X-ray spectroscopy (EDS) using a Bruker Esprit 1.8 system on a Zeiss Merlin high-resolution scanning electron microscope (SEM). EDX analysis on the polycrystalline materials was made from polished cross-section of the crystals.

### 2.5.2 Micro-Raman spectroscopy

The phase composition of  $\text{Sb}_2(\text{Se}_{1-x}\text{S}_x)_3$  solid solutions,  $\text{Sb}_2\text{Se}_3$  polycrystals and thin films were studied by using RT micro-Raman scattering with Horiba's LabRam HR800 spectrometer with a 532 nm laser line (YAG: Nd laser) and a multichannel CCD detection system. The laser spot size on the sample was 10  $\mu\text{m}$  in diameter. The system enables spectral resolution better than  $1\text{ cm}^{-1}$ .

### 2.5.3 X-ray diffraction spectroscopy (XRD)

The Raman analysis was complemented by the powder X-ray diffraction (XRD) analysis using a Rigaku Ultima IV diffractometer operating with the silicon strip detector D/teX Ultra. PDXL 2 software was used for the derivation of crystal structure information from the powder XRD data (ICDD 01-083-7430 and 03-065-2434 for  $\text{Sb}_2\text{Se}_3$  and  $\text{Sb}_2\text{S}_3$ , respectively).

### 2.5.4 Ultraviolet-visible spectroscopy (UV-Vis)

Energy band gaps of the undoped and Sn-doped  $\text{Sb}_2\text{Se}_3$  polycrystalline materials (Paper II) were determined by ultraviolet-visible spectroscopy (UV-Vis) using a Shimadzu UV-1800 spectrophotometer equipped with a specular reflector.

### 2.5.5 X-ray photoelectron spectroscopy (XPS)

X-ray photoelectron spectroscopy (XPS) was used to determine the Sn-doping of the  $\text{Sb}_2\text{Se}_3$  polycrystals (Paper II). The Kratos Analytical AXIS ULTRA DLD spectrometer fitted with the monochromatic Al  $K\alpha$  X-rays source and the achromatic Mg  $K\alpha$ /Al  $K\alpha$  dual anode X-ray source was used for the XPS measurements. The depth profiling of elemental composition was obtained by  $\text{Ar}^+$  ion sputtering using  $\text{Ta}_2\text{O}_3$  reference sample with known thickness for evaluation of the sputtering depth.

### 2.5.6 Ultraviolet photoelectron spectroscopy (UPS)

UPS analysis was applied for determining the work function of the  $\text{Sb}_2\text{Se}_3$  polycrystals (Paper II) using an Axis Ultra DLD photoelectron spectrometer (Kratos Analytical) fitted with a helium discharge lamp. The He discharged lamp with resonance line He(I) ( $h\nu = 21.22\text{ eV}$ ) was used to obtain UPS spectra. Before the measurement, the Ag foil and the  $\text{Sb}_2\text{Se}_3$  and  $\text{Sb}_2\text{Se}_3:\text{Sn}$  polycrystalline sample surfaces were cleaned by argon ion sputtering (4 keV, 10 mA) for 2 min. A bias of  $-9.124\text{ V}$  was used to separate the analyser and the secondary edges of the sample, and the bias was optimized to shift the Ag spectrum into the linear region of the analyser (kinetic energy of 0–10 eV). A spectrometer

with a pass energy of 5 eV and a large area aperture of  $300\ \mu\text{m} \times 700\ \mu\text{m}$  was used. Under these conditions, the energy resolution of the spectra was measured at the Fermi edge of the clean Ag foil at RT.

### **2.5.7 Photoluminescence spectroscopy (PL)**

Photoluminescence spectroscopy was used for studying the optical and defect properties of the  $\text{Sb}_2(\text{Se}_{1-x}\text{S}_x)_3$  polycrystals (Paper I). For the PL measurements the  $\text{Sb}_2(\text{Se}_{1-x}\text{S}_x)_3$  polycrystals were mounted on the cold finger of a closed-cycle helium cryostat Janis SHI-4 of Lake Shore Cryotronics and the measurements were carried out in the temperature region of 3–110 K. Near band edge PL spectra were excited with a diode-pumped Nd:YAG solid state laser with the wavelength of 266 nm, pulse width 0.6 ns, and repetition rate 19 kHz. The maximum peak energy was 0.75  $\mu\text{J}$  and the maximum average power was approximately 15 mW. The maximum peak power density was estimated to be  $660\ \text{kW cm}^{-2}$ . The laser beam was not focused to avoid damaging the sample and the pump power was reduced by a gradient UV (fused silica) filter. The PL signal was dispersed using a 0.5 m focal length Andor SR-500i monochromator and captured with thermoelectrically cooled InGaAs detector IGA-030-TE2-H of Electro-Optical Systems Inc and with Hamamatsu R632 photomultiplier tube in the case of  $\text{Sb}_2\text{S}_3$ . For comparison, the PL spectra of deeper bands in the  $\text{Sb}_2(\text{Se}_{1-x}\text{S}_x)_3$  polycrystals were also measured by using a continuous wave He–Cd gas laser (Kimmon) with a wavelength of 442 nm and maximum power of 37.1 mW. For the respective measurements, the samples were mounted on the cold finger of a closed-cycle helium cryostat (Janis CCS-150) and cooled down to 20 K. For PL signal detection, a Hamamatsu InGaAs photomultiplier tube was used in the range of 0.77–1.35 eV. Neutral density filters were used to alter the laser power density on the sample.

### **2.5.8 I-V characteristics and external quantum efficiency (EQE)**

To measure the *I-V* characteristics and determine the PCE of  $\text{ZnO:Al/CdS/Sb}_2\text{Se}_3/\text{Mo/BSG}$  solar cells, a Keithley 2400 source meter was employed under standard test conditions (AM1.5,  $100\ \text{mW/cm}^2$ ) using a Newport Oriel Class A 91195A solar simulator. The measurements of the external quantum efficiency (EQE) spectra were performed on a commercial EQE measurement system from Scientech Inc (Paper III).

### 3 Results and discussion

In this chapter, the first section 3.1 presents the results of the study of optical properties of  $\text{Sb}_2(\text{Se}_{1-x}\text{S}_x)_3$  ( $x = 0-1$ ) polycrystalline materials studied by PL spectroscopy. The second section 3.2 is dedicated to the results of the study of Sn-doping of  $\text{Sb}_2\text{Se}_3$  polycrystals, focusing on the changes in the electronic structure due to Sn-doping, which is investigated by UPS. The third section (3.3) presents the results of the development of a controllable method for depositing  $\text{Sb}_2\text{Se}_3$  thin films with highly oriented grains and a compact morphology.

#### 3.1 Optical properties of $\text{Sb}_2(\text{Se}_{1-x}\text{S}_x)_3$ ( $x = 0-1$ ) polycrystalline materials

##### 3.1.1 Elemental and phase composition of $\text{Sb}_2(\text{Se}_{1-x}\text{S}_x)_3$ polycrystals

A summary of the EDS microanalysis, measured at multiple spots from each polycrystalline solid solution and presented in Table 3, confirm the targeted elemental compositions of  $\text{Sb}_2(\text{Se}_{1-x}\text{S}_x)_3$  (with  $x$  varying from 0 to 1, and  $\Delta x \sim 0.2$ ).

**Table 3.** Elemental compositions of the studied  $\text{Sb}_2(\text{Se}_{1-x}\text{S}_x)_3$  solutions determined by EDX.

Solid solutions $\text{Sb}_2(\text{Se}_{1-x}\text{S}_x)_3$	$x = \text{S}/(\text{S}+\text{Se})$ input	$x = \text{S}/(\text{S}+\text{Se})$ output	Antimony (Sb), at%	Selenium (Se), at%	Sulfur (S), at%
$\text{Sb}_2\text{Se}_3$	$x = 0$	$x = 0$	$40.1 \pm 1.4$	$59.8 \pm 1.4$	-
$\text{Sb}_2(\text{Se}_{0.8}\text{S}_{0.2})_3$	$x = 0.2$	$x = 0.21$	$40.2 \pm 1.5$	$46.8 \pm 1.2$	$12.9 \pm 0.2$
$\text{Sb}_2(\text{Se}_{0.6}\text{S}_{0.4})_3$	$x = 0.4$	$x = 0.38$	$39.9 \pm 1.6$	$36.8 \pm 1.0$	$23.2 \pm 0.3$
$\text{Sb}_2(\text{Se}_{0.4}\text{S}_{0.6})_3$	$x = 0.6$	$x = 0.60$	$40.1 \pm 1.7$	$23.8 \pm 0.7$	$35.9 \pm 0.5$
$\text{Sb}_2(\text{Se}_{0.2}\text{S}_{0.8})_3$	$x = 0.8$	$x = 0.81$	$40.1 \pm 1.8$	$10.8 \pm 0.3$	$49.0 \pm 0.7$
$\text{Sb}_2\text{S}_3$	$x = 1$	$x = 1$	$40.2 \pm 1.9$	-	$59.8 \pm 0.9$

The evolution of the Raman spectra and XRD patterns with varying  $x$ -value in  $\text{Sb}_2(\text{Se}_{1-x}\text{S}_x)_3$  is presented in Figure 10 and Figure 11, respectively. The experimental Raman spectra were fitted with the Lorentzian functions. The Raman spectra of the end members,  $\text{Sb}_2\text{Se}_3$  and  $\text{Sb}_2\text{S}_3$ , are in very good correlation to the literature data with dominating  $A_g^2$  mode at  $190 \text{ cm}^{-1}$  accompanied with other modes at 100, 125, 156,  $213 \text{ cm}^{-1}$  in  $\text{Sb}_2\text{Se}_3$  [93], and at  $A_g^2$  mode of  $\text{Sb}_2\text{S}_3$  at  $283 \text{ cm}^{-1}$  accompanied with the other modes at 98, 125, 156, 190, 239,  $310 \text{ cm}^{-1}$  [94][95]. The bimodal behaviour of  $A_g^2$ -modes confirms the formation of the  $\text{Sb}_2(\text{Se}_{1-x}\text{S}_x)_3$  solid solutions, as shown in Figure 10a and Figure 10b. However, two distinct Raman studies of  $\text{Sb}_2\text{S}_3$ , report variations in the  $A_g$  mode at  $312 \text{ cm}^{-1}$  [94] and  $B_{2g}$  mode at  $314 \text{ cm}^{-1}$  [95] under different polarization, pressure and temperature conditions.

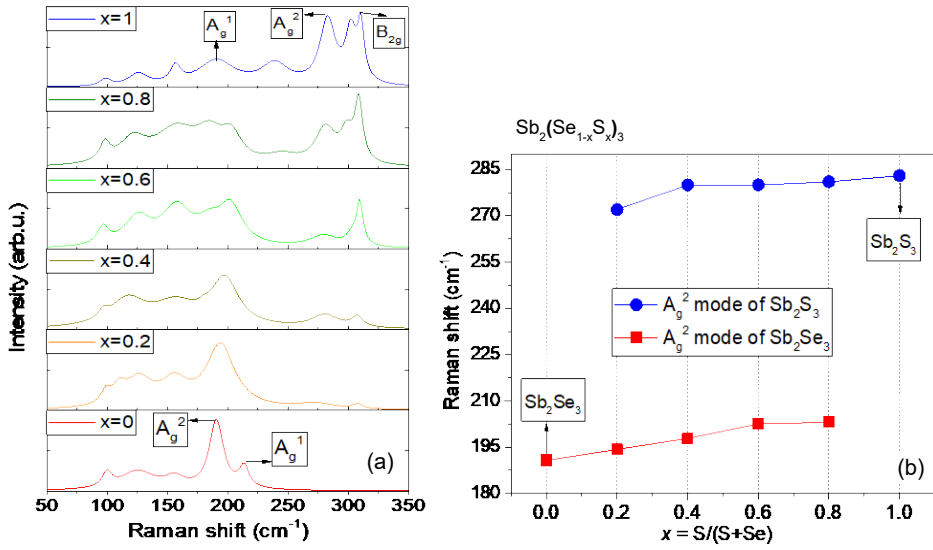


**Figure 10.** a) Raman spectra of  $Sb_2(Se_{1-x}S_x)_3$  solid solutions, b) bimodal behaviour of the  $A_g^2$  Raman modes regarding the  $x$ -value.

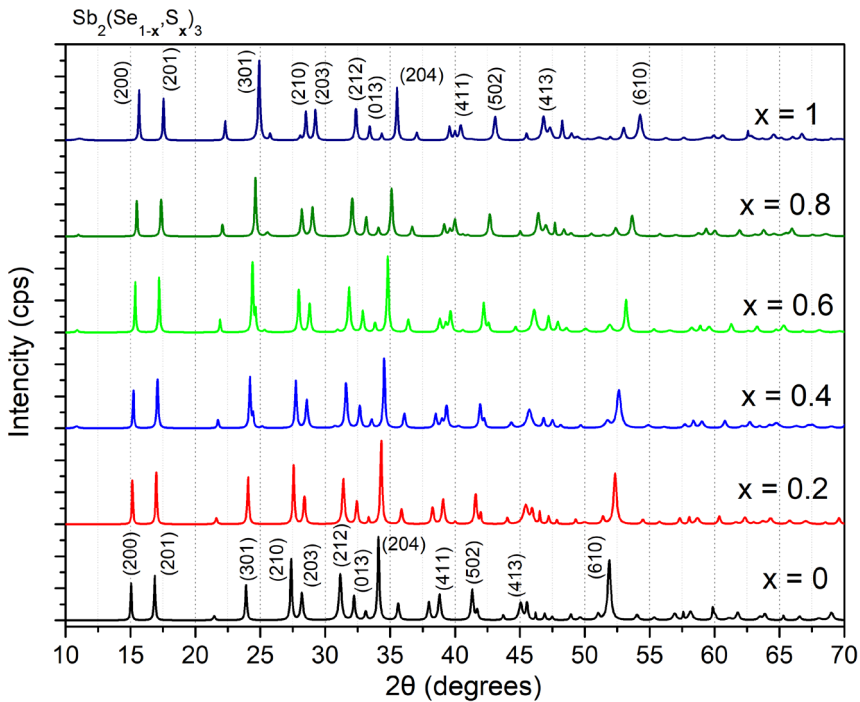


**Figure 11.** XRD patterns of  $Sb_2(Se_{1-x}S_x)_3$  solid solutions, as the  $x$  changes from 0 to 1.

The XRD patterns of the solid solutions shown in Figure 11 with varying  $x$  value from 0 to 1, indicate that all the peaks correspond to  $Sb_2Se_3$ ,  $Sb_2S_3$  and to their solid solutions, in accordance with ICDD 01-083-7430 for  $Sb_2Se_3$  and ICDD 03-065-2434 for  $Sb_2S_3$ . All the solid solutions were determined to have an orthorhombic structure with space group

Pnma. A shift of the XRD peaks towards higher degrees was observed with increasing x-value in the  $\text{Sb}_2(\text{Se}_{1-x}\text{S}_x)_3$  solid solutions. The lattice parameters for each solid solution were extracted using Rietveld refinement procedure and the corresponding values related to the x-value are shown in Figure 12.

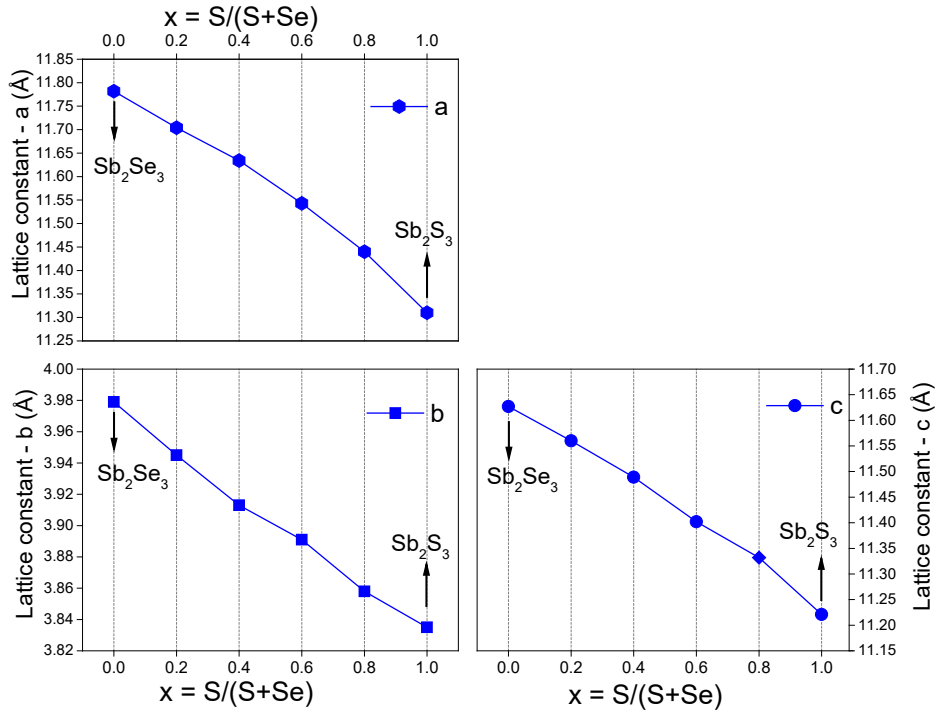


**Figure 12.** The change in lattice constants for  $\text{Sb}_2(\text{Se}_{1-x}\text{S}_x)_3$  solid solutions depending on the x-value.

### 3.1.2 Optical properties of $\text{Sb}_2(\text{Se}_{1-x}\text{S}_x)_3$ polycrystals

To study the electronic and defect structure of the  $\text{Sb}_2(\text{Se}_{1-x}\text{S}_x)_3$  solid solutions, temperature and laser power dependent photoluminescence measurements were performed and analysed. Figure 13 presents the PL bands excited with the continuous wave laser at  $T = 20$  K. The dominating PL band position,  $E_{max}$ , exhibits a blueshift from 0.856 eV to 1.107 eV as the value of x increases from 0 to 1. This shift is attributed to the changes in the energy bandgap of the  $\text{Sb}_2(\text{Se}_{1-x}\text{S}_x)_3$  solid solutions. The dominating PL band of  $\text{Sb}_2\text{Se}_3$  is out of the measurement range ( $< 0.8$  eV). These very broad (FWHM  $\sim 0.25$  eV) and Gaussian shaped deep PL bands have rather low intensity, making the reliable detailed analysis of temperature and laser power dependences impossible. The low temperature ( $T = 3$  K) near band edge PL spectra, measured using a pulsed UV laser and presented in Figure 13, reveal an asymmetric shape of the PL bands. Additionally, there is noticeable shift in the PL emission towards higher energies, increasing from 1.309 eV to 1.728 eV as sulphur content increases. All the detected PL spectra were dominated by an asymmetric PL band, which was fitted using a Split-Pseudo Voigt function. From this point, the analysis will focus on the edge PL emission of  $\text{Sb}_2(\text{Se}_{1-x}\text{S}_x)_3$  excited with the pulsed UV laser (Figure 13).

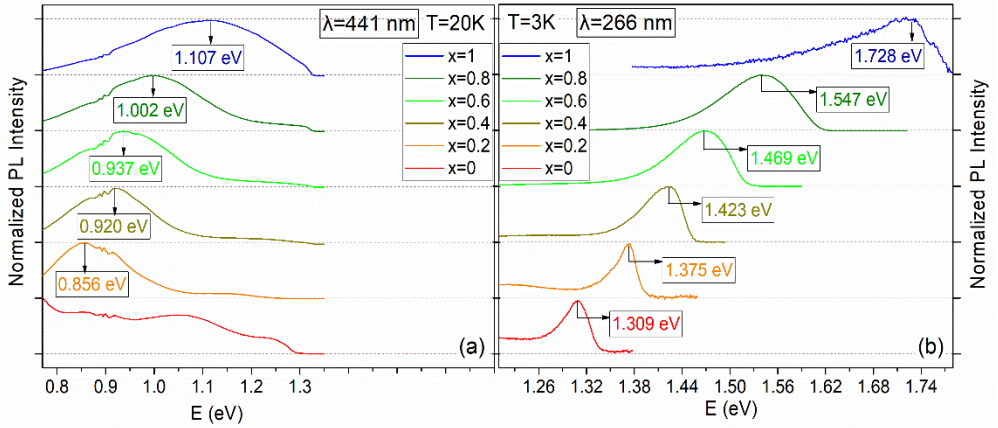


**Figure 13.** a) PL spectra of the  $Sb_2(Se_{1-x}S_x)_3$  solid solutions with  $x = 0$  to 1, respectively, excited by continuous wave laser (441 nm) at 20 K, b) PL spectra of the solid solutions with  $x = 0$  to 1, respectively, excited by the pulsed UV laser (266 nm) at 3 K and 7 mW.

Temperature dependencies of the edge PL band positions  $E_{max}$  of the  $Sb_2(Se_{1-x}S_x)_3$  solid solutions are shown in Figure 14. A redshift of the PL band position with increasing temperature, which is more rapid than the temperature dependence of the bandgap energy [96], was detected for  $Sb_2(Se_{1-x}S_x)_3$  with  $x = 0$  and  $x = 0.2$ . A similar rapid redshift was detected in Ref. [97] and attributed mostly to biexcitons. However, for the other samples, the redshift could not be observed within the used temperature range, as the PL emission quenched fast and disappeared from  $T > 60$  K.

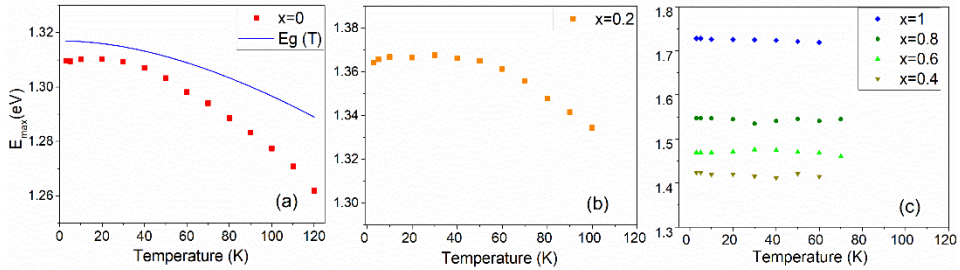


**Figure 14.** Temperature dependencies of near band edge PL emissions from 3 K to 120 K for  $Sb_2(Se_{1-x}S_x)_3$  solid solutions.  $E_g(T)$  is temperature dependence of the bandgap energy for  $Sb_2Se_3$  measured by photoreflectance [96]. a) Redshift of  $E_{max}$  for  $x = 0$ , b) redshift of  $E_{max}$  for  $x = 0.2$ , c) from  $x = 0.4$  to 1, peak positions stay almost constant with increasing temperature.

The temperature dependencies of the integrated intensities ( $\Phi$ ) of the PL emissions of the  $Sb_2(Se_{1-x}S_x)_3$  solid solutions with  $x \leq 0.2$  enabled to determine the thermal activation energies for the corresponding PL bands by fitting the experimental data with the theoretical expression [98]:

$$\Phi(T) = \frac{\Phi_0}{1 + \alpha_1 \cdot T^{3/2} + \alpha_2 \cdot T^{3/2} \cdot \exp\left(-\frac{E_a}{kT}\right)}, \quad (1)$$

where  $\alpha_1$  and  $\alpha_2$  are the process rate parameters,  $T$  is temperature in Kelvin(K),  $k$  is Boltzmann constant, and  $E_a$  is the thermal activation energy. From equation (1), the thermal activation energies were calculated to be  $E_a = 15 \pm 3$  meV and  $E_a = 11 \pm 3$  meV for the samples with  $x = 0$  and  $x = 0.2$ , respectively, as shown in Figure 15. These  $E_a$  values align well with the thermal quenching activation energies reported in a recent study for the excitons and biexcitons [97], suggesting that the PL emission in the  $\text{Sb}_2(\text{Se}_{1-x}\text{S}_x)_3$  solid solutions with  $x \leq 0.2$  is likely of excitonic origin. Unfortunately, the lack of sufficient experimental data points prevented a detailed determination of the PL quenching behaviour for the solid solutions from  $x = 0.4$  to 1.

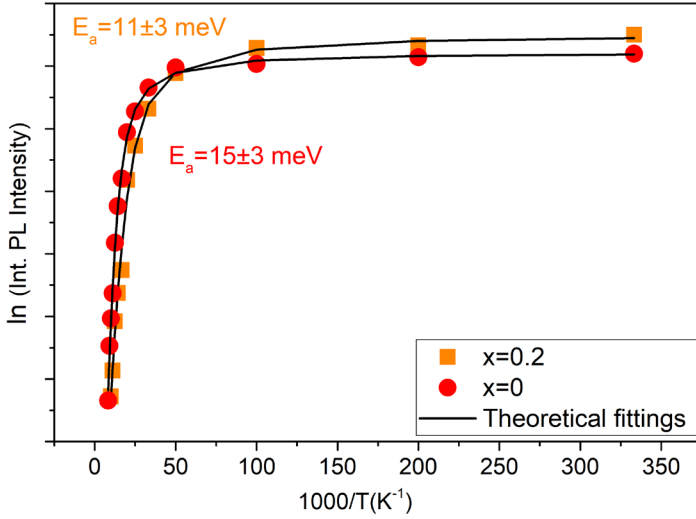


**Figure 15.** Integrated PL intensity of  $\text{Sb}_2(\text{Se}_{1-x}\text{S}_x)_3$  on a log scale as a function of reverse temperature together with the theoretical fitting with equation (1) for  $x = 0$  and for  $x = 0.2$ .

The laser power dependencies of the low-temperature PL emissions have also been investigated to understand better the origin of the PL emission. The dependence of the integrated PL intensity  $\Phi(P)$  as a function of laser power  $P$  in the range from 0.1 mW to 15 mW for the  $\text{Sb}_2(\text{Se}_{1-x}\text{S}_x)_3$  solid solutions with  $x$  varying from 0 to 1 is shown in Figure 16 and is following the dependence  $\Phi \sim P^m$  [99]. The power coefficient values  $m = 1.37$  and  $m = 1.03$  were found for  $\text{Sb}_2(\text{Se}_{1-x}\text{S}_x)_3$  with  $x = 0$  and  $x = 0.2$ , respectively, indicating to the exciton related recombination processes, which are known to have  $m \geq 1$ . Excitons and biexcitons have been recently detected in high quality  $\text{Sb}_2\text{Se}_3$  microcrystals under high PL excitation density [97]. However,  $m < 1$  was found for the remaining  $\text{Sb}_2(\text{Se}_{1-x}\text{S}_x)_3$  solid solutions with  $x = 0.4$  to  $x = 1$ , suggesting a different type of radiative recombination involving charge carriers localized at defects within the band gap. Notably, no shift in the PL band position  $E_{max}$  with increasing laser power was detected for any of the studied  $\text{Sb}_2(\text{Se}_{1-x}\text{S}_x)_3$  solid solutions.

The asymmetric shape of the PL bands at low temperatures can be attributed to electron–phonon coupling, where phonon replicas follow a Poisson distribution, as described by the well-known Frank-Condon configuration coordinate model [100]. Electron–phonon coupling is stronger in samples with  $x > 0.2$ , while the laser power dependence of the PL emission confirms an excitonic origin for samples with  $x \leq 0.2$ . Additionally, deep-donor–deep-acceptor (DD-DA) pair recombination involving a donor

and an acceptor, which are located at very short distance in the crystal lattice includes strong Coulomb interaction between the corresponding defects and can result in close to band edge emission with PL peak energy [101]:

$$E_{DAP} = E_g - (E_A + E_D) + \frac{e^2}{4\pi \cdot \epsilon \epsilon_0 \cdot r}, \quad (2)$$

where  $E_g$  is the bandgap energy,  $E_D$  and  $E_A$  are donor and acceptor ionization energies, respectively,  $\epsilon_0$  is vacuum permittivity,  $\epsilon$  is the relative dielectric constant, and  $r$  is the distance between donor and acceptor defect in the crystal lattice. When paired, the ionization energies of the related donor and acceptor defects in the case of closest pairs are rather small. Usually, DAP emission is characterized with a small blueshift with increasing laser power (in the order of few meV). However, in the case of very close DAPs, there can be almost no blueshift as is observed also in this study for the  $Sb_2(Se_{1-x}S_x)_3$  solid solutions [102].

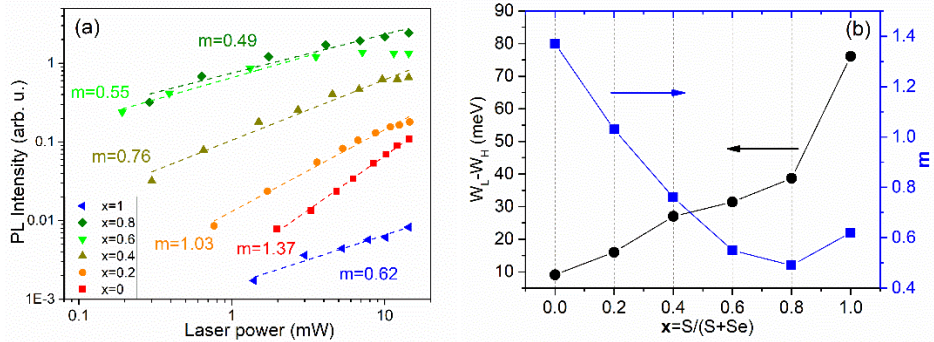


**Figure 16.** a) The integrated intensities of near band edge PL bands as a function of laser power at  $T = 3$  K on a log-log scale for the  $Sb_2(Se_{1-x}S_x)_3$  solid solutions. b) The opposite trends of  $(W_L - W_H)$  and  $m$  value on the  $x$ -value of  $Sb_2(Se_{1-x}S_x)_3$  at  $T = 3$  K.

According to the Frank-Condon configuration coordinate model, the full PL spectrum related to recombination centre consists of zero phonon line and its phonon replicas, which are separated by the phonon energy  $E_{ph}$ . The intensity of each phonon replica is proportional to  $I(k) \sim (\exp(-S) \cdot S^k) / k!$  [100] with  $k$  from 0 to  $\infty$  (see Figure 17). In Poisson distribution,  $S$  parameter is called Huang-Rhys factor and  $E_{ph}$  is usually the longitudinal optical (LO) phonon energy. However, in polycrystalline and anisotropic  $Sb_2(Se_{1-x}S_x)_3$  solid solutions the spectral shape of these components can be different. Inhomogeneous broadening of zero phonon line can increase the halfwidth of all peaks and the shape can become asymmetric. The strength of the electron-phonon interaction and therefore the distribution of the phonon replicas is described by the  $S$  parameter. In this study, namely  $S \sim 0.8$  were determined for the  $Sb_2(Se_{1-x}S_x)_3$  solid solutions. The difference  $(W_L - W_H)$  between half-width of the low energy side ( $W_L$ ) and half-width of the high energy side ( $W_H$ ) of the PL band was found to grow linearly with increasing sulphur content (see Figure 16).

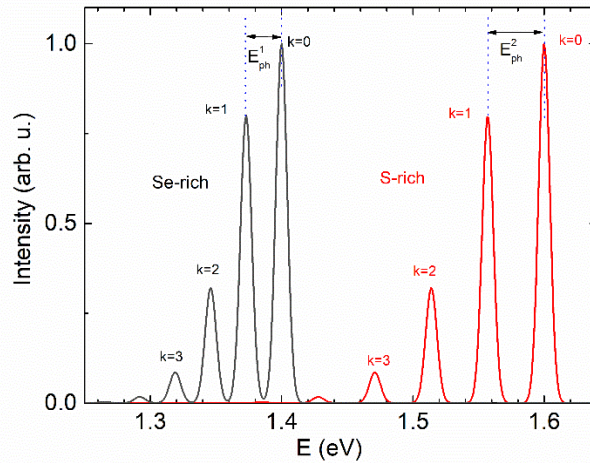


**Figure 17.** Theoretical shape of PL bands with different phonon energies and  $S = 0.8$ . Gaussian shape with  $w = 10$  meV was used in calculations. The zero-phonon line position was taken 1.4 and 1.6 eV for Se-rich and S-rich  $\text{Sb}_2(\text{Se}_{1-x}\text{S}_x)_3$  cases, respectively. The asymmetry of resulting PL band is increasing with increase of  $E_{ph}$ .

The increased asymmetry of the PL band with increasing  $x$  value is more or less related to the increase of phonon energy  $E_{ph}$ , see Figure 10a and Figure 17. The position of the PL band follows a linear trend towards higher energies with increasing  $x$  value in  $\text{Sb}_2(\text{Se}_{1-x}\text{S}_x)_3$ , with the exception of  $x = 1$  ( $\text{Sb}_2\text{S}_3$ ), which shows a PL band at higher energies than the linear trend predicts. Considering also the low PL intensity of the  $\text{Sb}_2\text{S}_3$  sample, it can be proposed that this sample has lower crystalline quality and may contain amorphous  $\text{Sb}_2\text{S}_3$  phase, which has higher band gap ( $> 1.8$  eV [103]) compared to crystalline  $\text{Sb}_2\text{S}_3$ . The amorphous phase could result from non-optimized growth conditions for  $\text{Sb}_2\text{S}_3$ , as the same growth conditions were applied across the entire series of  $\text{Sb}_2(\text{Se}_{1-x}\text{S}_x)_3$  solid solutions.

## 3.2 Electronic band structure of Sn-doped $\text{Sb}_2\text{Se}_3$ polycrystals

Although research on Sn-doping of  $\text{Sb}_2\text{Se}_3$  is available in the literature, the corresponding ultraviolet photoelectron spectroscopy (UPS) spectra have not been reported. In this study, the effect of Sn-doping on the  $\text{Sb}_2\text{Se}_3$  polycrystalline material was investigated to alter its optical properties and electronic band structure aiming at improved  $p$ -type conductivity.

### 3.2.1 Compositional properties of Sn-doped $\text{Sb}_2\text{Se}_3$ polycrystals

$\text{Sb}_2\text{Se}_3$  polycrystals were isothermally annealed at 350 °C, 400 °C, 450 °C, and 500 °C, in the presence of tin diselenide ( $\text{SnSe}_2$ ) within degassed quartz ampoules to facilitate the introduction of Sn into the material. The samples with  $\text{SnSe}_2$  were labelled as  $\text{SbSe}_{350}$ ,  $\text{SbSe}_{400}$ ,  $\text{SbSe}_{450}$ , and  $\text{SbSe}_{500}$  based on their respective annealing temperatures. The un-annealed and un-doped reference sample was labelled as  $\text{SbSe}_0$ . As shown in Figure 18, the XRD analysis did not reveal any secondary phases or the formation of  $(\text{Sb}_x\text{Sn}_{1-x})_2\text{Se}_3$  alloys, as verified by Rietveld analysis using the ICDD 01-083-7430 data card. The RT micro-Raman spectra presented in Figure 19, along with EDS analysis results in Table 4, also confirmed the uniform single-phase composition of the  $\text{Sb}_2\text{Se}_3$  polycrystals.

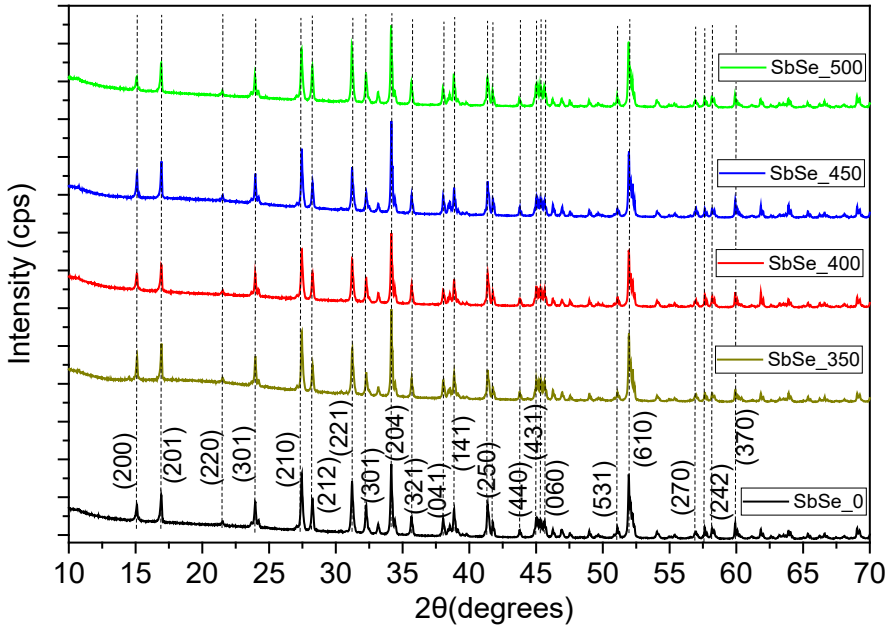


**Figure 18.** XRD patterns of the Sn-doped and reference  $Sb_2Se_3$  polycrystals showing single-phase material composition matching the reference  $Sb_2Se_3$  on ICDD 01-083-7430.

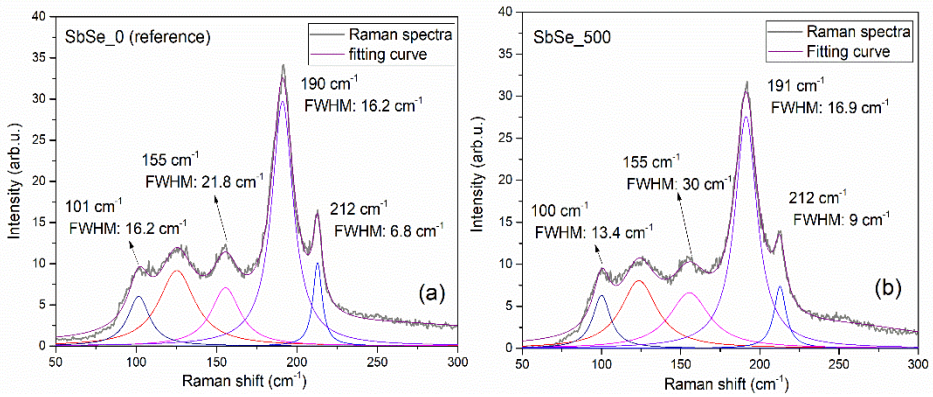


**Figure 19.** a) Raman spectra of the intrinsic  $Sb_2Se_3$  ( $SbSe_0$ ), and b) Sn-doped  $Sb_2Se_3$  ( $SbSe_500$ ).

**Table 4.** Elemental compositions of the studied  $Sb_2Se_3$  and Sn-doped  $Sb_2Se_3$  polycrystalline samples determined by EDS.

Element, at.%	SbSe_0	SbSe_350	SbSe_400	SbSe_450	SbSe_500
Antimony	41.31 ± 1.5	40.41 ± 1.4	40.11 ± 1.6	40.35 ± 1.4	40.97 ± 1.5
Selenium	58.69 ± 1.4	59.59 ± 1.4	59.89 ± 1.6	59.65 ± 1.4	59.03 ± 1.4

The EDS analysis revealed a slightly Sb-rich composition of the  $\text{Sb}_2\text{Se}_3$  samples, with an error margin of approximately 1.5 atomic %. Therefore, it is expected that both EDS and also XRD analysis would not detect any Sn content in the samples, as doping concentration of tin is likely to be sufficiently low. As a result, unwanted secondary phases did not form in  $\text{Sb}_2\text{Se}_3$  due to the post-thermal process with  $\text{SnSe}_2$ .

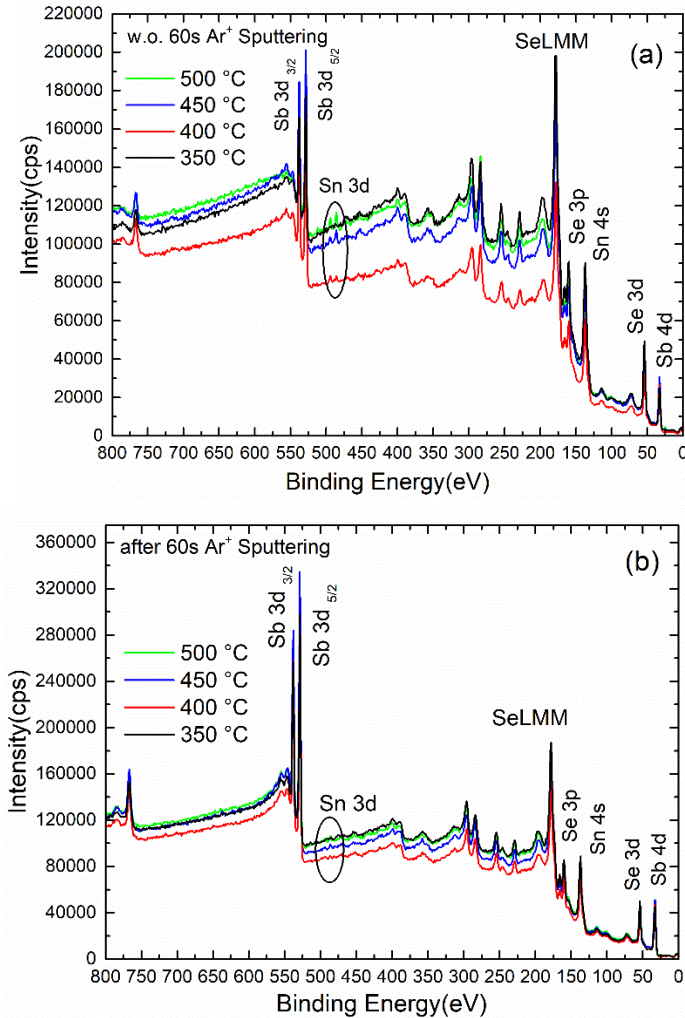


**Figure 20.** a) XPS survey spectra of  $\text{Sb}_2\text{Se}_3$  polycrystalline samples, to which Sn-doping process was applied at four different temperatures: 350 °C, 400 °C, 450 °C, and 500 °C, and b) XPS survey spectra of the same samples after Argon-ion sputtering for 60 seconds.

On the other hand, the highly sensitive XPS analysis enabled to detect the presence of Sn on the surface of the thermally processed  $\text{Sb}_2\text{Se}_3$  polycrystals. The XPS survey spectra of  $\text{Sb}_2\text{Se}_3$  polycrystalline samples before and after  $\text{Ar}^+$  sputtering are shown in Figure 20. The Sn  $3d_{5/2}$  peak at 486 eV and Sn  $3d_{3/2}$  peak at 495 eV were detected by the XPS, as shown in Figure 21. This observation aligns well with the data reported by Nanda et al. [104], confirming the successful incorporation of Sn into the surface of  $\text{Sb}_2\text{Se}_3$ .

However, after 60 seconds of Ar<sup>+</sup> sputtering (equivalent to a material thickness of approximately 5 nm), only the SbSe\_500 sample showed significant intensity of the Sn 3d<sub>5/2</sub> and Sn 3d<sub>3/2</sub> peaks (see Figure 21), leading to its selection for further analysis. The XPS peaks of Sb<sub>2</sub>Se<sub>3</sub> are in correspondence with the ones presented by Don et al. [105].

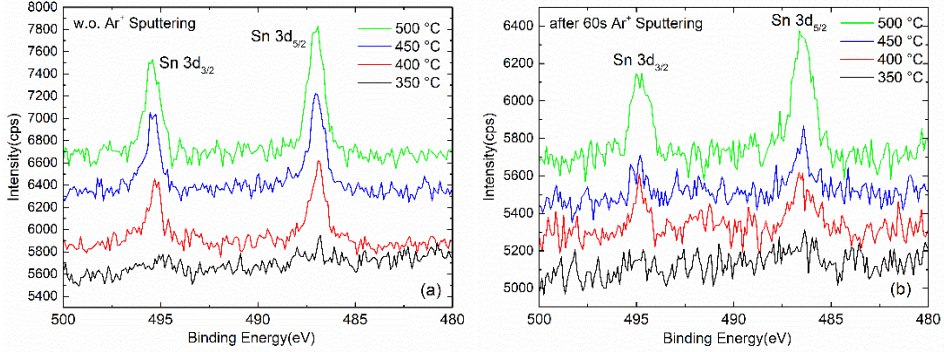


**Figure 21.** Sn - 3d doublets determined by XPS a) from the surface of the Sn-doped Sb<sub>2</sub>Se<sub>3</sub> polycrystals and b) after 60 seconds of Argon-ion sputtering corresponding to the removal of 0.5 nm of the surface layer.

### 3.2.2 Electronic band structure of Sn-doped Sb<sub>2</sub>Se<sub>3</sub> by UPS

To investigate the influence of Sn-doping on the electronic band structure of Sb<sub>2</sub>Se<sub>3</sub> polycrystals, an UPS study was conducted on both the SbSe\_0 and SbSe\_500 samples. For the UPS measurements, the pressure of the He lamp was optimized to ensure maximum signal intensity and stability during the experiment. The UV excitation intensity and the angle of the sample plane with the UV source were kept identical for both SbSe\_0 and SbSe\_500. Figure 22 a and Figure 22 b present a comparison of the combined He(I)-UPS spectra for the SbSe\_0 and SbSe\_500 samples at the binding energy and kinetic energy scales, allowing for an examination of the relative differences in their work functions, as  $\Phi_{\text{SbSe}_0} = E_{\text{vacuum}} - E_{f, \text{SbSe}_0}$  and  $\Phi_{\text{SbSe}_{500}} = E_{\text{vacuum}} - E_{f, \text{SbSe}_{500}}$ , respectively.

Further to that, the work functions of SbSe\_0 and SbSe\_500 were calculated by using equation (3), as pointed out respectively in Figure 23 a, and Figure 23 b.

$$\Phi = h\nu - E_{\text{cutoff}}, \quad (3)$$

where  $\Phi$  is the work function,  $h\nu$  is the excitation energy of He(I) line = 21.22 eV, and  $E_{\text{cutoff}}$  is the secondary electron cutoff energy extracted with a linear fitting at the high binding energy spectra in Figure 22. From equation (4), the work function of SbSe\_0 is  $\Phi = 21.22 \text{ eV} - 16.83 \text{ eV} = 4.39 \text{ eV}$  on the surface and  $\Phi = 21.22 \text{ eV} - 16.88 \text{ eV} = 4.34 \text{ eV}$  beneath the surface after Ar-sputtering, while lower values were obtained for SbSe\_500, namely  $\Phi = 21.22 \text{ eV} - 17.92 \text{ eV} = 3.3 \text{ eV}$  on the surface and  $\Phi = 21.22 \text{ eV} - 18.08 \text{ eV} = 3.14 \text{ eV}$  after the Ar-sputtering.

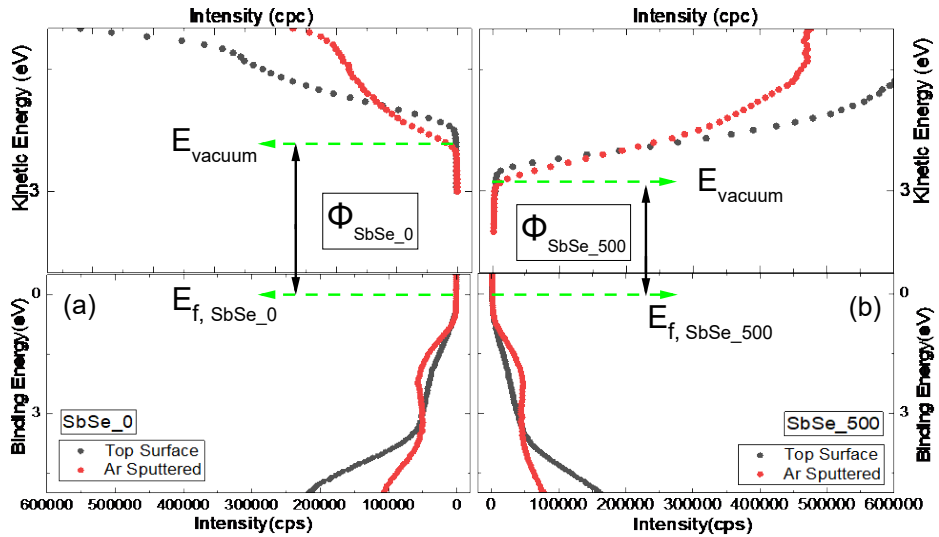


**Figure 22.** Work function ( $\Phi$ ) shown by using the combined UPS spectra referring to the Fermi level (0 eV) for a) the SbSe\_0 (reference) sample, and b) the SbSe\_500 sample.

The Sn-doping process also altered the valence band onset ( $V_{B_{onset}}$ ) in polycrystalline  $Sb_2Se_3$ . With the binding energy spectrum plotted relative to the Fermi level (0 eV) in Figure 23 a and Figure 23 b for the SbSe\_0 and SbSe\_500 samples, the  $V_{B_{onset}}$  values were also determined by drawing tangent lines at the cutoff and the baselines of the spectra [106]. In the tangent lines obtained by linear fittings of the binding energy spectra, the slope values for the SbSe\_500 sample show a decrease compared to those of SbSe\_0 sample. Therefore, the energetic distance between the VBM and the Fermi level on the surface is determined as  $E_f - E_{VB} = 0.46$  eV and 0.40 eV for SbSe\_0 and SbSe\_500, respectively. After cleaning the sample surfaces by Ar-sputtering, beneath the surface, the energy difference between the Fermi level and the valence band edge ( $E_f - E_{VB}$ ) was found to be 0.61 eV SbSe\_0 sample and 0.58 eV for the SbSe\_500 sample. For the SbSe\_500 sample, the Fermi level is positioned closer to the valence band, both on the material's surface and beneath the surface. The difference between the Fermi levels is relatively small, however, it suggests that increasing the Sn content could further enhanced p-type conductivity. To achieve this, the Sn-doping process could be further optimised or alternative Sn doping procedures could be developed to enable higher levels of Sn incorporation.

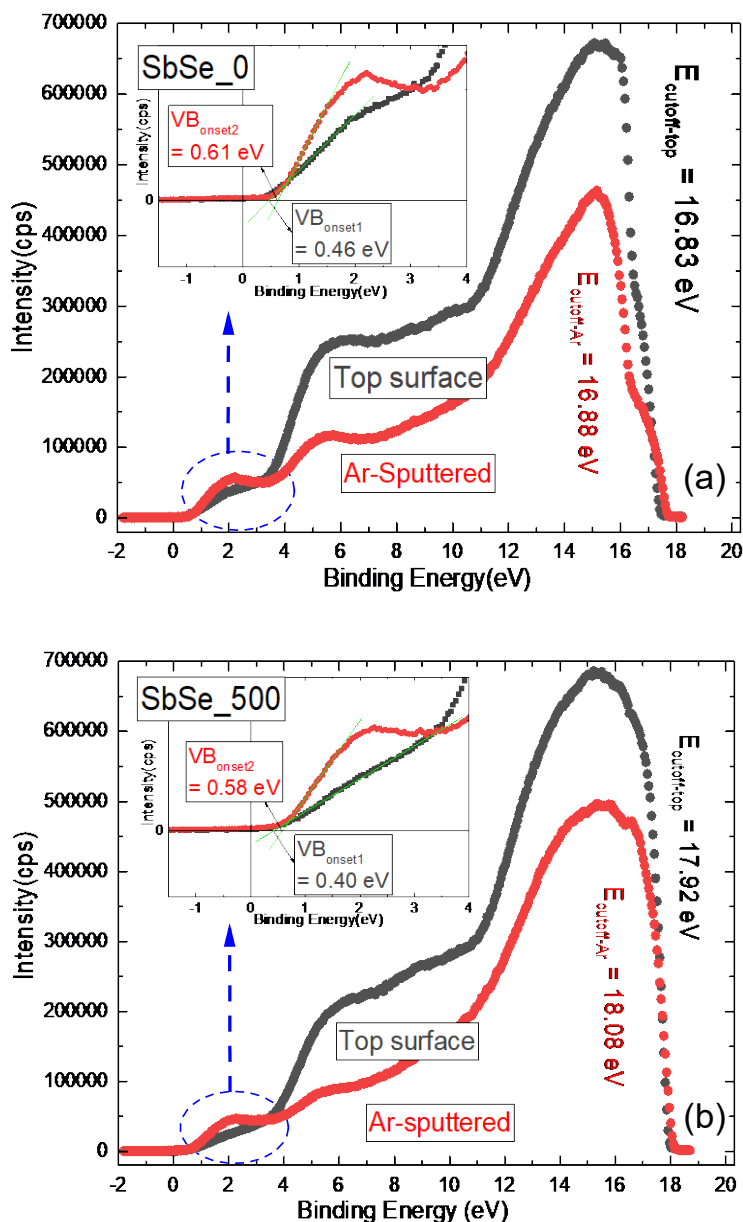


**Figure 23.**  $E_{cutoff}$  values linearly fitted on the UPS spectra in binding energy scale before and after Ar-ion sputtering, and the onset of the valence band ( $VB_{onset}$ ) at low binding energy a) for the SbSe\_0 reference sample and b) for the SbSe\_500, Sn-doped sample.

In addition, in Figure 22, the UPS measurement at kinetic energy uses the cutoff at the low binding energy of the Ag foil in the sample holder as the reference point (0 eV). However, if the UPS ionization energies had been calculated based on the vacuum level, the band structure of SbSe\_500 would have shown lower ionization energies compared to that of SbSe\_0 due to its lower work function value. Therefore, SbSe\_500 may not exhibit a spike-like energy barrier for photo-excited electrons in an energy band

alignment with CdS buffer layer in a typical thin film solar cell, as the work function of CdS thin film is reported to be approximately 3.91 eV [107].

Any post-thermal treatment can alter the crystallinity and defect structure of a semiconductor material. The Sn doping method employed on SbSe<sub>0</sub> (the reference sample), which involved annealing at different temperatures in the presence of SnSe<sub>2</sub> pellets, is also a thermal process. To understand whether the differences in the Fermi energy level and the work function derived from the UPS data on SbSe<sub>500</sub> are solely attributable to Sn-doping or if they also reflect contributions from the annealing temperature, the UPS analysis was repeated on a parallel series of Sb<sub>2</sub>Se<sub>3</sub> polycrystals that were subjected to the same temperatures and durations without the inclusion of SnSe<sub>2</sub> pellets. The post-annealed undoped Sb<sub>2</sub>Se<sub>3</sub> revealed a decreased work function by around 0.3 eV compared to SbSe<sub>0</sub>, while the difference in work functions between SbSe<sub>0</sub> and SbSe<sub>500</sub> was more than 1 eV. This indicates that there is also an effect of temperature on the band structure of Sb<sub>2</sub>Se<sub>3</sub>, which is however significantly smaller than the effect of Sn-doping. Additionally, although  $E_f - E_{VB}$  was smaller in SbSe<sub>500</sub> than it was in SbSe<sub>0</sub>, the difference of  $E_f - E_{VB} = 0.62$  meV in SbSe<sub>0</sub> remained unchanged for the undoped Sb<sub>2</sub>Se<sub>3</sub> post-annealed at 500 °C. On the other hand, to compare the effect of post-thermal treatment and Sn-doping on Sb<sub>2</sub>Se<sub>3</sub> at the same process temperature, it is crucial to consider their respective partial chemical pressures. At 500 °C, Sb<sub>2</sub>Se<sub>3</sub> and SnSe<sub>2</sub> have partial pressures of 0.45 Torr [108] and 0.75 Torr [109], respectively, while the contribution from elemental Sb and Sn are negligible. At 500 °C, the partial pressure of selenium, derived from either SnSe<sub>2</sub> or Sb<sub>2</sub>Se<sub>3</sub> sources, is the highest due to its volatility, resulting in high pressures at elevated temperatures. However, the partial pressure of selenium from either Sb<sub>2</sub>Se<sub>3</sub> or SnSe<sub>2</sub> is significantly lower than what would be obtained from pure selenium [110]. The reported values above suggest that the partial pressures from the dopant SnSe<sub>2</sub> can exceed those from Sb<sub>2</sub>Se<sub>3</sub> in the tin doping method applied in this study. There is no balancing pressure for Sb<sub>2</sub>Se<sub>3</sub> during the post-thermal treatment in vacuum at 500 °C, where partial pressure from elemental selenium may lead to generation of selenium vacancies. Therefore, it can be concluded that the results from the UPS analysis on SbSe<sub>500</sub>, when compared to the reference sample (SbSe<sub>0</sub>), primarily arise from the introduction of Sn into Sb<sub>2</sub>Se<sub>3</sub>.

In the final step, UV-Vis spectroscopy in reflection measurement mode was used to determine the band gap energy of the studied samples SbSe<sub>0</sub> and SbSe<sub>500</sub>. Transmittance spectra could not be measured due to the high absorption coefficient of Sb<sub>2</sub>Se<sub>3</sub> in the visible range, as well as the large particle size of the polycrystalline powder samples ranging from 50 to 100 μm in diameter. The absorption coefficient, which matches values reported in the literature [111][112], for both samples was calculated as  $4.5 \times 10^4$  cm<sup>-1</sup>. As shown in Figure 24, the same band gap energy value of 1.25 eV at RT was found from the reflectance spectra by using the Tauc plot of Kubelka–Munk transformation ( $F(R)$ ) [113][114] for both samples. The band gap energy of Sb<sub>2</sub>Se<sub>3</sub> does not change after the Sn-doping process since the level of Sn incorporation in SbSe<sub>500</sub> remained at the doping level as was confirmed by the XRD, EDS and XPS analyses.

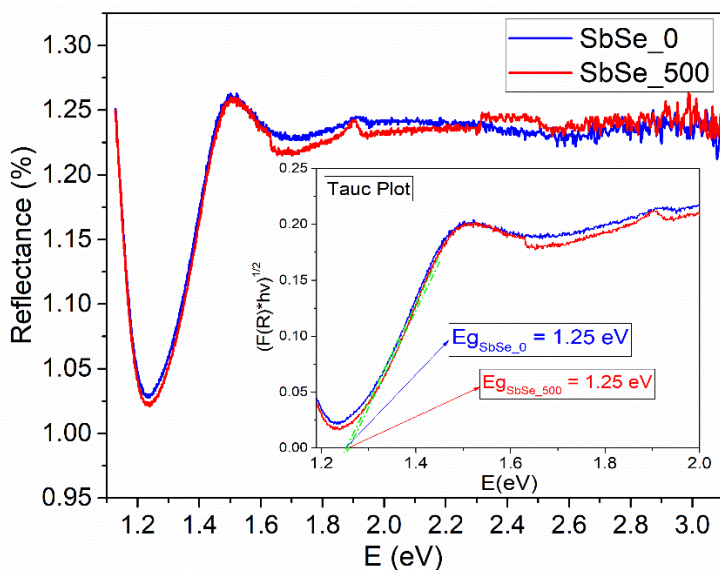


**Figure 24.** Reflectance spectra measured by UV-Vis spectroscopy and bandgap energy values calculated by using the Tauc plot for SbSe<sub>0</sub>, and for SbSe<sub>500</sub>.

The information regarding the work function of undoped and Sn-doped Sb<sub>2</sub>Se<sub>3</sub> absorbers enables a more precise design of the *p-n* junction interface between the undoped as well as Sn-doped Sb<sub>2</sub>Se<sub>3</sub> absorber and a potential n-type buffer layer. An optimized *p-n* junction interface is essential for achieving high-performance Sb<sub>2</sub>Se<sub>3</sub> solar cells, alongside optimal carrier concentration and reduced recombination losses.

### 3.3 Enhanced control of the grain orientation in Sb<sub>2</sub>Se<sub>3</sub> thin films

The research in this section presents a controllable method for depositing Sb<sub>2</sub>Se<sub>3</sub> thin films with highly oriented grains along the *c*-axis and a compact morphology aiming at improved solar cell device performance. A combination of magnetron sputtering and post-deposition isothermal selenization techniques was used.

#### 3.3.1 Composition and morphology of the Sb<sub>2</sub>Se<sub>3</sub> thin films

The RF-sputtered Sb film on the Mo/BSG substrate had a thickness of approximately 315 nm, as determined from the cross-section SEM image shown in Figure 25a. The uniform surface morphology of the Sb film can be seen in Figure 25b. These Sb films were subsequently selenized at different temperatures ranging from 380 °C to 420 °C, using different Ar-pressures ranging from 200 to 300 Torr to obtain Sb<sub>2</sub>Se<sub>3</sub> thin films. The optimal selenization temperature was found to be between 380–400 °C.

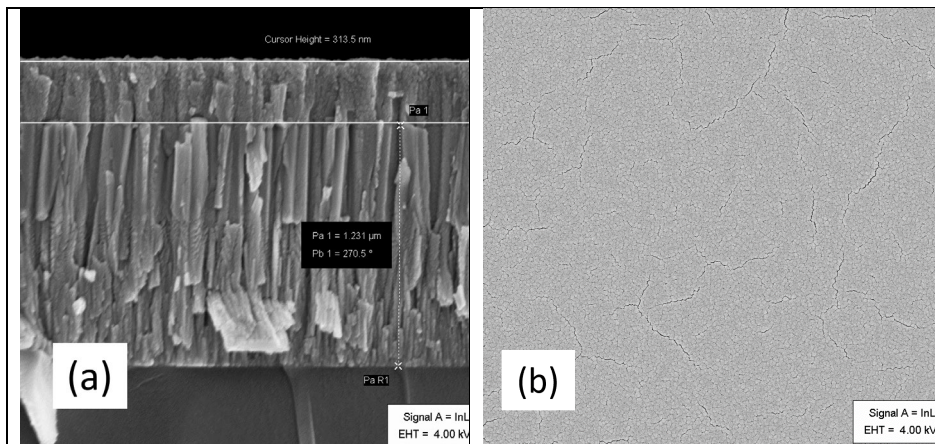


**Figure 25.** SEM images of a) cross section, and b) top-view of sputtered Sb film on Mo/BSG.

A higher selenization temperature of 420 °C may result in better vertical growth with the preferred orientation, as Tang et al. [68] also suggests that the preferred grain orientations [221], [211], and [001] of  $\text{Sb}_2\text{Se}_3$  to the substrate's surface require higher surface energies ( $\text{J}/\text{m}^2$ ) than other non-preferred ones. However, the enhanced vertical growth of  $\text{Sb}_2\text{Se}_3$  grains at higher selenization temperature can disturb the surface compactness, potentially leading to shunt paths in a  $\text{Sb}_2\text{Se}_3/\text{CdS}$ -based thin film solar cell, as can be seen from the SEM image in Figure 26. Therefore, finding an optimal balance between grain orientation and surface compactness is crucial. In the following, four samples were chosen based on the uniformity and repeatability of the  $\text{Sb}_2\text{Se}_3$  films for further study. The selected Sb/Mo/BSG thin films were selenized at 380 °C and 400 °C for 30 minutes, accompanied by two different Ar-pressures. The samples labelled as SbSe\_380-200, SbSe\_400-200, SbSe\_380-300, SbSe\_400-300 are described in Table 5.

It was found that selenization of Sb/Mo/BSG films without the presence of any inert gas, such as argon, leads to elemental Se reacting very aggressively with Sb in the selenization temperature range used in this study. This results in severe surface degradation and detachment of the  $\text{Sb}_2\text{Se}_3$  layer from the Mo/BSG substrates an example is shown in Figure 26. With the reference to Table 5, when 200 Torr and 300 Torr of Ar-pressures are filled into 25 ml quartz ampoules at RT, the pressure at 380 °C should reach approximately 440 Torr and 660 Torr, respectively. At 400 °C, the pressure should be around 453 Torr and 675 Torr, respectively, assuming the ideal gas behaviour in an isolated system. On the other hand, the Se vapor pressure originating from elemental Se-bead at 380 °C and 400 °C is lower than the partial Ar-pressure at the same temperatures. This is because the boiling point of Se at 1 atm (760 Torr) is approximately 685 °C [110].

**Table 5.** Selenization process parameters of Sb/Mo/BSG thin films.

Sample name	Selenization temperature, °C	Ar pressure at RT, Torr
SbSe_380-200	380	200
SbSe_380-300	380	300
SbSe_400-200	400	200
SbSe_400-300	400	300

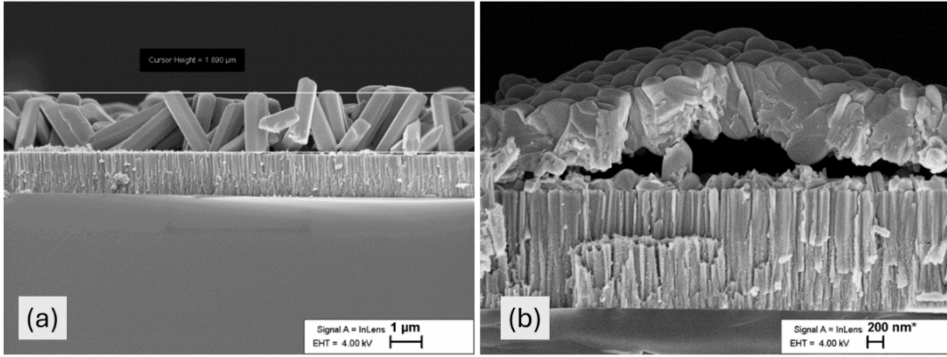


**Figure 26.** a) A cross-section SEM image of SbSe\_420-200: Sb/Mo/BSG thin film, which was selenized at 420 °C for 30 minutes in preheated cylindrical furnace using 200 Torr of Ar-gas pressure at RT. Thickness of the uncompact thin film is 1.8 μm, b) a cross-section SEM image of SbSe\_380-00: Sb/Mo/BSG thin film, which was selenized at 380 °C for 30 minutes without the presence of any inert gas. The absence of the inert gas resulted in the detachment of the Sb<sub>2</sub>Se<sub>3</sub> layer from the Mo/BSG substrate.

It is expected that the difference between partial pressures of Se vapor and Ar-gas inside the quartz ampoule will influence the Se-Sb reaction rate on the Mo/BSG substrate and the Se saturation in the Sb<sub>2</sub>Se<sub>3</sub> thin film. Therefore, the elemental composition of the studied Sb<sub>2</sub>Se<sub>3</sub> thin films was determined by EDS analysis and is shown in Table 6. Although the difference in the Se/Sb ratio among the studied samples remains close to the margin of EDS measurement error, the extreme samples SbSe\_380-200 and SbSe\_400-300 exhibit slightly more Se-rich compositions.

**Table 6.** Elemental compositions by EDS and the thickness of the Sb<sub>2</sub>Se<sub>3</sub> film from SEM cross-sectional images of the studied Sb<sub>2</sub>Se<sub>3</sub> thin-film samples.

	Antimony at. %	Selenium at. %	Thickness, nm
SbSe_380-200	37.5 ± 1.1	62.5 ± 1.2	640
SbSe_380-300	41.5 ± 1.3	58.5 ± 1.3	660
SbSe_400-200	40.6 ± 1.1	59.4 ± 1.1	1310
SbSe_400-300	38.1 ± 1.0	61.9 ± 1.1	870

Figure 27 and Figure 28 show the top view and cross-sectional SEM images of Sb<sub>2</sub>Se<sub>3</sub> thin films prepared by varying the selenization temperature and Ar-pressure. All studied samples have columnar and highly crystallized grain structures. Namely, the samples SbSe\_400-200 (Figure 28 a, c) and SbSe\_400-300 (Figure 28 b, d), selenized at higher temperature of 400 °C, exhibit irregular morphology with micro-voids in the Sb<sub>2</sub>Se<sub>3</sub> film. However, these films also feature longer columnar grains with the lengths up to 2 μm and width of up to 700 nm. On the other hand, a lower selenization temperature of 380 °C for the samples SbSe\_380-200 (Figure 27 a, c) and SbSe\_380-300 (Figure 27 b, d) resulted in more densely packed grains. The isothermally selenized samples, which were prepared using lower Ar-pressure of 200 Torr, SbSe\_380-200 and SbSe\_400-200, showed narrower columnar grains with widths up to 570 nm.

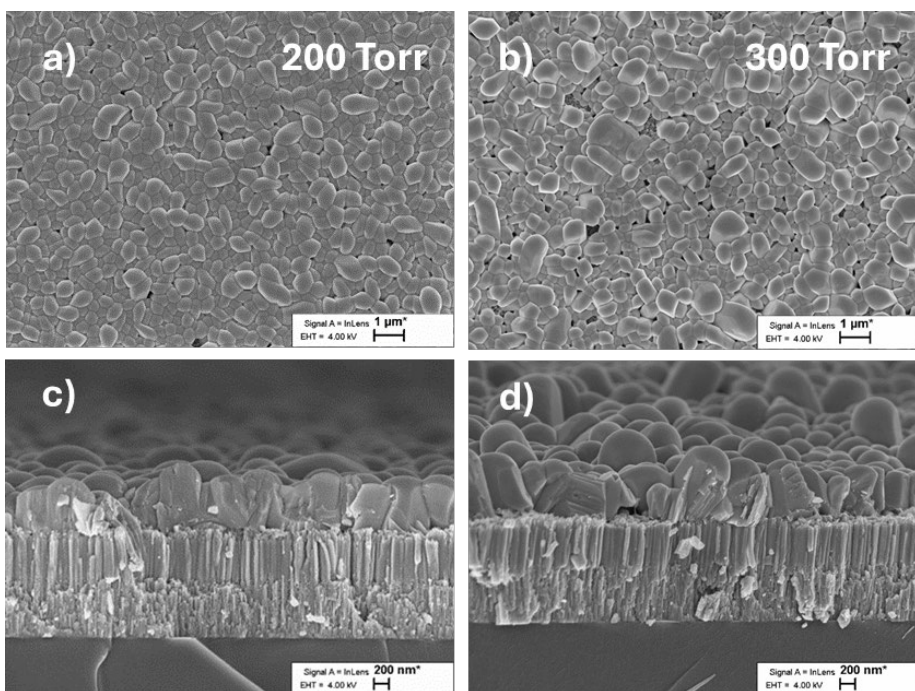


**Figure 27.** SEM images of surface (a, b) and corresponding cross-sections (c, d) of  $Sb_2Se_3$  thin film selenized at 380 °C under different Ar-pressure.

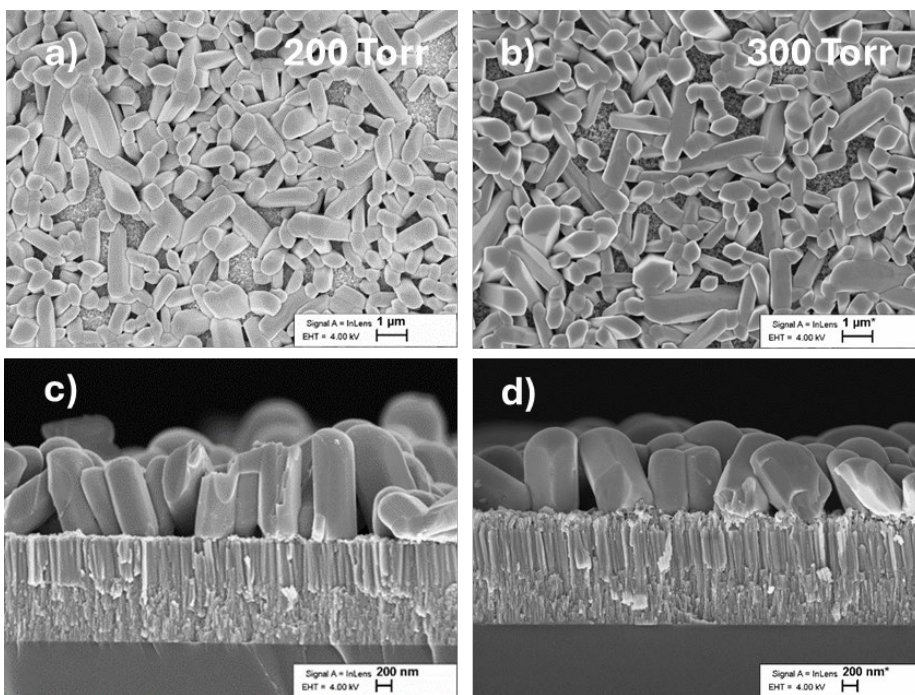


**Figure 28.** SEM images of surface (a, b) and corresponding cross-sections (c, d) of  $Sb_2Se_3$  thin film selenized at 400 °C under different Ar-pressure.

The RT micro-Raman spectra, measured by scanning multiple spots on the surfaces of the samples, were found to be identical across the surface of each sample. The resolved Raman spectra of SbSe\_380-200 and SbSe\_380-300, with Lorentzian peaks used for the fitting shown in Figure 29, indicate that the crystallinity of both samples is satisfactory, compared to the Raman spectra from the polycrystalline materials in Figure 19a. This conclusion is based on the narrow FWHM values of the main Raman shift ( $A_g^2$ ) at  $191\text{ cm}^{-1}$ , as demonstrated by the comparison between amorphous and crystalline thin films of  $\text{Sb}_2\text{Se}_3$  shown by Muskens et al. [115]. Angle-resolved and polarized Raman spectra of  $\text{Sb}_2\text{Se}_3$  studied by Jäckel et al. [116], suggested that the relative decrease in the intensity of the  $B_{2g}^1$  peak at  $155\text{ cm}^{-1}$ , and at the same time, a relative enhancement of the intensity of the  $B_{1g}^2$  peak at  $205\text{ cm}^{-1}$  [117], are linked to the preferred grain orientation of  $\text{Sb}_2\text{Se}_3$  in the [001] direction. The study of Jäckel et al. [116] also showed that it is possible to detect the grain orientation of [001] from the XRD analysis by using its equivalent counterpart indexed with [002] [15].

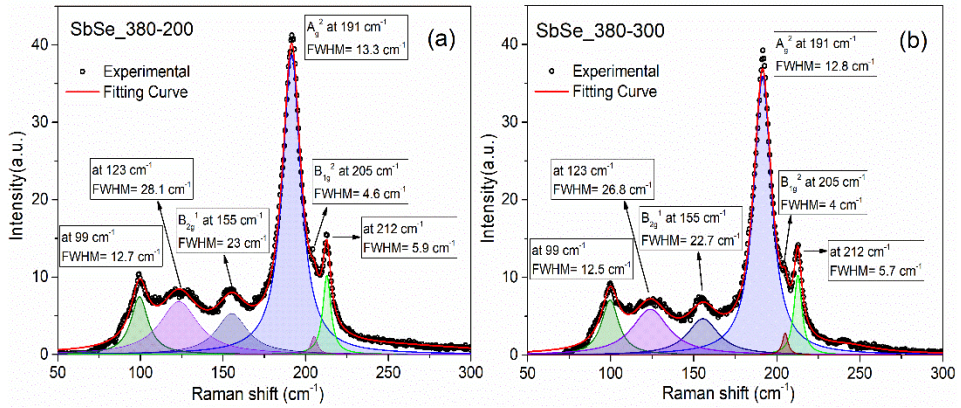


**Figure 29.** The resolved Raman spectra of (a)  $\text{Sb}_2\text{Se}_3/\text{Mo}/\text{BSG}$  thin-film synthesized at  $380\text{ }^\circ\text{C}$  under Ar-pressure 200 Torr at RT, (b)  $\text{Sb}_2\text{Se}_3/\text{Mo}/\text{BSG}$  thin-film synthesized at  $380\text{ }^\circ\text{C}$  under Ar-pressure 300 Torr-Ar at RT.

### 3.3.2 Grain orientation in the $\text{Sb}_2\text{Se}_3$ thin film

However, to gather more information about the crystallinity of the SbSe\_380-200 and SbSe\_380-300 samples, the XRD analysis was performed using ICDD 00-015-0861 card in the Rietveld analysis for  $\text{Sb}_2\text{Se}_3$ , as shown in Figure 30a. No secondary phases were detected, confirming the results by EDS and Raman analysis. As seen in Figure 30a, the relative XRD peak intensity of (002) along the c-axis dominates in both samples. The XRD peaks corresponding to the (hk1), (0k1), and particularly (002) planes are representative of vertically oriented  $\text{Sb}_2\text{Se}_3$  grains, as reported in the literature [15][53][116][118]. To comprehend better the relative XRD intensities, the texture coefficients (TC) of sixteen XRD peaks in Figure 30b were calculated using the following equation [15]:

$$TC_{hkl} = \frac{I(hkl)}{I_o(hkl)} / \left( \frac{1}{N} \sum_{i=1}^N \frac{I_i(hkl)}{I_{oi}(hkl)} \right). \quad (4)$$

In the equation (4),  $I(hkl)$  indicate to an experimentally obtained intensity of a reflection with  $hkl$  Miller indices,  $N$  is total number of all XRD peaks resolved in the Rietveld analysis,  $I_0(hkl)$  are standard intensities (a.u.) from the reference ICDD 00-015-0861 card, and  $I_i(hkl)$  are XRD intensities (a.u.) in this study. As a result, the sum of those preferred TC indexed (101), (021), (211), (221), (002), based on the sixteen XRD peaks ( $N = 16$ ), is 9 for SbSe\_380-200, and 10.2 for SbSe\_380-300. Therefore, as shown in Figure 30, the texture coefficients of the preferred orientations cumulatively dominate the XRD spectra by 56% and 63% for SbSe\_380-200 and SbSe\_380-300, respectively. The results of the XRD analysis complement the observations made from the SEM images in 27, confirming the enhanced grain orientations aligning with the c-axis of the Sb<sub>2</sub>Se<sub>3</sub>/Mo/BSG thin films. Unexpectedly, the texture coefficient in Figure 30b shows that the sample selenized at higher Ar-pressure, SbSe\_380-300, has stronger reflection from the (002) plane and it exhibits relatively larger grains as observed on the SEM images in 27. Nevertheless, some micro-voids located distinctly on the surfaces of SbSe\_380-200 and SbSe\_380-300 thin films were still observed on the SEM images. This challenge arises from the high anisotropy of Sb<sub>2</sub>Se<sub>3</sub> crystallites. It can be concluded that thicker RF-sputtered Sb and a selenization temperature lower than 380 °C can further enhance the surface compactness of Sb<sub>2</sub>Se<sub>3</sub> thin films. Additionally, performing a heat treatment on the antimony thin film (Sb/Mo/BSG) in an inert gas ambient or in vacuum before thermal selenization may influence the characteristics of the resulting Sb<sub>2</sub>Se<sub>3</sub> thin film. However, such a process would require additional optimization.

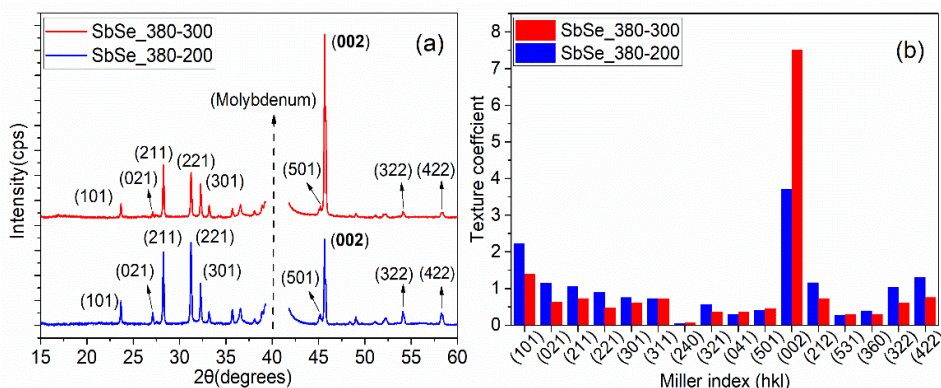


**Figure 30.** (a) XRD pattern of SbSe\_380-200 with blue, and SbSe\_380-300 with red. (b) XRD texture coefficients (TC) for sample SbSe\_380-200 (blue), and SbSe\_380-300 (red).

To test the Sb<sub>2</sub>Se<sub>3</sub> thin film with enhanced grain orientation in a solar cell device, a complete solar cell structure of ZnO:Al/CdS/Sb<sub>2</sub>Se<sub>3</sub>/Mo/BSG was fabricated as described in the experimental details of the manuscript. The cross-sectional SEM image of a complete device is presented in Figure 31.

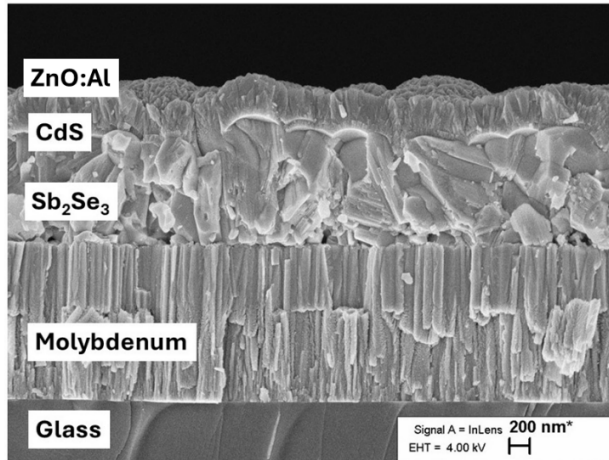


**Figure 31.** Cross-sectional SEM image of a ZnO:Al/CdS/Sb<sub>2</sub>Se<sub>3</sub>/Mo/BSG solar cell based on SbSe<sub>380-300</sub> thin film.

The I-V curve of the solar cell shown in Figure 32 a reveals a reverse leakage current of 0.1 mA and exhibits high serial resistance. The reverse leakage current observed in the I-V curve may be attributed to micro-voids on the surface of the Sb<sub>2</sub>Se<sub>3</sub> thin film. The EQE spectra of the solar cell shown in Figure 32b exhibits a reduced response in the wavelength range between 400 nm and 530 nm, as well as a diminished red response at wavelengths longer than 850 nm. The EQE reduction between 400 nm and 530 nm may be due to the recombination of photo-generated EHPs in the CdS/Sb<sub>2</sub>Se<sub>3</sub> junction area. Moreover, the reduced red response in the EQE suggests recombination of EHPs at the Sb<sub>2</sub>Se<sub>3</sub>/Mo back contact interface. This implies the need for a suitable hole transport layer in Sb<sub>2</sub>Se<sub>3</sub>/CdS-based solar cells [119] and optimization of the CdS buffer layer. In the literature a solar cell made from RF-magnetron sputtered Sb<sub>2</sub>Se<sub>3</sub>, followed by post-thermal selenization has demonstrated a PCE of 6.84%, showing higher  $V_{oc}$  and  $FF$  values compared to this study [73].

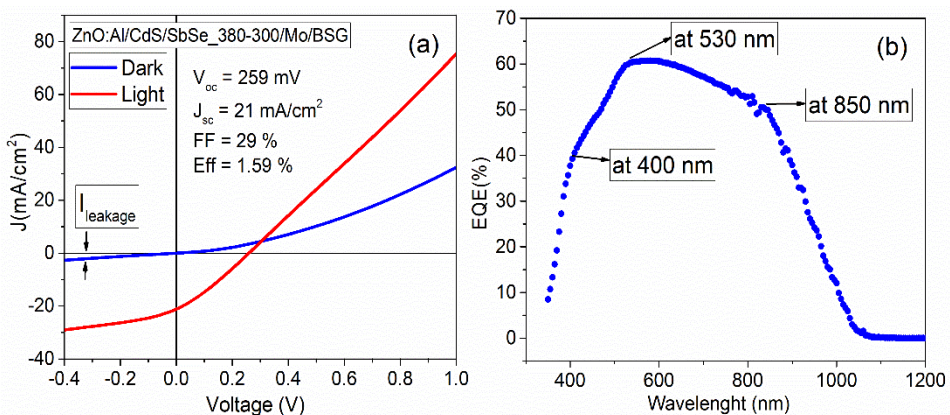


**Figure 32.** a) I-V curve of the solar cell based on SbSe<sub>380-300</sub> thin film, b) its EQE spectrum.

Although optimization of the complete thin film solar cell structure was not the focus of this study, a decent photocurrent density of 21 mA/cm<sup>2</sup> was achieved using SbSe\_380-300 with improved grain orientation as an absorber. This confirms the importance of the grain orientation for enhancing current production in the Sb<sub>2</sub>Se<sub>3</sub> based solar cells.

## Conclusions

The aim of this thesis was to investigate and tune the structural and optoelectronic properties limiting the power conversion efficiency of  $\text{Sb}_2\text{Se}_3$  solar cells. This was approached through alloying and doping strategies of  $\text{Sb}_2\text{Se}_3$  polycrystalline materials, and by developing a novel fabrication method for  $\text{Sb}_2\text{Se}_3$  thin film, aiming to enhance their quality for solar cell applications. Following conclusions can be made from the studies performed in the frame of this thesis:

1. Single phase  $\text{Sb}_2(\text{Se}_{1-x}\text{S}_x)_3$  ( $x = 0-1$ ) polycrystalline materials were successfully synthesized and their optical properties were studied by temperature and power dependent PL spectroscopy. The low-temperature ( $T = 3$  K) PL emission of  $\text{Sb}_2(\text{Se}_{1-x}\text{S}_x)_3$  solid solutions excited with a pulsed UV laser was found to shift towards higher energies from 1.309 eV to 1.728 eV with increasing sulphur content. The PL emission was found to have an excitonic origin in the samples with  $x = 0$  and 0.2 and resulting from the DD-DA pairs recombination in the samples with  $x = 0.4$  to  $x = 1$ . Asymmetric shape of the PL emission is result of the electron-phonon interaction. Electron-phonon interaction was found to be increased with the sulphur content ( $x$ ) in  $\text{Sb}_2(\text{Se}_{1-x}\text{S}_x)_3$  since  $\text{Sb}_2\text{S}_3$  has higher optical phonon (LO) energies.
2. An approach for Sn-doping of  $\text{Sb}_2\text{Se}_3$  polycrystalline material by isothermal annealing in the presence of  $\text{SnSe}_2$  at different temperatures was implemented. The Sn-doping was confirmed by the XPS analysis. The UPS study showed that Sn-doped  $\text{Sb}_2\text{Se}_3$  had a much smaller work function and a Fermi level slightly closer to the VBM compared to the undoped intrinsic  $\text{Sb}_2\text{Se}_3$  confirming slightly improved  $p$ -type conductivity of the  $\text{Sb}_2\text{Se}_3$  upon Sn-doping.
3. The desired grain orientation along the  $c$ -axis in  $\text{Sb}_2\text{Se}_3/\text{Mo}/\text{BSG}$  thin films was successfully achieved using magnetron sputtering method combined with post-deposition isothermal selenization. This was confirmed by the texture coefficient analysis and by the SEM analysis of the morphology of the  $\text{Sb}_2\text{Se}_3$  thin films. A balance between the preferred grain orientation in the [001] direction and the surface compactness of the thin films was found to be crucial for their use in thin film solar cell applications. Enhanced grain orientation closely aligning with the  $c$ -axis in the  $\text{Sb}_2\text{Se}_3$  thin film without compromising its surface compactness obtained with the selenization process at 380 °C after in a 300 Torr of Ar-pressure environment at RT. The developed method could pave the way for the fabrication of other quasi-1D chalcogenide thin films. To achieve higher PCEs in  $\text{Sb}_2\text{Se}_3$  thin film solar cells, further optimization of the device architecture is essential.

## References

- [1] [World Energy Outlook 2024 \(iea.blob.core.windows.net\)](http://iea.blob.core.windows.net), [The last access date: 28.10.2024]
- [2] [Snapshot of Global PV Markets - 2023 \(iea-pvps.org\)](http://iea-pvps.org), [The last access date: 28.10.2024]
- [3] H. Maghraoui-Meherzi, T. Ben Nasr, M. Dachraoui. Synthesis, structure and optical properties of  $\text{Sb}_2\text{Se}_3$ , *Materials Science in Semiconductor Processing* 16 (2013) 179–184, <https://doi.org/10.1016/j.mssp.2012.04.019>
- [4] Chao Chen, Kanghua Li, and Jiang Tang, Ten Years of  $\text{Sb}_2\text{Se}_3$  Thin Film Solar Cells, *Sol. RRL* 2022, 6, 2200094, <https://doi.org/10.1002/solr.202200094>
- [5] X. Liu, J. Chen, M. Luo, M. Leng, Z. Xia, Y. Zhou, S. Qin, D.-J. Xue, L. Lv, H. Huang, D. Niu, J. Tang. Thermal Evaporation and Characterization of  $\text{Sb}_2\text{Se}_3$  Thin Film for Substrate  $\text{Sb}_2\text{Se}_3/\text{CdS}$  Solar Cells, *ACS Appl. Mater. Interfaces* 6 (2014) 10687–10695, <https://doi.org/10.1021/am502427s>
- [6] Yuqi Zhao, Shaoying Wang, Chuang Li, Bo Che, Xueling Chen, Hongyi Chen, Rongfeng Tang, Xiaomin Wang, Guilin Chen, Ti Wang, Junbo Gong, Tao Chen, Xudong Xiao and Jianmin Li. Regulating deposition kinetics via a novel additive-assisted chemical bath deposition technology enables fabrication of 10.57%-efficiency  $\text{Sb}_2\text{Se}_3$  solar cells, *Energy Environ. Sci.*, 2022,15, 5118–5128, <https://doi.org/10.1039/D2EE02261C>
- [7] Zhaoteng Duan, Xiaoyang Liang, Yang Feng, Haiya Ma, Baolai Liang, Ying Wang, Shiping Luo, Shufang Wang, Ruud E. I. Schropp, Yaohua Mai, and Zhiqiang Li.  $\text{Sb}_2\text{Se}_3$  Thin-Film Solar Cells Exceeding 10% Power Conversion Efficiency Enabled by Injection Vapor Deposition Technology, *Adv. Mater.* 2022, 34, 2202969, <https://doi.org/10.1002/adma.202202969>
- [8] Yuqi Zhao, Shaoying Wang, Chenhui Jiang, Chuang Li, Peng Xiao, Rongfeng Tang, Junbo Gong, Guilin Chen, Tao Chen, Jianmin Li, Xudong Xiao. Regulating Energy Band Alignment via Alkaline Metal Fluoride Assisted Solution Post-Treatment Enabling  $\text{Sb}_2(\text{S}, \text{Se})_3$  Solar Cells with 10.7% Efficiency, *Adv. Energy Mater.* 2022, 12, 2103015. <https://doi.org/10.1002/aenm.202103015>
- [9] Yuqi Zhao, Shaoying Wang, Chenhui Jiang, Chuang Li, Peng Xiao, Rongfeng Tang, Junbo Gong, Guilin Chen, Tao Chen, Jianmin Li, and Xudong Xiao. Advances on  $\text{Sb}_2\text{Se}_3$  Solar Cells Fabricated by Physical Vapor Deposition Techniques, *Solar* 2023, 3(4), 566–95. <https://doi.org/10.3390/solar3040031>
- [10] Zhiqiang Li, Xiaoyang Liang, Gang Li, Haixu Liu, Huiyu Zhang, Jianxin Guo, Jingwei Chen, Kai Shen, Xingyuan San, Wei Yu, Ruud E.I. Schropp, and Yaohua Mai. 9.2%-efficient core-shell structured antimony selenide nanorod array solar cells, *Nature Communications* 10:125 (2019), <https://doi.org/10.1038/s41467-018-07903-6>
- [11] Ying Zhou, Liang Wang, Shiyong Chen, Sikai Qin, Xinsheng Liu, Jie Chen, Ding-Jiang Xue, Miao Luo, Yuanzhi Cao, Yibing Cheng, Edward H. Sargent and Jiang Tang. Thin-film  $\text{Sb}_2\text{Se}_3$  photovoltaics with oriented one-dimensional ribbons and benign grain boundaries, *Nature Photonics* 9 (2015) 409–415, <https://doi.org/10.1038/nphoton.2015.78>

- [12] Taifeng Jua, Bonkee Kooa, Jea Woong Job, and Min Jae Koa. Enhanced photovoltaic performance of solution-processed  $\text{Sb}_2\text{Se}_3$  thin film solar cells by optimizing device structure, *Current Applied Physics* 20 (2020) 282–287, <https://doi.org/10.1016/j.cap.2019.11.018>
- [13] Menglin Huang, Peng Xu, Dan Han, Jiang Tang, and Shiyong Chen. Complicated and unconventional defect properties of the quasio- dimensional photovoltaic semiconductor  $\text{Sb}_2\text{Se}_3$ , *ACS Appl. Mater. Interfaces* 11 (2019) 15564–15572, <https://doi.org/10.1021/acsami.9b01220>.
- [14] Christopher N. Savory, and Davis O. Scaldon. The complex defect chemistry of antimony selenide, *J. Mater. Chem. A* 7 (2019) 10739, <https://doi.org/10.1039/C9TA02022E>
- [15] F. Pattini, S. Rampino, F. Mezzadri, D. Calestani, G. Spaggiari, M. Sidoli, D. Delmonte, A. Sala, E. Gilioli, and M. Mazzer. Role of the substrates in the ribbon orientation of  $\text{Sb}_2\text{Se}_3$  films grown by Low-Temperature Pulsed Electron Deposition, *Solar Energy Materials & Solar Cells* 218 (2020) 110724, <https://doi.org/10.1016/j.solmat.2020.110724>
- [16] Xixing Wen, Zonghuan Lu, Xuke Yang, Chao Chen, Morris A. Washington, Gwo-Ching Wang, Jiang Tang, Qiang Zhao, and Toh-Ming Lu. Vertically Aligned One-Dimensional Crystal-Structured  $\text{Sb}_2\text{Se}_3$  for High-Efficiency Flexible Solar Cells via Regulating Selenization Kinetics, *ACS Appl. Mater. Interfaces* 2023, 15, 18, 22251–22262, <https://doi.org/10.1021/acsami.3c01830>
- [17] Rong Tang, Zhuang-Hao Zheng, Zheng-Hua Su, Xue-Jin Li, Ya-Dong Wei, Xiang-Hua Zhang, Yong-Qing Fu, Jing-Ting Luo, Ping Fan, and Guang-Xing Liang. Highly efficient and stable planar heterojunction solar cell based on sputtered and post-selenized  $\text{Sb}_2\text{Se}_3$  thin film, *Nano Energy* 64 (2019) 103929, <https://doi.org/10.1016/j.nanoen.2019.103929>
- [18] Guangzhuang Sun, Bo Li, Jia Li, Zhengwei Zhang, Huifang Ma, Peng Chen, Bei Zhao, Ruixia Wu, Weiqi Dang, Xiangdong Yang, Xuwan Tang, Chen Dai, Ziwei Huang, Yuan Liu, Xidong Duan, and Xiangfeng Duan. Direct van der Waals epitaxial growth of 1D/2D  $\text{Sb}_2\text{Se}_3/\text{WS}_2$  mixed-dimensional p-n heterojunctions, *Nano Research* 12(5) (2019) 1139–1145. <https://doi.org/10.1007/s12274-019-2364-1>
- [19] Jing Zhou, Dan Meng, Tinghe Yang, Xintong Zhang, Zheqing Tang, Yu Cao, Jian Ni, Jianjun Zhang, Ziyang Hu, Jinbo Pang. Enhanced charge carrier transport via efficient grain conduction mode for  $\text{Sb}_2\text{Se}_3$  solar cell applications, *Applied Surface Science* 591 (2022) 153169. <https://doi.org/10.1016/j.apsusc.2022.153169>
- [20] Theodore D. C. Hobson, Laurie J. Phillips, Oliver S. Hutter, Huw Shiel, Jack E. N. Swallow, Christopher N. Savory, Pabitra K. Nayak, Silvia Mariotti, Bhaskar Das, Leon Bowen, Leanne A. H. Jones, Thomas J. Featherstone, Matthew J. Smiles, Mark A. Farnworth, Guillaume Zoppi, Pardeep K. Thakur, Tien-Lin Lee, Henry J. Snaith, Chris Leighton, David O. Scanlon, Vinod R. Dhanak, Ken Durose, Tim D. Veal, and Jonathan D. Major. Isotype Heterojunction Solar Cells Using n-Type  $\text{Sb}_2\text{Se}_3$  Thin Films, *Chem. Mater.* 2020, 32, 2621–2630, <https://doi.org/10.1021/acs.chemmater.0c00223>
- [21] Shuo Chen, Xvsheng Qiao, Zhuanghao Zheng, Michel Cathelinaud, Hongli Ma, Xianping Fan and Xianghua Zhang. Enhanced electrical conductivity and photoconductive properties of Sn-doped  $\text{Sb}_2\text{Se}_3$  crystals, *J. Mater. Chem. C*, 2018, 6, 6465, <https://doi.org/10.1039/C8TC01683F>

- [22] D. M. Chapin, C. S. Fuller, and G. L. Pearson. A New Silicon p-n Junction Photocell for Converting Solar Radiation into Electrical Power, *Journal of Applied Physics* 25, 676 (1954), <https://doi.org/10.1063/1.1721711>
- [23] A.R. Zanatta. The Shockley–Queisser limit and the conversion efficiency of silicon-based solar cells, *Results in Optics* 9 (2022) 100320, <https://doi.org/10.1016/j.rio.2022.100320>
- [24] Nancy M. Haegel , Pierre Verlinden, Marta Victoria, and Pietro Altermatt et al. Photovoltaics at multi-terawatt scale: Waiting is not an option, 7 APRIL 2023 VOL 380 ISSUE 6640, <https://doi.org/10.1126/science.adf6957>
- [25] Cumulative installed solar PV capacity worldwide from 2000 to 2023, <https://www.statista.com/statistics/280220/global-cumulative-installed-solar-pv-capacity/>, [The last access date: 28.10.2024]
- [26] Fraunhofer Institute for Solar Energy Systems, ISE. Photovoltaics Report; ISE: Freiburg, Germany, 2023
- [27] Martin A. Green, Ewan D. Dunlop, Masahiro Yoshita, Nikos Kopidakis, Karsten Bothe, Gerald Siefer, Xiaojing Hao. Solar cell efficiency tables (version 62), *Prog Photovolt Res Appl.* 2023;31:651–663, <https://doi.org/10.1002/ppp.3726>
- [28] National Renewable Energy Laboratory (NREL) in Fall 2023 Solar Industry Update, <https://www.nrel.gov/docs/fy24osti/88026.pdf>
- [29] Martin A. Green, Keith Emery, Yoshihiro Hishikawa, Wilhelm Warta, Ewan D. Dunlop. Solar cell efficiency tables (version 46), *Prog. Photovoltaics Res. Appl.*, 23 (7) (2015) 805–812, <https://doi.org/10.1002/ppp.2637>
- [30] J. Keller, K. Kiselman, O. Donzel-Gargand, N. M. Martin, M. Babucci, O. Lundberg, E. Wallin, L. Stolt, M. Edoff. High-concentration silver alloying and steep back-contact gallium grading enabling copper indium gallium selenide solar cell with 23.6% efficiency, *Nat Energy* 9 (2024) 467–478, <https://doi.org/10.1038/s41560-024-01472-3>
- [31] Fei Ma, Yang Zhao, Zihan Qu, and Jingbi You. Developments of Highly Efficient Perovskite Solar Cells, *Acc. Mater. Res.* 4 (2023) 716–725, <https://doi.org/10.1021/accountsmr.3c00068>
- [32] <https://www.longi.com/en/news/2024-snec-silicon-perovskite-tandem-solar-cells-new-world-efficiency/>, Shanghai,China- June 14<sup>th</sup> - On June 14th, at the highly anticipated 2024 SNEC Expo in Shanghai, LONGi Green Energy Technology Co., Ltd. (hereinafter referred to as “LONGi”) announced a major breakthrough in the development of its silicon-perovskite tandem solar cells.
- [33] Kayes BM, Nie H, Twist R, et al. 27.6% conversion efficiency, a new record for single-junction solar cells under 1 sun illumination. In: *Proceedings of the 37th IEEE Photovoltaic Specialists Conference*; 2011.
- [34] Wanlass M. Systems and Methods for Advanced Ultra-High-Performance InP Solar Cells. US Patent 9,590,131 B2, 7 March 2017
- [35] NREL Best Research-Cell Efficiency Chart. Available online: <https://www.nrel.gov/pv/cell-efficiency.html>, [The last access date: 28.10.2024]

- [36] Xixing Wen, Zonghuan Lu, Gwo-Ching Wang, Morris A. Washington, Toh-Ming Lu. Efficient and stable flexible  $\text{Sb}_2\text{Se}_3$  thin film solar cells enabled by an epitaxial CdS buffer layer, *Nano Energy* 85 (2021) 106019, <https://doi.org/10.1016/j.nanoen.2021.106019>
- [37] G. Ghosh, The Sb-Se (antimony-selenium) system, *J. Phase Equilibria*. 14 (1993), <https://doi.org/10.1007/BF02667889>
- [38] Sergio Giraldo, Zacharie Jehl, Marcel Placidi, Victor Izquierdo-Roca, Alejandro Pérez-Rodríguez, and Edgardo Saucedo. Progress and Perspectives of Thin Film Kesterite Photovoltaic Technology: A Critical Review. *Adv. Mater.* 2019, 31, 1806692, <https://doi.org/10.1002/adma.201806692>
- [39] M. Grossberg, O. Volobujeva, A. Penezko, R. Kaupmees, T. Raadik, J. Krustok. Origin of photoluminescence from antimony selenide, *J. Alloys Compd* 817 (2020) 152716, <https://doi.org/10.1016/j.jallcom.2019.152716>
- [40] C. Chen, DC Bobela, Y. Yang, S. Lu, K. Zeng, C. Ge, B. Yang, L. Gao, Y. Zhao, MC Beard, J. Tang. Characterization of basic physical properties of  $\text{Sb}_2\text{Se}_3$  and its relevance for photovoltaics, *Front. Optoelectron.* 10 (1) (2017) 18–30, <https://doi.org/10.1007/s12200-017-0702-z>
- [41] Li Zhang, Yanbo Li, Changli Li, Qiao Chen, Zhen Zhen, Xin Jiang, Miao Zhong, Fuxiang Zhang, and Hongwei Zhu. Scalable Low-Band-Gap  $\text{Sb}_2\text{Se}_3$  Thin-Film Photocathodes for Efficient Visible–Near-Infrared Solar Hydrogen Evolution, *ACS Nano* 2017, 11, 12753–12763, <https://pubs.acs.org/doi/10.1021/acsnano.7b07512>
- [42] X. Wen, C. Chen, S. Lu, K. Li, R. Kondrotas, Y. Zhao, W. Chen, L. Gao, C. Wang, J. Zhang, and G. Niu. Vapor transport deposition of antimony selenide thin film solar cells with 7.6% efficiency, *Nat Commun* 9, 2179 (2018), <https://doi.org/10.1038/s41467-018-04634-6>
- [43] N. Spalatu, R. Krautmann, A. Katerski, E. Karber, R. Josepson, J. Hiie, I. Oja Acik, M. Krunks, Screening and optimization of processing temperature for  $\text{Sb}_2\text{Se}_3$  thin film growth protocol: Interrelation between grain structure, interface intermixing and solar cell performance, *Solar Energy Materials and Solar Cells*, 225 (2021) 111045, <https://doi.org/10.1016/j.solmat.2021.111045>
- [44] Chong Wang, Shuaicheng Lu, Sen Li, Siyu Wang, Xuetian Lin, Jun Zhang, Rokas Kondrotas, Kanghua Li, Chao Chen, Jiang Tang. Efficiency improvement of flexible  $\text{Sb}_2\text{Se}_3$  solar cells with non-toxic buffer layer via interface engineering, *Nano Energy* 71 (2020) 104577, <https://doi.org/10.1016/j.nanoen.2020.104577>
- [45] Shuaicheng Lu, Honghe Ding, Jun Hu, Yuhao Liu, Junfa Zhu, Rokas Kondrotas, Chao Chen, Jiang Tang. In situ investigation of interfacial properties of  $\text{Sb}_2\text{Se}_3$  heterojunctions, *Appl. Phys. Lett.* 116, 241602 (2020), <https://doi.org/10.1063/5.0008879>
- [46] L. Wang, D.B. Li, K. Li, C. Chen, H.X. Deng, L. Gao, Y. Zhao, F. Jiang, L. Li, F. Huang, Y. He. Stable 6%-efficient  $\text{Sb}_2\text{Se}_3$  solar cells with a ZnO buffer layer. Stable 6%-efficient  $\text{Sb}_2\text{Se}_3$  solar cells with a ZnO buffer layer, *Nat Energy* 2, 17046 (2017), <https://doi.org/10.1038/nenergy.2017.46>

- [47] Mykhailo Koltsov, Robert Krautmann, Atanas Katerski, Natalia Maticiuc, Malle Krunks, Ilona Oja Acik and Nicolae Spalatu. A post-deposition annealing approach for organic residue control in TiO<sub>2</sub> and its impact on Sb<sub>2</sub>Se<sub>3</sub>/TiO<sub>2</sub> device performance, *Faraday Discuss.*, 2022, 239, 273, <https://doi.org/10.1039/D2FD00064D>
- [48] Christopher H. Don, Thomas P. Shalvey, Daniya A. Sindi, Bradley Lewis, Jack E. N. Swallow, Leon Bowen, Daniel F. Fernandes, Tomas Kubart, Deepnarayan Biswas, Pardeep K. Thakur, Tien-Lin Lee, and Jonathan D. Major. Reactive DC Sputtered TiO<sub>2</sub> Electron Transport Layers for Cadmium-Free Sb<sub>2</sub>Se<sub>3</sub> Solar Cells, *Adv. Energy Mater.* 2024, 2401077, <https://doi.org/10.1002/aenm.202401077>
- [49] Jun Zhang, Rokas Kondrotas, Shuaicheng Lu, Chong Wang, Chao Chen, Jiang Tang. Alternative back contacts for Sb<sub>2</sub>Se<sub>3</sub> solar cells, *Solar Energy* 182 (2019) 96–101, <https://doi.org/10.1016/j.solener.2019.02.050>
- [50] Cong Liu, Kai Shen, Dongxu Lin, Ye Cao, Shudi Qiu, Jianzha Zheng, Feixiong Bao, Yanyan Gao, Hongbing Zhu, Zhiqiang Li, and Yaohua Mai. Back Contact Interfacial Modification in Highly Efficient All-Inorganic Planar n-i-p Sb<sub>2</sub>Se<sub>3</sub> Solar Cells, *ACS Applied Materials & Interfaces* 2020 12 (34), 38397–38405, <https://doi.org/10.1021/acsami.0c10629>
- [51] Yuyuan Ma, Yiwei Yin, Gang Li, Weitao Lian, Jianwang Zhang, Rongfeng Tang, Huanxin Jub and Tao Chen. Aqueous solution processed MoS<sub>3</sub> as an eco-friendly hole-transport layer for all-inorganic Sb<sub>2</sub>Se<sub>3</sub> solar cells, *Chem. Commun.*, 2020, 56, 15173, <https://doi.org/10.1039/D0CC05997H>
- [52] Oliver S. Hutter, Laurie J. Phillips, Ken Durose, Jonathan D. Major. 6.6% efficient antimony selenide solar cells using grain structure control and an organic contact layer, *Solar Energy Materials and Solar Cells* 188 (2018) 177–181, <https://doi.org/10.1016/j.solmat.2018.09.004>
- [53] R. Krautmann, N. Spalatu, R. Gunder, D. Abou-Ras, T. Unold, S. Schorr, M. Krunks, I. Oja Acik. Analysis of grain orientation and defects in Sb<sub>2</sub>Se<sub>3</sub> solar cells fabricated by close-spaced sublimation, *Solar Energy* 225 (2021) 494–500, <https://doi.org/10.1016/j.solener.2021.07.022>
- [54] Al Amin, Dian Li, Xiaomeng Duan, S. N. Vijayaraghavan, Harigovind G. Menon, Jacob Wall, Mark Weaver, Mark Ming-Cheng Cheng, Yufeng Zheng, Lin Li, and Feng Yan. Enhanced Efficiency and Stability in Sb<sub>2</sub>S<sub>3</sub> Seed Layer Buffered Sb<sub>2</sub>Se<sub>3</sub> Solar Cells, *Adv. Mater. Interfaces* 2022, 9, 2200547, <https://doi.org/10.1002/admi.202200547>
- [55] Christoph Freysoldt, Blazej Grabowski, Tilmann Hickel, Jörg Neugebauer, Georg Kresse, Anderson Janotti, and Chris G. Van de Walle. First-principles calculations for point defects in solids, *Adv. Mater. Interfaces* 2022, 9, 2200547, <https://doi.org/10.1103/RevModPhys.86.253>
- [56] Weitao Lian, Rui Cao, Gang Li, Huiling Cai, Zhiyuan Cai, Rongfeng Tang, Changfei Zhu, Shangfeng Yang, and Tao Chen. Distinctive Deep-Level Defects in Non-Stoichiometric Sb<sub>2</sub>Se<sub>3</sub> Photovoltaic Materials, *Adv. Sci.* 2022, 9, 2105268, <https://doi.org/10.1002/advs.202105268>
- [57] J. Hubbard. Electron correlations in narrow energy bands, *Proc. R. Soc. Lond.* A276238–257, <https://doi.org/10.1098/rspa.1963.0204>

- [58] Xinwei Wang, Seán R. Kavanagh, David O. Scanlon, and Aron Walsh. Four-electron negative-U vacancy defects in antimony selenide, *Phys. Rev. B* 108, 134102, <https://doi.org/10.1103/PhysRevB.108.134102>
- [59] Huaibing Song, Tiaoyang Li, Jia Zhang, Ying Zhou, Jiajun Luo, Chao Chen, Bo Yang, Cong Ge, Yanqing Wu, Jiang Tang. Highly Anisotropic Sb<sub>2</sub>Se<sub>3</sub> Nanosheets: Gentle Exfoliation from the Bulk Precursors Possessing 1D Crystal Structure, *Adv. Mater.* 2017, 29, 1700441, <https://doi.org/10.1002/adma.201700441>
- [60] Xinwei Wang, Zhenzhu Li, Seán R. Kavanagh, Alex M. Ganose and Aron Walsh. Lone pair driven anisotropy in antimony chalcogenide semiconductors, *Phys. Chem. Chem. Phys.*, 2022, 24, 7195, <https://doi.org/10.1039/D1CP05373F>
- [61] Nicolae Spalatu, Robert Krautmann, Atanas Katerski, Erki Karber, Raavo Josepson, Jaan Hiie, Ilona Oja Acik, Malle Krunks. Screening and optimization of processing temperature for Sb<sub>2</sub>Se<sub>3</sub> thin film growth protocol: Interrelation between grain structure, interface intermixing and solar cell performance, *Solar Energy Materials & Solar Cells* 225 (2021) 111045, <https://doi.org/10.1016/j.solmat.2021.111045>
- [62] N. Cifuentes, S. Ghosh, A. Shongolova, M. R. Correia, P. M. P. Salomé, P. A. Fernandes, S. Ranjbar, S. Garud, B. Vermang, G. M. Ribeiro, and J. C. González. Electronic Conduction Mechanisms and Defects in Polycrystalline Antimony Selenide, *J. Phys. Chem. C* 2020, 124, 14, 7677–7682, <https://doi.org/10.1021/acs.jpcc.0c00398>
- [63] Xincheng Liu, Yajun Qiao, Ya Liu, Jingling Liu, Erguang Jia, Songfeng Chang, Xingfen Shen, Shuang Li, Ke Cheng. Enhanced open circuit voltage of Sb<sub>2</sub>Se<sub>3</sub>/CdS solar cells by annealing Se-rich amorphous Sb<sub>2</sub>Se<sub>3</sub> films prepared via sputtering process, *Solar Energy* 195 (2020) 697–702, <https://doi.org/10.1016/j.solener.2019.11.072>
- [64] Weitao Lian, Rui Cao, Gang Li, Huiling Cai, Zhiyuan Cai, Rongfeng Tang, Changfei Zhu, Shangfeng Yang, Tao Chen. Distinctive Deep-Level Defects in Non-Stoichiometric Sb<sub>2</sub>Se<sub>3</sub> Photovoltaic Materials, *Adv. Sci.* 2022, 9, 2105268, <https://doi.org/10.1002/advs.202105268>
- [65] Xixing Wen, Chao Chen, Shuaicheng Lu, Kanghua Li, Rokas Kondrotas, Yang Zhao, Wenhao Chen, Liang Gao, Chong Wang, Jun Zhang, Guangda Niu and Jiang Tang. Vapor transport deposition of antimony selenide thin film solar cells with 7.6% efficiency, *Nat Commun* 9, 2179 (2018), <https://doi.org/10.1038/s41467-018-04634-6>
- [66] Xinwei Wang, Seán R. Kavanagh, David O. Scanlon, Aron Walsh. Upper efficiency limit of Sb<sub>2</sub>Se<sub>3</sub> solar cells, Volume 8, Issue 7, 17 July 2024, Pages 2105–2122, <https://doi.org/10.1016/j.joule.2024.05.004>
- [67] Volker L. Deringer, Ralf P. Stoffel, Matthias Wuttig and Richard Dronskowski. Vibrational properties and bonding nature of Sb<sub>2</sub>Se<sub>3</sub> and their implications for chalcogenide materials, *Chem. Sci.*, 2015,6, 5255–5262, <https://doi.org/10.1039/C5SC00825E>
- [68] Ying Zhou, Liang Wang, Shiyu Chen, Sikai Qin, Xincheng Liu, Jie Chen, Ding-Jiang Xue, Miao Luo, Yuanzhi Cao, Yibing Cheng, Edward H. Sargent & Jiang Tang. Thin-film Sb<sub>2</sub>Se<sub>3</sub> photovoltaics with oriented one-dimensional ribbons and benign grain boundaries, *Nature Photon* 9, 409–415 (2015), <https://doi.org/10.1038/nphoton.2015.78>

- [69] R.A. Lomas-Zapata, A.W. Prior, B.G. Mendis. A simulation study of the role of anisotropic charge transport and grain boundary recombination in thin-film  $\text{Sb}_2\text{Se}_3$  photovoltaics, *Solar Energy* 264 (2023) 112054, <https://doi.org/10.1016/j.solener.2023.112054>
- [70] Xinsheng Liu, Yongjun Liu, Shiqi Zhang, Xiaoman Sun, Yujun Zhuang, Jingling Liu, Gang Wang, Ke cheng, Zuliang Du. Regulating Deposition Pressures During Rapid Thermal Evaporation Processes to Enable Efficient  $\text{Sb}_2\text{Se}_3$  Solar Cells, *Small Methods* 2024, 8, 2300728, <https://doi.org/10.1002/smt.202300728>
- [71] Deng-Bing Li, Xinxing Yin, Corey R. Grice, Lei Guan, Zhaoning Song, Changlei Wang, Chao Chen, Kanghua Li, Alexander J. Cimaroli, Rasha A. Awni, Dewei Zhao, Haisheng Song, Weihua Tang, Yanfa Yan, Jiang Tang. Stable and efficient  $\text{CdS}/\text{Sb}_2\text{Se}_3$  solar cells prepared by scalable close space sublimation, *Nano Energy* 49 (2018) 346–353, <https://doi.org/10.1016/j.nanoen.2018.04.044>
- [72] Chenchen Yuan, Lijian Zhang, Weifeng Liu, Changfei Zhu. Rapid thermal process to fabricate  $\text{Sb}_2\text{Se}_3$  thin film for solar cell application, *Solar Energy* 137 (2016) 256–260, <https://doi.org/10.1016/j.solener.2016.08.020>
- [73] Guang-Xing Liang a , Yan-Di Luo a , Shuo Chen a , Rong Tang a , Zhuang-Hao Zheng, Xue-Jin Li b , Xin-Sheng Liu, Yi-Ke Liu, Ying-Fen Li, Xing-Ye Chen, Zheng-Hua Su, Xiang-Hua Zhang, Hong-Li Ma, Ping Fan. Sputtered and selenized  $\text{Sb}_2\text{Se}_3$  thin-film solar cells with open-circuit voltage exceeding 500 mV, *Nano Energy* 73 (2020) 104806, <https://doi.org/10.1016/j.nanoen.2020.104806>
- [74] Dan Liu, Rongfeng Tang, Yuyuan Ma, Chenhui Jiang, Weitao Lian, Gang Li, Wenhao Han, Changfei Zhu, and Tao Chen. Direct Hydrothermal Deposition of Antimony Triselenide Films for Efficient Planar Heterojunction Solar Cells, *ACS Appl. Mater. Interfaces* 2021, 13, 18856–18864, <https://doi.org/10.1021/acsami.1c02393>
- [75] Ke Li, Rongfeng Tang, Changfei Zhu, and Tao Chen. Critical Review on Crystal Orientation Engineering of Antimony Chalcogenide Thin Film for Solar Cell Applications, *Adv. Sci.* 2024, 11, 2304963, <https://doi.org/10.1002/adv.202304963>
- [76] Jianjun Li, Jialiang Huang, Kanghua Li, Yiyu Zeng, Yuanfang Zhang, Kaiwen Sun, Chang Yan, Chaowei Xue, Chao Chen, Tao Chen, Martin A. Green, Jiang Tang, Xiaojing Hao. Defect-Resolved Effective Majority Carrier Mobility in Highly Anisotropic Antimony Chalcogenide Thin-Film Solar Cells, *Sol. RRL* 2021, 5, 2000693, <https://doi.org/10.1002/solr.202000693>
- [77] Ying Zhou, Liang Wang, Shiyu Chen, Sikai Qin, Xinsheng Liu, Jie Chen, Ding-Jiang Xue, Miao Luo, Yuanzhi Cao, Yibing Cheng, Edward H. Sargent and Jiang Tang. Thin-film  $\text{Sb}_2\text{Se}_3$  photovoltaics with oriented one-dimensional ribbons and benign grain boundaries, *Nature Photon* 9, 409–415 (2015), <https://doi.org/10.1038/nphoton.2015.78>
- [78] Si-Nae Park, Se-Yun Kim, Sang-Ju Lee, Shi-Joon Sung, Kee-Jeong Yang, Jin-Kyu Kang, Dae-Hwan Kim. Facile growth of a  $\text{Sb}_2\text{Se}_3$  nanorod array induced by a  $\text{MoSe}_2$  interlayer and its application in 3D p–n junction solar cells, *Mater. Adv.*, 3 (2022) 978–985. <https://doi.org/10.1039/D1MA00804H>

- [79] Guangxing Liang, Xingye Chen, Donglou Ren, Xiangxing Jiang, Rong Tang, Zhuanghao Zheng, Zhenghua Su, Ping Fan, Xianghua Zhang, Yi Zhang, Shuo Chen. Ion doping simultaneously increased the carrier density and modified the conduction type of  $\text{Sb}_2\text{Se}_3$  thin films towards quasi-homojunction solar cell, *Journal of Materiomics* 7 (2021) 1324e1334, <https://doi.org/10.1016/j.jmat.2021.02.009>
- [80] H. M. Patel, S. P. Sikligar, P. D. Patel, P. B. Patel, H. N. Desai, J. M. Dhimmar and B. P. Modi. Recent Advances to Enhance Electrical and Photoelectrical Properties of Antimony Selenide Crystals via Tin Doping, *Journal of Electronic Materials* (2023) 52:196–208, <https://doi.org/10.1007/s11664-022-09963-3>
- [81] Theodore D C Hobson, Huw Shiel, Christopher N Savory, Jack E N Swallow, Leanne A H Jones, Thomas J Featherstone, Matthew J Smiles, Pardeep K Thakur, Tien-Lin Lee, Bhaskar Das. P-type conductivity in Sn-doped  $\text{Sb}_2\text{Se}_3$ , *J. Phys. Energy* 4 (2022) 045006, <https://doi.org/10.1088/2515-7655/ac91a6>
- [82] Yang Li, Ying Zhou, Yining Zhu, Chao Chen, Jiajun Luo, Jingyuan Ma, Bo Yang, Xiaojie Wang, Zhe Xia, Jiang Tang. Characterization of Mg and Fe doped  $\text{Sb}_2\text{Se}_3$  thin films for photovoltaic application, *Appl. Phys. Lett.* 109, 232104 (2016), <https://doi.org/10.1063/1.4971388>
- [83] Wen-Hui Li, Meng Li, Yu-Jie Hu, Chuan-Hui Cheng, Ze-Ming Kan, Dongqi Yu, Jing Leng, Shengye Jin, Shulin Cong. Enhanced performance of antimony selenide thin film solar cell using  $\text{PbI}_2$  as a dopant, *Appl. Phys. Lett.* 118, 093903 (2021), <https://doi.org/10.1063/5.0040940>
- [84] Chao Chen, Kanghua Li, Shiyong Chen, Liang Wang, Shuaicheng Lu, Yuhao Liu, Dengbing Li, Haisheng Song, and Jiang Tang. Efficiency Improvement of  $\text{Sb}_2\text{Se}_3$  Solar Cells via Grain Boundary Inversion, *ACS Energy Lett.* 2018, 3, 10, 2335–2341, <https://doi.org/10.1021/acscenergylett.8b01456>
- [85] Liu Jiajun, Liu Jianming, Liu Congqiang, Lu Wenquan, Liu Shirong and Su Wenchao. Mineralogy of the stibnite-antimonoselite series *Int. Geol. Rev.*, 41 (11) (1999), pp. 1042–1050, <https://doi.org/10.1080/00206819909465189>
- [86] Yiyu Zeng, Kaiwen Sun, Jialiang Huang, Michael P. Nielsen, Fan Ji, Chuhan Sha, Shengjie Yuan, Xueyun Zhang, Chang Yan, Xu Liu, Hui Deng, Yanqing Lai, Jan Seidel, Ned Ekins-Daukes, Fangyang Liu, Haisheng Song, Martin Green, and Xiaojing Hao. Quasi-Vertically Orientated Antimony Sulfide Inorganic Thin-Film Solar Cells Achieved by Vapor Transport Deposition, *ACS Appl. Mater. Interfaces* 2020, 12, 20, 22825–22834, <https://doi.org/10.1021/acscami.0c02697>
- [87] Yanlin Pan, Dongliang Zheng, Jianxin Chen, Jun Zhou, Rui Wang, Xingyu Pan, Xiaobo Hu, Shaoqiang Chen, Pingxiong Yang, Jiahua Tao, Junhao Chu. Controllable vapor transport deposition of efficient  $\text{Sb}_2(\text{S,Se})_3$  solar cells via adjusting evaporation source area, *Journal of Alloys and Compounds* 906 (2022) 164320, <https://doi.org/10.1016/j.jallcom.2022.164320>
- [88] Weihuang Wang, Xiaomin Wang, Guilin Chen, Binwen Chen, Hailing Cai, Tao Chen, Shuiyuan Chen, Zhigao Huang, Changfei Zhu, Yi Zhang. Promising  $\text{Sb}_2(\text{S,Se})_3$  Solar Cells with High Open Voltage by Application of a  $\text{TiO}_2/\text{CdS}$  Double Buffer Layer, *Sol. RRL* 2018, 2, 1800208, <https://doi.org/10.1002/solr.201800208>

- [89] Xueling Chen, Bo Che, Yuqi Zhao, Shaoying Wang, Hu Li, Junbo Gong, Guilin Chen, Tao Chen, Xudong Xiao, Jianmin Li. Solvent-Assisted Hydrothermal Deposition Approach for Highly-Efficient  $\text{Sb}_2(\text{S,Se})_3$  Thin-Film Solar Cells, *Adv. Energy Mater.* 2023, 13, 2300391, <https://doi.org/10.1002/aenm.202300391>
- [90] Hao Dong, Lijian Zhang, Bo Che, Peng Xiao, Haolin Wang, Changfei Zhu and Tao Chen. Hydrothermal Deposition of Antimony Selenosulfide on Titanium Oxide Nanoparticle Films for Cadmium-Free Solar Cells, *ACS Appl. Opt. Mater.* 2023, 1, 374–381, <https://doi.org/10.1021/acsaom.2c00075>
- [91] Weitao Lian, Rongfeng Tang, Yuyuan Ma, Chunyan Wu, Chao Chen, Xiaomin Wang, Fang Fang, Jianwang Zhang, Zheng Wang, Huanxin Ju, Changfei Zhu, Tao Chen. Probing the trap states in N–i–P  $\text{Sb}_2(\text{S,Se})_3$  solar cells by deep-level transient spectroscopy, *J. Chem. Phys.* 153, 124703 (2020), <https://doi.org/10.1063/5.0020244>
- [92] Jiashuai Li, Zheng Gao, Xuzhi Hu, Shuxin Wang, Yongjie Liu, Chen Wang, Kailian Dong, Zhaofeng Zeng, Chen Tao, Guojia Fang. Defects Passivation via Potassium Iodide Post-Treatment for Antimony Selenosulfide Solar Cells with Improved Performance, *Adv. Funct. Mater.* 2023, 33, 2211657, <https://doi.org/10.1002/adfm.202211657>
- [93] Nicole Fleck, Theodore D. C. Hobson, Christopher N. Savory, John Buckeridge, Tim D. Veal, Maria R. Correia, David O. Scanlon, Ken Durosea and Frank Jäkel. Identifying Raman modes of  $\text{Sb}_2\text{Se}_3$  and their symmetries using angle-resolved polarised Raman spectra, *J. Mater. Chem. A*, 2020,8, 8337–8344, <https://doi.org/10.1039/D0TA01783C>
- [94] Paolo Sereni, Maurizio Musso, Peter Knoll, Peter Blaha, Karlheinz Schwarz, Günther Schmidt. Polarization-Dependent Raman Characterization of Stibnite ( $\text{Sb}_2\text{S}_3$ ), *AIP Conference Proceedings* 1267, 1131 (2010), <https://doi.org/10.1063/1.3482339>
- [95] Y. A. Sorb, V. Rajaji, P. S. Malavi, U. Subbarao, P. Halappa, S. C. Peter, S. Karmakar and C. Narayana. Pressure-induced electronic topological transition in  $\text{Sb}_2\text{S}_3$ , 2016 *J. Phys.: Condens. Matter* 28 015602, doi: [10.1088/0953-8984/28/1/015602](https://doi.org/10.1088/0953-8984/28/1/015602)
- [96] Max Birkett, Wojciech M. Linhart, Jessica Stoner, Laurie J. Phillips, Ken Durose, Jonathan Alaria, Jonathan D. Major, Robert Kudrawiec, Tim D. Veal. Band gap temperature-dependence of close-space sublimation grown  $\text{Sb}_2\text{Se}_3$  by photo-reflectance, *Appl. Mater.* 6 (2018), 084901, <https://doi.org/10.1063/1.5027157>
- [97] Jüri Krustok, Rokas Kondrotas, Ramunas Nedzinskas, Kristi Timmo, Reelika Kaupmees, Valdek Mikli, Maarja Grossberg. Identification of excitons and biexcitons in  $\text{Sb}_2\text{Se}_3$  under high photoluminescence excitation density, *Adv. Opt. Mater.* 9 (2021) 2100107, <https://doi.org/10.1002/adom.202100107>.
- [98] J. Krustok, H. Collan and K. Hjelt. Does the low-temperature Arrhenius plot of the photoluminescence intensity in CdTe point towards an erroneous activation energy? *Journal of Applied Physics* 81, 1442–1445 (1997), <https://doi.org/10.1063/1.363903>
- [99] T. Schmidt, K. Lischka, W. Zulehner. Excitation-power dependence of the near-band-edge photoluminescence of semiconductors, *Phys. Rev. B* 45 (1992) 8989, <https://doi.org/10.1103/PhysRevB.45.8989>
- [100] K. Huang and A. Rhys. Theory of light absorption and non-radiative transitions in F-centres. *Proc. R. Soc. A* 204, 406–423 (1950), [https://doi.org/10.1142/9789812793720\\_0007](https://doi.org/10.1142/9789812793720_0007)

- [101] F. Williams. Donor—acceptor pairs in semiconductors. *Phys. Stat. Solidi* 25, 493–512 (1968), [doi:10.1002/pssb.19680250202](https://doi.org/10.1002/pssb.19680250202)
- [102] J. Krustok, J. Raudoja, M. Krunks, H. Mändar, and H. Collan. Nature of the native deep localized defect recombination centers in the chalcopyrite and orthorhombic AgInS<sub>2</sub>. *J. Appl. Phys.* v. 88, No 1, 205–209 (2000), <https://doi.org/10.1063/1.373644>
- [103] F. Aousgi, M. Kanzari. Study of the optical properties of the amorphous Sb<sub>2</sub>S<sub>3</sub> thin films, *J. Optoelectron. Adv. Mater.* 12 (2) (2010) 227–232.
- [104] Emma P. Mukhokosi, Saluru B. Krupanidhi & Karuna K. Nanda. Band Gap Engineering of Hexagonal SnSe<sub>2</sub> Nanostructured Thin Films for Infra-Red Photodetection, *Scientific Reports* volume 7, Article number: 15215 (2017), <https://doi.org/10.1038/s41598-017-15519-x>
- [105] Christopher H. Don, Huw Shiel, Theodore D. C. Hobson, Christopher N. Savory, Jack E. N. Swallow, Matthew J. Smiles, Leanne A. H. Jones, Thomas J. Featherstone, Pardeep K. Thakur, Tien-Lin Lee, Ken Durose, Jonathan D. Major, Vinod R. Dhanak, David O. Scanlon and Tim D. Veal. Sb 5s<sup>2</sup> lone pairs and band alignment of Sb<sub>2</sub>Se<sub>3</sub>: a photoemission and density functional theory study, *J. Mater. Chem. C*, 2020, 8, 12615. <https://doi.org/10.1039/D0TC03470C>
- [106] James E. Whitten. Ultraviolet photoelectron spectroscopy: Practical aspects and best practices, *Applied Surface Science Advances* 13 (2023) 100384. <https://doi.org/10.1016/j.apsadv.2023.100384>
- [107] Huw Shiel, Oliver S. Hutter, Laurie J. Phillips, Jack E. N. Swallow, Leanne A. H. Jones, Thomas J. Featherstone, Matthew J. Smiles, Pardeep K. Thakur, Tien-Lin Lee, Vinod R. Dhanak, Jonathan D. Major, and Tim D. Veal. Natural Band Alignments and Band Offsets of Sb<sub>2</sub>Se<sub>3</sub> Solar Cells, *ACS Appl. Energy Mater.* 2020, 3, 12, 11617–11626. <https://dx.doi.org/10.1021/acsaem.0c01477>
- [108] Xinsheng Liu, Jie Chen, Miao Luo, Meiyong Leng, Zhe Xia, Ying Zhou, Sikai Qin, Ding-Jiang Xue, Han Huang, Dongmei Niu, and Jiang Tang. Thermal Evaporation and Characterization of Sb<sub>2</sub>Se<sub>3</sub> Thin Film for Substrate Sb<sub>2</sub>Se<sub>3</sub>/CdS Solar Cells, *ACS Appl. Mater. Interfaces* 2014, 6, 10687–10695. <https://doi.org/10.1021/am502427s>
- [109] Liyong Yao, Jianping Ao, Ming-Jer Jeng, Jinlian Bi, Shoushuai Gao, Qing He, Zhiqiang Zhou, Guozhong Sun, Yun Sun, Liann-Be Chang and Jian-Wun Chen. CZTSe solar cells prepared by electrodeposition of Cu/Sn/Zn stack layer followed by selenization at low Se pressure, *Nanoscale Res Lett.* 2014; 9(1): 678, <https://doi.org/10.1186/1556-276X-9-678>
- [110] E. H. Baker. The vapour pressure and resistivity of selenium at high temperatures, *J. Chem. Soc. A*, 1968, 1089–1092. <https://doi.org/10.1039/J19680001089>
- [111] Xinsheng Liu, Jie Chen, Miao Luo, Meiyong Leng, Zhe Xia, Ying Zhou, Sikai Qin, Ding-Jiang Xue, Lu Lv, Han Huang, Dongmei Niu, and Jiang Tang. Thermal Evaporation and Characterization of Sb<sub>2</sub>Se<sub>3</sub> Thin Film for Substrate Sb<sub>2</sub>Se<sub>3</sub>/CdS Solar Cells, *ACS Appl. Mater. Interfaces* 2014, 6, 10687–10695. <https://doi.org/10.1021/am502427s>
- [112] Taifeng Ju, Bonkee Koo, Jea Woong Jo, Min Jae Ko. the Enhanced photovoltaic performance of solution-processed Sb<sub>2</sub>Se<sub>3</sub> thin film solar cells by optimizing device structure, *Current Applied Physics* 20 (2020) 282–287. <https://doi.org/10.1016/j.cap.2019.11.018>

- [113] Prince George and Pradip Chowdhury. Complex dielectric transformation of UV-vis diffuse reflectance spectra for estimating optical band-gap energies and materials classification, *Analyst*, 2019, 144, 3005-3012, [Analyst](https://doi.org/10.1039/C8AN02257G), 2019, 144, 3005–3012, <https://doi.org/10.1039/C8AN02257G>
- [114] A. I. Kontos, A. G. Kontos, Y. S. Raptis, P. Falaras. Nitrogen modified nanostructured titania: electronic, structural and visible-light photocatalytic properties, *phys. stat. sol. (RRL)* 2, No. 2, 83–85 (2008), <https://doi.org/10.1002/pssr.200802006>
- [115] Matthew Delaney, Ioannis Zeimpekis, Daniel Lawson, Daniel W. Hewak, and Otto L. Muskens. A New Family of Ultralow Loss Reversible Phase-Change Materials for Photonic Integrated Circuits:  $\text{Sb}_2\text{S}_3$  and  $\text{Sb}_2\text{Se}_3$ , *Adv. Funct. Mater.* 30 (2020) 2002447, <https://doi.org/10.1002/adfm.202002447>
- [116] Nicole Fleck, Theodore D. C. Hobson, Christopher N. Savory, John Buckeridge, Tim D. Veal, Maria R. Correia, David O. Scanlon, Ken Durose and Frank Jackel. Identifying Raman modes of  $\text{Sb}_2\text{Se}_3$  and their symmetries using angle-resolved polarised Raman spectra, *J. Mater. Chem. A* 8 (2020) 8337, <https://doi.org/10.1039/D0TA01783C>
- [117] Pedro Vidal-Fuentes, Maxim Guc, Xavier Alcobe, Tariq Jawhari, Marcel Placidi, Alejandro Pérez-Rodríguez, Edgardo Saucedo and Victor Izquierdo Roca. Multiwavelength excitation Raman scattering study of  $\text{Sb}_2\text{Se}_3$  compound: fundamental vibrational properties and secondary phases detection, *2D Mater.* 6 (2019) 045054, <https://doi.org/10.1088/2053-1583/ab4029>
- [118] Jimin Kim, Wooseok Yang, Yunjung Oh, Hyungsoo Lee, Seonhee Lee, Hyunjung Shin, Joosun Kim and Jooho Moon. Self-oriented  $\text{Sb}_2\text{Se}_3$  nanoneedle photocathodes for water splitting obtained by a simple spin-coating method, *J. Mater. Chem. A* 5 (2017) 2180–2187, <https://doi.org/10.1039/C6TA09602F>
- [119] Roberto Jakomin, Stefano Rampino, Giulia Spaggiari, Michele Casappa, Giovanna Trevisi, Elena Del Canale, Enos Gombia, Matteo Bronzoni, Kodjo Kekeli Sossue, Francesco Mezzadri and Francesco Pattini. Cu-Doped  $\text{Sb}_2\text{Se}_3$  Thin-Film Solar Cells Based on Hybrid Pulsed Electron Deposition/Radio Frequency Magnetron Sputtering Growth Techniques, *Solar* 4 (2024) 83–98, <https://doi.org/10.3390/solar4010004>

## **Acknowledgements**

I acknowledge my supervisor Prof. Maarja Grossberg-Kuusik for her contribution, guidance and motivation.

I appreciate the collaborative input of members of the Laboratory of Photovoltaic Materials from the Department of Materials and Environmental Technology at Tallinn University of Technology, and the co-authors from other institutions. I am especially grateful to Dr. Mati Danilson, Prof. Marit Kauk-Kuusik, Dr. Kristi Timmo, and Prof. Jüri Krustok for guiding me with different experiments and analysis.

This work was supported by the Estonian Research Council [grant number PRG1023]; M-ERA.net project LightCell [grant number MNHA23040]; and GREENTECH Project [grant number TK210].

Additionally, I dedicate the five years of effort in this study to my beloved father, Hidayet Uslu, who sadly passed away during my journey. His memory has been a source of strength throughout this work.

## Abstract

### Modification of the optoelectronic properties of Sb<sub>2</sub>Se<sub>3</sub> absorber material for photovoltaic applications

Antimony selenide (Sb<sub>2</sub>Se<sub>3</sub>) has emerged as a prospective absorber material for thin-film solar cells due to its quasi-one-dimensional (Q1D) nanoribbon structure, offering distinct advantages over other chalcogenide photovoltaic (PV) materials. These include low toxicity, an optimal bandgap (~ 1.2 eV at room temperature), a high absorption coefficient exceeding 10<sup>4</sup> cm<sup>-1</sup>, and a long minority carrier lifetime (approximately 60 ns). Additionally, the low melting point of Sb<sub>2</sub>Se<sub>3</sub> of 885 K enables low-temperature deposition, which would allow the reduction of the fabrication costs of thin films for PV. The crystallinity and the optoelectronic properties of the Sb<sub>2</sub>Se<sub>3</sub> thin films are significantly influenced by the growth conditions, including substrate type, deposition and post-treatment temperature and the chemical environment. These factors also impact the power conversion efficiency of solar cell device, which to date reaches close to 11%. Despite rapid advancements in power conversion efficiency, three main challenges persist for Sb<sub>2</sub>Se<sub>3</sub>-based solar cells: complex defect chemistry, low intrinsic carrier concentration, and anisotropic electrical properties dependent on crystal orientation.

The thesis is based on three peer-reviewed publications and addresses these challenges by investigating alloying and doping strategies and developing a novel approach for the fabrication of Sb<sub>2</sub>Se<sub>3</sub> thin films with high crystalline quality. In the first study in this thesis, antimony selenosulphide Sb<sub>2</sub>(Se<sub>1-x</sub>S<sub>x</sub>)<sub>3</sub> (x = 0–1) polycrystalline materials were synthesized from high purity elemental precursors with the aim to tune the optical properties of Sb<sub>2</sub>Se<sub>3</sub> by alloying with sulphur. The optical properties of Sb<sub>2</sub>(Se<sub>1-x</sub>S<sub>x</sub>)<sub>3</sub> solid solutions were analyzed for the first time using temperature- and power-dependent photoluminescence spectroscopy (PL), revealing the shift of the low-temperature PL emission from 1.309 eV to 1.728 eV as sulphur content increased. Samples with lower sulphur content (x ≤ 0.2) exhibited excitonic emission, while samples with x = 0.4 to x = 1 showed PL emission arising from deep-donor-deep-acceptor pair recombination. The detected asymmetric shape of the PL emission in the studied samples resulting from the electron-phonon interaction was found to increase with the sulphur content (x) in Sb<sub>2</sub>(Se<sub>1-x</sub>S<sub>x</sub>)<sub>3</sub> since Sb<sub>2</sub>S<sub>3</sub> has higher optical phonon (LO) energies.

In the second experimental study in this thesis, Sn-doping is applied on the Sb<sub>2</sub>Se<sub>3</sub> polycrystalline material with the aim to improve the p-type conductivity of the absorber material. Sn-doping was achieved by isothermal post-annealing four portions of Sb<sub>2</sub>Se<sub>3</sub> polycrystals at 350 °C, 400 °C, 450 °C, 500 °C, respectively, along with SnSe<sub>2</sub> pellets for 30 minutes in degassed and sealed quartz ampoules. Sn-doping was confirmed by X-ray photoelectron spectroscopy (XPS). Changes in the electronic band structure of intrinsic Sb<sub>2</sub>Se<sub>3</sub> resulting from Sn-doping were studied by ultraviolet photoelectron spectroscopy (UPS). UPS analysis showed reduction in the work function and a shift of the Fermi level closer to the valence band maximum of Sb<sub>2</sub>Se<sub>3</sub> upon Sn-doping suggesting improved p-type conductivity.

Finally, in the third study in this thesis a controllable fabrication approach for Sb<sub>2</sub>Se<sub>3</sub> thin film absorbers with significantly enhanced grain orientations combining RF-magnetron sputtering and post-thermal selenization in an inert gas at elevated pressures was developed. The film structure was studied by X-ray diffraction (XRD). Improved grain

orientations in the  $\text{Sb}_2\text{Se}_3$  thin film closely aligning with the  $c$ -axis, especially in the [002] direction without compromising the surface compactness was obtained with the isothermal selenization process at 380 °C and 300 Torr of Ar-pressure at RT. The selenization was performed in quartz ampoules together with the elemental Se beads.

In summary, this thesis presents a comprehensive investigation of the optoelectronic and structural properties of  $\text{Sb}_2\text{Se}_3$  absorber material for emerging photovoltaics. This study filled some knowledge gaps about the optoelectronic properties of  $\text{Sb}_2\text{Se}_3$  and provided valuable insights into strategies for overcoming current limitations and improving the efficiency of  $\text{Sb}_2\text{Se}_3$ -based solar cells.

## Lühikokkuvõte

### Päikeseplatari absorbermaterjali $Sb_2Se_3$ optoelektronsete omaduste muutmine

Kvaasi-ühemöötmeline materjal antimoniseleniid ( $Sb_2Se_3$ ) on viimasel ajal pälvinud laialdast tähelepanu, sest omab päikeseelemendi absorberina mitmeid eeliseid teiste kalkogeniidide ees.  $Sb_2Se_3$  on madala toksilisusega, päikeseenergia elektrienergiaks muundamise jaoks optimaalse keelutsooniga (toatemperatuuril  $\sim 1,2$  eV), kõrge valguse neeldumiskoeffitsendiga ( $> 10^4$  cm<sup>-1</sup>) ning pika vähemus laengukandjate eluaga ( $\sim 60$  ns). Lisaks on  $Sb_2Se_3$ -l madal sulamistemperatuur (885 K), mis võimaldab materjali valmistamist madalatel temperatuuridel, andes sellega võimaluse vähendada õhukeseleiliste päikeseelementide tootmiskulusid.  $Sb_2Se_3$  kristallilisus ning optoelektronsed omadused sõltuvad tugevalt materjali sünteesimise tingimustest sh alusmaterjali tüübist, sünteesi või sadestamise temperatuurist, järeltöötlemise temperatuurist ning keemilisest keskkonnast. Need parameetrid mõjutavad ka päikeseelementide efektiivsust, mis  $Sb_2Se_3$  puhul ulatub hetkel 11%-ni. Vaatamata efektiivsuse kiirele kasvule viimasel kümnendil, on  $Sb_2Se_3$ -põhiste päikeseelementide arendamisel endiselt kolm peamist väljakutset: keeruline defektide keemia, madal laengukandjate tihedus ning anisotroopsed elektrilised omadused, mis sõltuvad kristallide orientatsioonist.

Doktoritöö põhineb kolmel eelretsenseeritud teadusartiklil, mille keskmes on ülaltoodud väljakutsed. Täpsemalt uuriti legeerimise ning tahkete lahuste moodustamise strateegiaid ning töötati välja uudne lähenemisviis kõrge kristallilise kvaliteediga  $Sb_2Se_3$  õhukete kilede valmistamiseks. Esimeses uuringus sünteesiti kõrge puhtusastmega lähteainetest antimon selenosulfiid  $Sb_2(Se_{1-x}S_x)_3$  ( $x = 0-1$ ) polükristalsed tahked lahused eesmärgiga muuta väavli lisamisega  $Sb_2Se_3$  optoelektronsed omadusi.  $Sb_2(Se_{1-x}S_x)_3$  tahkete lahuste optilisi omadusi uuriti esmakordselt fotoluminestsents spektroskoopia abil kasutades erinevaid temperatuure ja ergastuskiirguse võimsusi. Leiti, et madalatemperatuurne fotoluminestsentskiirguse riba nihkus väavli kontsentratsiooni kasvades 1,309 eV-lt 1,728 eV-ni, olles kooskõlas materjali keelutsooni laiuse kasvuga. Madala väavli sisaldusega ( $x \leq 0,2$ ) objektides mõõdeti eksitonidest pärinev luminescentskiirgus ning suurema väavli sisaldusega ( $x = 0,4$  kuni  $x = 1$ ) tahketes lahustes sügavate doonorite ja sügavate aktseptorite paaride rekombinatsioonist pärinev kiirgus. Luminescentskiirguse ribade ebasümmeetriline kuju on tingitud elektron-foonon vastasmõjust, mis leiti olevat tugevam suurema väavli sisaldusega  $Sb_2(Se_{1-x}S_x)_3$  tahketes lahustes, kus on suuremad energiaga optilised foononid.

Doktoritöö teises osas legeeriti polükristalset  $Sb_2Se_3$  tinaga (Sn), eesmärgiga parandada absorbermaterjali p-tüüpi juhtivust. Tinaga legeerimine viidi läbi vakumeeritud kvartsist ampullides 30 minuti jooksul kasutades  $Sb_2Se_3$  isotermilist järeldõõmutamist erinevatel temperatuuridel (350 °C, 400 °C, 450 °C, 500 °C) koos  $SnSe_2$ -ga. Sn sisaldus materjalides tehti kindlaks röntgenfotoelektron-spektroskoopia abil. Muutuseid  $Sb_2Se_3$  elektronstruktuuris uuriti ultravioletse fotoelektron-spektroskoopiaga. Leiti, et Sn-ga legeerimine vähendas  $Sb_2Se_3$  väljumistööd ning nihutas Fermi nivood valentstsooni laele lähemale, mis viitab materjali p-tüüpi juhtivuse suurenemisele.

Doktoritöö viimasel osas töötati välja soovitud kristallide orientatsiooniga  $Sb_2Se_3$  õhukete kilede valmistamise meetod, kombineerides raadiosagedusliku magnetron pihustamise meetodi seleniseerimisega intergaasi keskkonnas. Röntgendifraktsiooni

analüüsi põhjal saadi antud meetodil  $\text{Sb}_2\text{Se}_3$  õhukesed kiled kristallide orientatsiooniga [002] suunas, säilitades samal ajal kilede kompaktsuse. Parim tulemus saadi  $\text{Sb}_2\text{Se}_3$  kilede isotermaalisel seleniseerimisel 380 °C ja 300 Torri toatemperatuurse argooni rõhu juures. Seleniseerimine teostati kvartsist ampullides kasutades seleeni allikana Se terasid.

Kokkuvõttes, käesolevas doktoritöös uuriti põhjalikult perspektiivse päikesepatarei absorbermaterjali  $\text{Sb}_2\text{Se}_3$  optoelektronseid ja struktuurseid omadusi, täites mõned teadmiste lüngad ning andes väärtuslikku teavet praeguste piirangute ületamise ja  $\text{Sb}_2\text{Se}_3$ -põhiste päikesepatareide tõhususe parandamise strateegiate kohta.



# Appendix 1

## Publication I

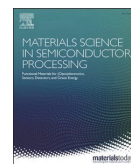
M. E. Uslu, R. Kondrotas, R. Nedzinskas, O. Volobujeva, K. Timmo, M. Kauk-Kuusik, J. Krustok, M. Grossberg, „Study of the optical properties of  $\text{Sb}_2(\text{Se}_{1-x}\text{S}_x)_3$  ( $x = 0-1$ ) solid solutions”, Material Science in Semiconductor Processing 144 (2022) 106571, <https://doi.org/10.1016/j.mssp.2022.106571>





Contents lists available at ScienceDirect

## Materials Science in Semiconductor Processing

journal homepage: [www.elsevier.com/locate/mssp](http://www.elsevier.com/locate/mssp)Study of the optical properties of  $\text{Sb}_2(\text{Se}_{1-x}\text{S}_x)_3$  ( $x = 0-1$ ) solid solutionsMehmet Ender Uslu<sup>a,\*</sup>, Rokas Kondrotas<sup>b</sup>, Ramūnas Nedzinskas<sup>b</sup>, Olga Volobujeva<sup>a</sup>,  
Kristi Timmo<sup>a</sup>, Marit Kauk-Kuusik<sup>a</sup>, Jüri Krustok<sup>a</sup>, Maarja Grossberg<sup>a</sup><sup>a</sup> Department of Materials and Environmental Technology, Tallinn University of Technology, Ehitajate tee 5, 19086, Tallinn, Estonia<sup>b</sup> State Research Institute Center for Physical Sciences and Technology, Saulėtekio Ave. LT-10257, Vilnius, Lithuania

## ARTICLE INFO

## Keywords:

 $\text{Sb}_2(\text{Se}_{1-x}\text{S}_x)_3$ 

Photoluminescence

Excitons

Deep donor-deep acceptor pairs

Electron phonon interaction

## ABSTRACT

This study presents a detailed analysis of the optical properties of the  $\text{Sb}_2(\text{Se}_{1-x}\text{S}_x)_3$  ( $x = 0-1$ ) polycrystals. Four antimony selenosulfide solid solutions  $\text{Sb}_2(\text{Se}_{1-x}\text{S}_x)_3$  together with  $\text{Sb}_2\text{Se}_3$  and  $\text{Sb}_2\text{S}_3$  were synthesized from elemental precursors at the same synthesis conditions, only varying the  $x = \text{S}/(\text{Se} + \text{S})$  value with a step of  $\Delta x = 0.2$ . Successful formation of the  $\text{Sb}_2(\text{Se}_{1-x}\text{S}_x)_3$  solid solutions was determined by Raman spectroscopy and X-ray diffraction. As expected for the same type of crystal structure of  $\text{Sb}_2\text{Se}_3$  and  $\text{Sb}_2\text{S}_3$ , the bimodal behavior of  $\text{A}_g$  Raman mode in  $\text{Sb}_2(\text{Se}_{1-x}\text{S}_x)_3$  was detected. Temperature and excitation power dependent photoluminescence (PL) analysis of  $\text{Sb}_2(\text{Se}_{1-x}\text{S}_x)_3$  was performed in order to look into the electronic and defect structure of these promising semiconductor materials for optoelectronic applications. The shift of the near band edge PL emission in  $\text{Sb}_2(\text{Se}_{1-x}\text{S}_x)_3$  towards higher energies from 1.309 eV to 1.728 eV with increasing sulfur content was detected at  $T = 3 \text{ K}$ . A change in the radiative recombination mechanism was detected being of excitonic origin in samples with  $x \leq 0.2$  and resulting from deep donor-deep acceptor pair recombination in samples with  $x > 0.2$ .

## 1. Introduction

Antimony chalcogenides ( $\text{Sb}_2\text{Ch}_3$ ), where Ch refers to S, Se, or Te, find widespread practices in photocatalysis, supercapacitors, and photovoltaics, as exhibiting thermoelectric [1,2], photoelectric, and dielectric [3] features. One of the most promising chalcogenides for photoelectric applications is the antimony selenide that was first introduced in the 1950s [4]. Antimony selenide ( $\text{Sb}_2\text{Se}_3$ ) is a binary compound from the  $\text{V}_2\text{-VI}_3$  group with anisotropic optoelectronic properties. It gained research attention in the last decade as an absorber material in thin-film solar cells due to an optimal band gap energy of 1.2 eV at room temperature [5], a high absorption coefficient of  $10^4 \text{ cm}^{-1}$  at visible wavelengths [6], and due to being a relatively cheap material composed of earth abundant elements with low toxicity.

However,  $\text{Sb}_2\text{Se}_3$  has a quasi-1D ribbons-like crystal structure, which results in 3 and 2 non-equivalent lattice sites for Se and Sb, respectively. Such low symmetry configuration of atoms in the lattice leads to large variety of point defects and complicated defect chemistry overall [7–9]. Complex defects with unknown nature may act as recombination centers, which drastically degrade the photoelectric conversion efficiency of the respective devices. Although the thermal activation of free electrons or holes benefits from specific intrinsic defects, not every kind of defect

has an off-stoichiometric doping character. A recent computational study using the hybrid method in Density Functional Theory (DFT) suggests that in  $\text{Sb}_2\text{Se}_3$  there are low formation energy cation–anion antisite defects with mid-gap transition levels that could act as recombination centers [10]. Briefly, these deep defects can be the main drawback against the advancement of  $\text{Sb}_2\text{Se}_3$  based thin-film solar cells. The maximum power conversion efficiency of antimony selenide-based solar cells so far is 9.2% [11], resulting from enhanced current density due to improved alignment of the crystals in [221] and [211] directions enabling more efficient charge-carriers transport. The grain boundaries between the ribbons stacked together by Van der Waals forces act as obstructive spaces degrading charge-carriers transport in [hk0] directions [12]. In other words, the anisotropic crystal structure is the second limiting factor for the energy conversion efficiency of the  $\text{Sb}_2\text{Se}_3$  photoabsorber.

The most accepted consensus in the literature about  $\text{Sb}_2\text{Se}_3$  based thin-film solar cells is that a Se-rich composition, where Se replaces some Sb-sites ( $\text{Se}_{\text{Sb}}$ ), enhances *p*-type conductivity, and increases the power conversion efficiency [13]. However, the post-growth selenization process, which is usually used to obtain a Se-rich  $\text{Sb}_2\text{Se}_3$ , has been shown to result only in a slight increment of Se-content since antimony selenide has a single-phase structure with no stable secondary phase.

\* Corresponding author.

E-mail address: [mehmet.uslu@taltech.ee](mailto:mehmet.uslu@taltech.ee) (M.E. Uslu).<https://doi.org/10.1016/j.mssp.2022.106571>

Received 22 December 2021; Received in revised form 27 January 2022; Accepted 12 February 2022

Available online 16 February 2022

1369-8001/© 2022 Elsevier Ltd. All rights reserved.

The need for the post-growth selenization can also be due to the volatility of selenium in high-temperature processes during the deposition of  $\text{Sb}_2\text{Se}_3$  by methods like rapid thermal evaporation (RTE) [14], close spaced sublimation (CSS) [15], and vapor transfer deposition (VTD). Nevertheless, experiments, which were performed to reveal the dominant defects in  $\text{Sb}_2\text{Se}_3$ , synthesized by different methods, show different results depending on the crystal quality, and slight deviations from stoichiometry. A deep-level transient spectroscopy (DLTS) study of a  $\text{Sb}_2\text{Se}_3$  based thin-film solar cell confirmed the existence of the deep defects with the nature of hole traps at around 0.48 eV and 0.71 eV above the valence band maximum (VBM), respectively, assigned to  $V_{\text{Sb}}$  and  $\text{Se}_{\text{Sb}}$  [16]. On the other hand, the low-temperature ( $T = 10$  K) photoluminescence (PL) spectra of  $\text{Sb}_2\text{Se}_3$  polycrystals showed three bands at 0.94, 1.10, and 1.24 eV [17]. The authors confirmed the emission at 0.94 eV as evidence of the close donor-acceptor pair (DAP) recombination, while the one at 1.24 eV resulting from distant donor-acceptor pair recombination. In addition to this, temperature and laser power-dependent PL study of  $\text{Sb}_2\text{Se}_3$  microcrystals using pulsed UV laser reported near band-edge excitons and biexcitons [18]. In  $\text{Sb}_2\text{S}_3$  the band-to-band PL emission was detected at 1.65 eV at room temperature and its intensity was found to change noticeably depending on the deposition method [19].

The optical processes in  $\text{Sb}_2\text{Se}_3$  are also affected by the closely positioned direct and indirect band-gaps [6]. Apart from this, also the valence band splitting by a crystal field ( $\Delta_{\text{cr}} = 13$  meV) and the spin-orbit interaction ( $\Delta_{\text{so}} = 35$  meV) at the Brillouin zone center has been detected [20]. It is crucial to collect more information about the electronic band structure of such highly anisotropic semiconductor material. Moreover,  $\text{Sb}_2\text{Se}_3$  is isomorphous to antimony sulfide ( $\text{Sb}_2\text{S}_3$ ) as both are from  $Pnma(62)$  space group [21], so we can follow a strategy of varying the  $x = \text{S}/(\text{S} + \text{Se})$  value in  $\text{Sb}_2(\text{Se}_{1-x}\text{S}_x)_3$  solid solutions to learn more about the electronic structure of this promising group of materials. Varying the  $x$ -value enables to tune the bandgap of  $\text{Sb}_2(\text{Se}_{1-x}\text{S}_x)_3$  in the range from 1.2 eV to 1.7 eV broadening the field of applications of these materials [22]. Moreover,  $\text{Sb}_2(\text{Se}_{1-x}\text{S}_x)_3$  (with determined Se content of 29 at%) based thin film solar cells have demonstrated power conversion efficiencies above  $\sim 10\%$  [23]. The optical properties of the  $\text{Sb}_2(\text{Se}_{1-x}\text{S}_x)_3$  solid solutions are barely studied and there is no photoluminescence data available for this material series. Therefore, this study aims at detailed insight into the electronic and defect structure of  $\text{Sb}_2(\text{Se}_{1-x}\text{S}_x)_3$  solid solutions ( $x$  varying from 0 to 1 and with  $\Delta x = 0.2$ ) using excitation power density and temperature dependent PL measurements to improve the understanding of the fundamental properties of these promising absorber materials for photovoltaics.

## 2. Experimental

$\text{Sb}_2(\text{Se}_{1-x}\text{S}_x)_3$  solid solutions with  $x = 0, 0.2, 0.4, 0.6, 0.8$  and 1 were synthesized from 5 N purity Sb, Se and S (Alfa Aesar) elemental precursors at the same synthesis conditions. The precursors were weighed in desired amounts and ratios, mixed and ground in an agate mortar, loaded into quartz ampoules, degassed and sealed under dynamic vacuum. For the synthesis, a two-step isothermal annealing process in a chamber furnace was used. All six samples together were heated up from room temperature to 200 °C within 1 h. After one week at 200 °C, the temperature was increased from 200 °C to 500 °C within 1 h. The samples were kept at 500 °C for one week. After two weeks, the synthesis-growth processes were stopped by taking the ampoules out of the furnace and cool down naturally in air to room temperature.

The elemental composition of the synthesized polycrystals were determined by Energy Dispersive X-ray Spectroscopy (EDX) using a Bruker Esprit 1.8 system on Zeiss Merlin high-resolution Scanning Electron Microscope (SEM). The phase composition and the evolution of the solid solution formation with varying S/Se ratio in  $\text{Sb}_2(\text{Se}_{1-x}\text{S}_x)_3$  was studied by using room-temperature micro-Raman analysis with Horiba's

LabRam HR800 spectrometer with a 532 nm laser line and with the spot size of 5  $\mu\text{m}$  in diameter. The Raman analysis was complemented by the powder X-Ray Diffraction (XRD) analysis using Rigaku Ultima IV diffractometer operating with the silicon strip detector D/teX Ultra. PDXL 2 software was used for the derivation of crystal structure information from the powder XRD data (ICDD 01-083-7430 and 03-065-2434 for  $\text{Sb}_2\text{Se}_3$  and  $\text{Sb}_2\text{S}_3$ , respectively).

For the PL measurements the polycrystals were mounted on the cold finger of a closed-cycle helium cryostat Janis SHI-4 of Lake Shore Cryotronics and the measurements were carried out in the temperature region of 3–110 K. Near band edge PL spectra were excited with a diode-pumped Nd:YAG solid state laser with the wavelength of 266 nm, pulse width 0.6 ns, and repetition rate 19 kHz. The maximum peak energy was 0.75  $\mu\text{J}$  and the maximum average power was approximately 15 mW. The maximum peak power density was estimated to be 660  $\text{kW cm}^{-2}$ . The laser beam was not focused to avoid damaging the sample and the pump power was reduced by a gradient UV (fused silica) filter. The PL signal was dispersed using a 0.5 m focal length Andor SR-500i monochromator and captured with thermoelectrically cooled InGaAs detector IGA-030-TE2-H of Electro-Optical Systems Inc and with Hamamatsu R632 photomultiplier tube in the case of  $\text{Sb}_2\text{S}_3$ .

For comparison, the PL spectra of deeper bands in the  $\text{Sb}_2(\text{Se}_{1-x}\text{S}_x)_3$  polycrystals were also measured by using a continuous wave He–Cd gas laser (Kimmon) with a wavelength of 442 nm and maximum power of 37.1 mW. For the respective measurements, the samples were mounted on the cold finger of a closed-cycle helium cryostat (Janis CCS-150) and cooled down to 20 K. For PL signal detection, a Hamamatsu InGaAs photomultiplier tube was used in the range of 0.77–1.35 eV.

## 3. Results and discussion

Average values of multiple spots from each polycrystalline solid solution measured by the EDX microanalysis are shown in Table 1. The results confirm the aimed elemental compositions of  $\text{Sb}_2(\text{Se}_{1-x}\text{S}_x)_3$  ( $x$  varying from 0 to 1 and with  $\Delta x \sim 0.2$ ). Evolution of the Raman spectra and XRD patterns with  $x$ -value in  $\text{Sb}_2(\text{Se}_{1-x}\text{S}_x)_3$  are presented in Figs. 1 and 2. The experimental Raman spectra were fitted with the Lorentzian functions. The Raman spectra of the pure  $\text{Sb}_2\text{Se}_3$  and  $\text{Sb}_2\text{S}_3$  compounds are in a very good correlation to the literature data with dominating  $A_g^2$  mode at 190  $\text{cm}^{-1}$  accompanied with other modes at 100, 125, 156, 213

**Table 1**  
Elemental compositions of the studied  $\text{Sb}_2(\text{Se}_{1-x}\text{S}_x)_3$  solid solutions determined by EDX.

$\text{Sb}_2(\text{Se}_{1-x}\text{S}_x)_3$	$x = \frac{\text{S}}{\text{S} + \text{Se}}$ input	$x = \frac{\text{S}}{\text{S} + \text{Se}}$ outcome	Antimony (Sb)	Selenium (Se)	Sulfur (S)
$\text{Sb}_2\text{Se}_3$	$x = 0$	$x = 0$	40.1 at% $\pm 1.4$ at%	59.8 at% $\pm 1.4$ at%	–
$\text{Sb}_2(\text{Se}_{0.8}\text{S}_{0.2})_3$	$x = 0.2$	$x = 0.21$	40.2 at% $\pm 1.5$ at%	46.8 at% $\pm 1.2$ at%	12.9 at% $\pm 0.2$ at%
$\text{Sb}_2(\text{Se}_{0.6}\text{S}_{0.4})_3$	$x = 0.4$	$x = 0.38$	39.9 at% $\pm 1.6$ at%	36.8 at% $\pm 1.0$ at%	23.2 at% $\pm 0.3$ at%
$\text{Sb}_2(\text{Se}_{0.4}\text{S}_{0.6})_3$	$x = 0.6$	$x = 0.60$	40.1 at% $\pm 1.7$ at%	23.8 at% $\pm 0.7$ at%	35.9 at% $\pm 0.5$ at%
$\text{Sb}_2(\text{Se}_{0.2}\text{S}_{0.8})_3$	$x = 0.8$	$x = 0.81$	40.1 at% $\pm 1.8$ at%	10.8 at% $\pm 0.3$ at%	49 at% $\pm 0.7$ at%
$\text{Sb}_2\text{S}_3$	$x = 1$	$x = 1$	40.2 at% $\pm 1.9$ at%	–	59.8 at% $\pm 0.9$ at%

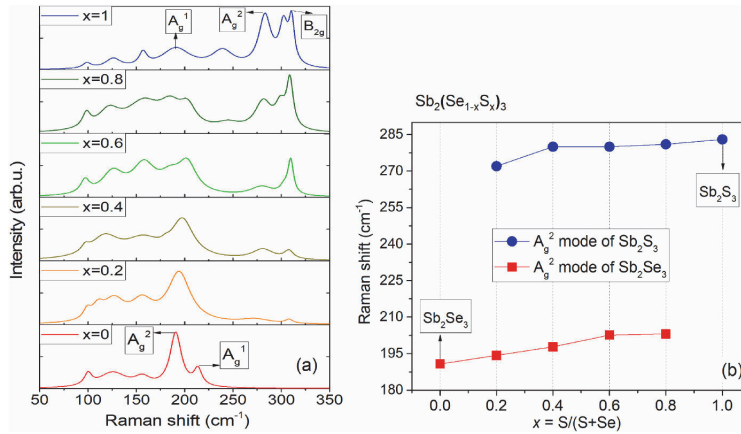


Fig. 1. a) Raman spectra of  $Sb_2(Se_{1-x}S_x)_3$  solid solutions, b) bimodal behavior of the  $A_g^2$  Raman modes regarding the  $x$ -value.

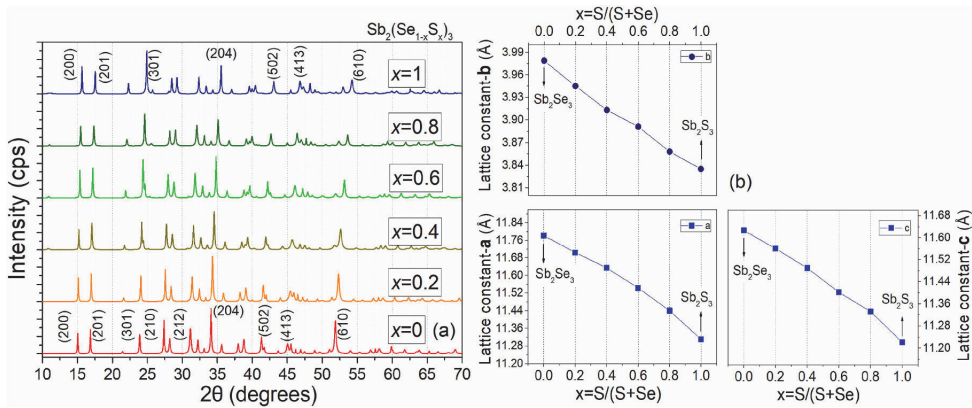


Fig. 2. a) XRD patterns of  $Sb_2(Se_{1-x}S_x)_3$  solid solutions, as the  $x$  changes from 0 to 1, b) the change in lattice constants for solid solutions depending on the  $x$ -value.

$cm^{-1}$  in  $Sb_2Se_3$  [24], and at  $A_g^2$  mode of  $Sb_2S_3$  at  $283\text{ cm}^{-1}$  accompanied with the other modes at  $98, 125, 156, 190, 239, 310\text{ cm}^{-1}$  [25,26]. The bimodal behavior of  $A_g^2$  modes confirms the formation of the  $Sb_2(Se_{1-x}S_x)_3$  solid solutions (see Fig. 1 a and b) although two Raman studies of  $Sb_2S_3$ , under different polarization, pressure and temperature

conditions, report different position of an  $A_g$  mode at  $312\text{ cm}^{-1}$  [25] and  $B_{2g}$  mode at  $314\text{ cm}^{-1}$  [26]. The behavior of FWHM on  $x$  value for two main peaks is given in Fig. S1. The XRD patterns of the solid solutions in Fig. 2a with  $x$  changing from 0 to 1, show that all the peaks belong to  $Sb_2Se_3$  and  $Sb_2S_3$ , respectively, and to their solid solutions. All of the

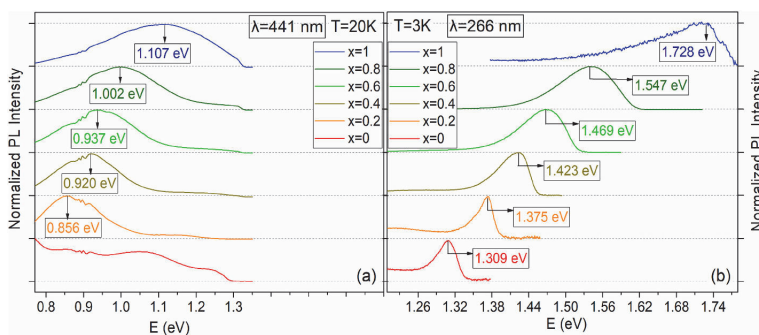


Fig. 3. a) PL spectra of the  $Sb_2(Se_{1-x}S_x)_3$  solid solutions with  $x$  varying from 0 to 1, respectively, excited by continuous wave laser (441 nm) at  $T = 20\text{ K}$ . b) PL spectra of the same materials excited by the pulsed UV laser (266 nm) at  $T = 3\text{ K}$  and laser power of  $15\text{ mW}$ .

solid solutions were determined to have an orthorhombic structure with space group *Pnma*. A shift of the XRD peaks towards higher degrees with increasing *x*-value was detected. The lattice parameters for each solid solution were extracted using Rietveld refinement procedure and the corresponding values regarding the *x*-value are shown in Fig. 2b. An example of the Rietveld refinement for one sample is given in Table S1 and Table S2. Decrease in the lattice parameters with increasing *x* value is detected as expected due to the smaller size of S atoms.

In order to study the electronic and defect structure of the  $\text{Sb}_2(\text{Se}_{1-x}\text{S}_x)_3$  solid solutions, temperature and laser power dependent photoluminescence measurements were performed and analyzed. The low-temperature ( $T = 3$  K) near band edge PL spectra measured with pulsed UV laser are presented in Fig. 3b, from where an asymmetric shape of the PL bands and a shift of the PL emission towards higher energies from 1.309 eV to 1.728 eV with increasing sulfur content is detected. All the detected PL spectra were dominated by an asymmetric PL band, which was fitted with Split-PseudoVoigt function. Fig. 3a presents the PL bands excited with the continuous wave laser at  $T = 20$  K, where the dominating PL band position  $E_{max}$  shows a blueshift from 0.856 eV to 1.107 eV with *x* varying from 0.2 to 1. The dominating PL band of  $\text{Sb}_2\text{Se}_3$  is out of the measurement range ( $<0.8$  eV). These very broad (FWHM  $\sim 0.25$  eV) and Gaussian shaped deep PL bands have rather low intensity making the reliable detailed temperature and laser power dependent analysis impossible. Since the dependence of the low-temperature PL spectra of the  $\text{Sb}_2(\text{Se}_{1-x}\text{S}_x)_3$  solid solutions on the *x*-value is not available in the literature, it is presented in the current paper. From here we focus on the analysis of the edge PL emission of  $\text{Sb}_2(\text{Se}_{1-x}\text{S}_x)_3$  excited with the pulsed UV laser (see Fig. 3b).

Temperature dependencies of the edge PL band positions  $E_{max}$  of the  $\text{Sb}_2(\text{Se}_{1-x}\text{S}_x)_3$  solid solutions are shown in Fig. 4. Redshift of the PL band position with increasing temperature, which is more rapid than the temperature dependence of the bandgap energy [27], was detected for  $\text{Sb}_2(\text{Se}_{1-x}\text{S}_x)_3$  with  $x = 0$  and  $x = 0.2$ . Similar rapid redshift was detected in Ref. [18] and was attributed mostly to biexcitons. For the other samples, the redshift could not be observed within the used temperature range, as the PL emission quenched fast and disappeared for  $T > 60$  K. The dependence of the integrated PL intensity  $\Phi(P)$  as a function of laser power  $P$  in the range from 0.1 mW to 15 mW for the  $\text{Sb}_2(\text{Se}_{1-x}\text{S}_x)_3$  solid solutions with *x* varying from 0 to 1 is shown in Fig. 5a and is following the dependence  $\Phi \sim P^m$  [28]. The power coefficient values  $m = 1.37$  and  $m = 1.03$  were found for  $\text{Sb}_2(\text{Se}_{1-x}\text{S}_x)_3$  with  $x = 0$  and  $x = 0.2$ , respectively, indicating to the exciton related recombination processes, which are known to have  $m \geq 1$ . Excitons and biexcitons have been recently detected in high quality  $\text{Sb}_2\text{Se}_3$  microcrystals under high PL excitation density [18]. However,  $m < 1$  was found for the rest of the  $\text{Sb}_2(\text{Se}_{1-x}\text{S}_x)_3$  solid solutions with  $x = 0.4$  to  $x = 1$ , indicating to a different type of radiative recombination in the respective samples involving charge carriers localized at defects within the band gap. Interestingly, no shift of the PL band position  $E_{max}$  with laser power could be detected for all

studied  $\text{Sb}_2(\text{Se}_{1-x}\text{S}_x)_3$  solid solutions.

Looking at the shape of the PL bands, such asymmetric shape at low temperatures can result from an electron-phonon coupling, where phonon replicas follow a Poisson distribution as described by the well-known Frank-Condon configuration coordinate model [29]. This applies for the samples with  $x > 0.2$  as in the case of  $x \leq 0.2$ , the laser power dependence of the PL emission indicated excitonic origin as described above. The asymmetric shape is also characteristic to heavily doped semiconductors, which in this case can be excluded as no characteristic strong blueshift (usually  $>10$  meV/decade) of the PL bands with increasing laser power could be detected [30]. Moreover, theoretical DFT calculations predict high concentration of rather deep donor and acceptor defects in  $\text{Sb}_2\text{Se}_3$ , which easily form deep donor-deep acceptor pairs (DD-DA) [10]. DD-DA pair recombination involving a donor and an acceptor, which are located at very short distance in the crystal lattice includes strong Coulomb interaction between the corresponding defects and can result in close to band edge emission with PL peak energy [31]:

$$E_{DAP} = E_g - (E_A + E_D) + \frac{e^2}{4\pi\epsilon\epsilon_0 r} \quad 1$$

where  $E_g$  is the bandgap energy,  $E_D$  and  $E_A$  are respectively donor and acceptor ionization energies,  $\epsilon_0$  is vacuum permittivity,  $\epsilon$  is the relative dielectric constant, and  $r$  is the distance between donor and acceptor defect in the crystal lattice. When paired, the ionization energies of the related donor and acceptor defects in the case of closest pairs are rather small. Usually DAP emission is characterized with a small blueshift with increasing laser power (in the order of few meV). However, in the case of very close donor-acceptor pairs, there can be almost no blueshift as is observed also in this study for the  $\text{Sb}_2(\text{Se}_{1-x}\text{S}_x)_3$  solid solutions [32].

According to the Frank-Condon configuration coordinate model, the full PL spectrum related to recombination centre consists of zero phonon line and its phonon replicas, which are separated by the phonon energy  $E_{ph}$ . The intensity of each phonon replica is proportional to  $I(k) \sim \exp(-S)S^k/k!$  [29] with  $k$  from 0 to  $\infty$  (see Fig. 6). In quite high quality crystals, the spectral shape of zero phonon line and its phonon replicas is Gaussian with halfwidth  $w$ .  $E_{ph}$  is usually the longitudinal optical (LO) phonon energy. However, in polycrystalline and anisotropic  $\text{Sb}_2(\text{Se}_{1-x}\text{S}_x)_3$  solid solutions the spectral shape of these components can be different. Inhomogeneous broadening of zero phonon line can increase the halfwidth of all peaks and the shape can become asymmetric. Therefore, it is difficult to resolve all individual peaks in our spectra and we just see a total asymmetric band.

The strength of the electron-phonon interaction and therefore the distribution of the phonon replicas is described by the  $S$  parameter, which is called a Huang-Rhys factor. In this study, a rather small values, namely  $S \sim 0.8$  were determined for the studied  $\text{Sb}_2(\text{Se}_{1-x}\text{S}_x)_3$  solid solutions. The difference ( $W_L - W_H$ ) between half-width of the low energy side ( $W_L$ ) and half-width of the high energy side ( $W_H$ ) of the PL band was

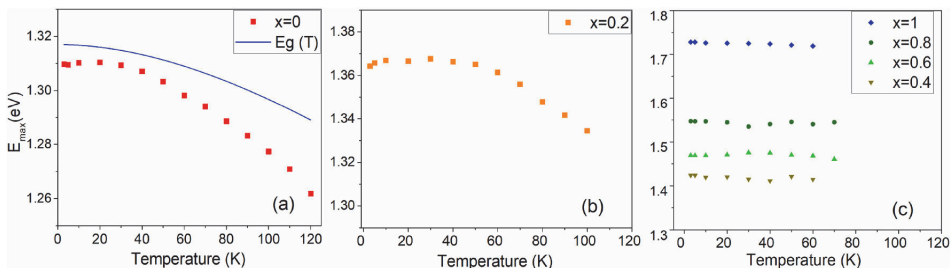


Fig. 4. Temperature dependencies of the PL band positions of the  $\text{Sb}_2(\text{Se}_{1-x}\text{S}_x)_3$  solid solutions.  $E_g(T)$  is temperature dependence of the bandgap energy of  $\text{Sb}_2\text{Se}_3$  measured by photoreflectance [27]: a) redshift of  $E_{max}$  for  $x = 0$ , b) redshift of  $E_{max}$  for  $x = 0.2$ , c) from  $x = 0.4$  to 1, no clear shift of the peaks could be detected within this temperature range.

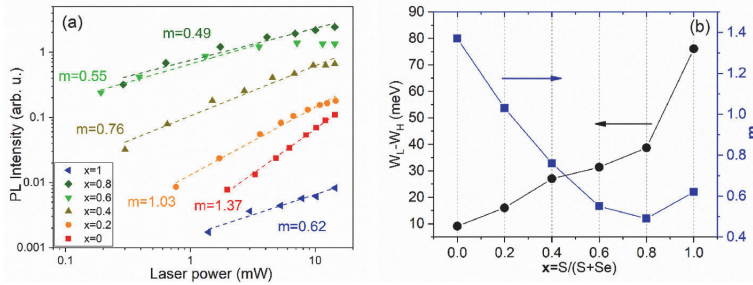


Fig. 5. a) The integrated intensities of near band edge PL bands as a function of laser power at T = 3 K on a log-log scale for the  $Sb_2(Se_{1-x}S_x)_3$  solid solutions. b) The opposite trends of  $(W_l - W_H)$  and m value on the x-value of  $Sb_2(Se_{1-x}S_x)_3$  at T = 3 K.

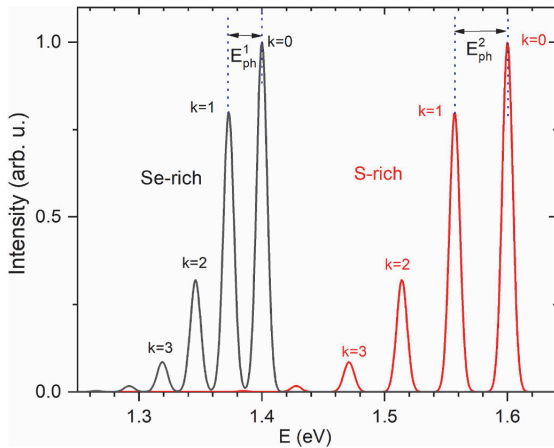


Fig. 6. Theoretical shape of PL bands with different phonon energies and S = 0.8. Gaussian shape with  $w = 10$  meV was used in calculations. The zero phonon line position was taken 1.4 and 1.6 eV for Se-rich and S-rich  $Sb_2(Se_{1-x}S_x)_3$  cases, respectively. The asymmetry of resulting PL band is increasing with increase of  $E_{ph}$ .

found to grow linearly with increasing sulfur content (see Fig. 5b).

The increased asymmetry of the PL band with increasing x value is more or less related to the increase of phonon energy  $E_{ph}$ , see Figs. 1a and Figure 6. The position of the PL band follows a linear trend towards higher energies with increasing x value in  $Sb_2(Se_{1-x}S_x)_3$ , with an exception of x = 1 ( $Sb_2S_3$ ), which shows a PL band at higher energies than the linear trend predicts. Considering also the low PL intensity of the  $Sb_2S_3$  sample, we can propose that this sample has lower crystalline quality and may contain amorphous  $Sb_2S_3$  phase, which has higher band gap (>1.8 eV [33]) compared to crystalline  $Sb_2S_3$ . The amorphous phase could result from non-optimized growth conditions for  $Sb_2S_3$  as in this study the growth conditions were kept constant for the whole series of  $Sb_2(Se_{1-x}S_x)_3$  solid solutions.

Finally, the temperature dependencies of the integrated intensities of the PL emissions of the  $Sb_2(Se_{1-x}S_x)_3$  solid solutions with  $x \leq 0.2$  enabled to determine the thermal activation energies for the corresponding PL bands by fitting the experimental data with the theoretical expression [34]:

$$\Phi(T) = \frac{\Phi_0}{1 + \alpha_1 \cdot T^{3/2} + \alpha_2 \cdot T^{3/2} \cdot \exp(-\frac{E_a}{kT})} \quad 2$$

where  $\alpha_1$  and  $\alpha_2$  are the process rate parameters and  $E_a$  is the thermal activation energy. Thermal activation energies  $E_a = 15 \pm 3$  meV and  $E_a$

$= 11 \pm 3$  meV for the samples with  $x = 0$  and  $x = 0.2$ , respectively, were obtained. These  $E_a$  values correlate nicely with the thermal quenching activation energies found in a recent study for the excitons and biexcitons [18], confirming that the PL emission in the  $Sb_2(Se_{1-x}S_x)_3$  solid solutions with  $x \leq 0.2$  is of excitonic origin. Unfortunately, there were not enough experimental data points to determine the PL quenching of the solid solutions from  $x = 0.4$  to 1.

#### 4. Conclusion

In this study, the polycrystals of  $Sb_2(Se_{1-x}S_x)_3$  solid solutions were successfully synthesized and the structural and luminescent properties of these materials were studied. The XRD and Raman analysis confirmed the formation of the full range of solid solutions. The low-temperature (T = 3 K) PL emission of  $Sb_2(Se_{1-x}S_x)_3$  solid solutions excited with a pulsed UV laser was found to shift towards higher energies from 1.309 eV to 1.728 eV with increasing sulfur content. Laser power and temperature dependent PL study enabled to determine the origin of the PL emission in the respective samples as of excitonic origin in the samples with  $x = 0$  and 0.2 and resulting from the DD-DA pairs recombination in the samples with  $x = 0.4$  to 1. Consequently, a change in the radiative recombination mechanism was detected in the studied  $Sb_2(Se_{1-x}S_x)_3$  with varying S/Se ratio.

#### CRedit authorship contribution statement

**Mehmet Ender Uslu:** Conceptualization, Data curation, Formal analysis, Writing – original draft, Writing – review & editing. **Rokas Kondrotas:** Writing – review & editing, Conceptualization. **Ramūnas Nedzinskas:** Conceptualization, Data curation, Writing – review & editing. **Olga Volobujeva:** Writing – review & editing, Supervision, Data curation, Conceptualization. **Kristi Timmo:** Conceptualization, Data curation, Writing – review & editing. **Marit Kauk-Kuusik:** Writing – review & editing, Resources, Conceptualization. **Jüri Krustok:** Conceptualization, Data curation, Formal analysis, Writing – original draft, Writing – review & editing. **Maarja Grossberg:** Writing – review & editing, Writing – original draft, Supervision, Resources, Funding acquisition, Formal analysis, Data curation, Conceptualization.

#### Declaration of competing interest

The authors declare that they have no known competing financial interests or personal relationships that could have appeared to influence the work reported in this paper.

#### Acknowledgments

This work has been supported by the European Regional Development Fund, Project TK141, and by the Estonian Research Council project

PRG1023.

## Appendix A. Supplementary data

Supplementary data to this article can be found online at <https://doi.org/10.1016/j.mssp.2022.106571>.

## References

- [1] F. Yan, T.J. Zhu, X.B. Zhao, S.R. Dong, Microstructures and thermoelectric properties of GeSbTe based layered compounds, *Appl. Phys. A* 88 (2007) 425–428, <https://doi.org/10.1007/s00339-007-4006-9>.
- [2] Y. Zheng, Q. Zhang, X. Su, H. Xie, S. Shu, T. Chen, G. Tan, Y. Yan, X. Tang, C. Uher, G.J. Snyder, Mechanically robust BiSbTe alloys with superior thermoelectric performance: a case study of stable hierarchical nanostructured thermoelectric materials, *Adv. Energy Mater.* 5 (2015) 1401391, <https://doi.org/10.1002/aenm.201401391>.
- [3] A.M. Farid, H.E. Atyia, N.A. Hegab, AC conductivity and dielectric properties of Sb<sub>2</sub>Te<sub>3</sub> thin films, *Vacuum* 80 (2005) 284–294, <https://doi.org/10.1016/j.vacuum.2005.05.003>.
- [4] E. Dönges, Z. Anorg., Über Chalkogenohalogenide des dreiwertigen Antimons und Wismuts. II. Über Selenohalogenide des dreiwertigen Antimons und Wismuts und über Antimon(III)-selenid Mit 2 Abbildungen, *Allg. Chem.* 263 (1950) 280–291, <https://doi.org/10.1002/zaac.19502630508>.
- [5] X. Wang, R. Tang, C. Wu, C. Zhu, T. Chen, Development of antimony sulfide-selenide Sb<sub>2</sub>(S,Se)<sub>3</sub>-based solar cells, *J. Energy Chem.* 27 (2018) 713–721, <https://doi.org/10.1016/j.ijechem.2017.09.031>.
- [6] C. Chen, W. Li, Y. Zhou, C. Chen, M. Luo, X. Liu, K. Zeng, B. Yang, C. Zhang, J. Han, J. Tang, Optical properties of amorphous and polycrystalline Sb<sub>2</sub>Se<sub>3</sub> thin films prepared by thermal evaporation, *Appl. Phys. Lett.* 107 (2015), 043905, <https://doi.org/10.1063/1.4927741>.
- [7] V.L. Deringer, R.P. Stoffel, M. Wuttig, R. Dronskowski, Vibrational properties and bonding nature of Sb<sub>2</sub>Se<sub>3</sub> and their implications for chalcogenide materials, *Chem. Sci.* 6 (2015) 5255, <https://doi.org/10.1039/C5SC00825E>.
- [8] Y. Zhou, L. Wang, S. Chen, S. Qin, X. Liu, J. Chen, D.-J. Xue, M. Luo, Y. Cao, Y. Cheng, E.H. Sargent, J. Tang, Thin-film Sb<sub>2</sub>Se<sub>3</sub> photovoltaics with oriented one-dimensional ribbons and benign grain boundaries, *Nat. Photonics* 9 (2015) 409–415, <https://doi.org/10.1038/nphoton.2015.78>.
- [9] M. Huang, P. Xu, D. Han, J. Tang, S. Chen, Complicated and unconventional defect properties of the quasi-one-dimensional photovoltaic semiconductor Sb<sub>2</sub>Se<sub>3</sub>, *ACS Appl. Mater. Interfaces* 11 (17) (2019) 15564–15572, <https://doi.org/10.1021/acsami.9b01220>.
- [10] C.N. Savory, D.O. Scanlon, The complex defect chemistry of antimony selenide, *J. Mater. Chem.* 7 (2019) 10739–10744, <https://doi.org/10.1039/C9TA02022E>.
- [11] Z. Li, X. Liang, G. Li, H. Liu, H. Zhang, J. Guo, J. Chen, K. Shen, X. San, W. Yu, R.E. I. Schropp, Y. Mai, 9.2%-efficient core-shell structured antimony selenide nanorod array solar cells, *Nat. Commun.* 10 (2019), <https://doi.org/10.1038/s41467-018-07903-6>. Article number: 125.
- [12] C. Chen, D.C. Bobela, Y. Yang, S. Lu, K. Zeng, C. Ge, B. Yang, L. Gao, Y. Zhao, M. C. Beard, J. Tang, Characterization of basic physical properties of Sb<sub>2</sub>Se<sub>3</sub> and its relevance for photovoltaics, *Front. Optoelectron.* 10 (2017) 18–30, <https://doi.org/10.1007/s12200-017-0702-z>.
- [13] R. Tang, Z.-H. Zheng, Z.-H. Su, X.-J. Li, Y.-D. Wei, X.-H. Zhang, Y.-Q. Fu, J.-T. Luoa, P. Fan, G.-X. Liang, Highly efficient and stable planar heterojunction solar cell based on sputtered and post-selenized Sb<sub>2</sub>Se<sub>3</sub> thin film, *Nano Energy* 64 (2019) 103929, <https://doi.org/10.1016/j.nanoen.2019.103929>.
- [14] C. Yuan, L. Zhang, W. Liu, C. Zhu, Rapid thermal process to fabricate Sb<sub>2</sub>Se<sub>3</sub> thin film for solar cell application, *Sol. Energy* 137 (2016) 256–260, <https://doi.org/10.1016/j.solener.2016.08.020>.
- [15] L. Guo, B. Zhang, S. Ranjit, J. Wall, S. Saurav, A.J. Hauser, G. Xing, L. Li, X. Qian, F. Yan Interface, Engineering via sputtered oxygenated Cds:O window layer for highly efficient Sb<sub>2</sub>Se<sub>3</sub> thin-film solar cells with efficiency above 7, *Solar RRL* 3 (2019) 1900225, <https://doi.org/10.1002/solr.201900225>.
- [16] X. Wen, C. Chen, S. Lu, K. Li, R. Kondrotas, Y. Zhao, W. Chen, L. Gao, C. Wang, J. Zhang, G. Niu, J. Tang, Vapor transport deposition of antimony selenide thin film solar cells with 7.6% efficiency, *Nat. Commun.* 9 (2018) 2179, <https://doi.org/10.1038/s41467-018-04634-6>.
- [17] M. Grossberg, O. Volobujeva, A. Penezko, R. Kaupmees, T. Raadik, J. Krustok, Origin of photoluminescence from antimony selenide, *J. Alloys Compd.* 817 (2020) 152716, <https://doi.org/10.1016/j.jallcom.2019.152716>.
- [18] J. Krustok, R. Kondrotas, R. Nedzinskas, K. Timmo, R. Kaupmees, V. Mikli, M. Grossberg, Identification of excitons and biexcitons in Sb<sub>2</sub>Se<sub>3</sub> under high photoluminescence excitation density, *Adv. Opt. Mater.* 9 (2021) 2100107, <https://doi.org/10.1002/adom.202100107>.
- [19] Y. Zeng, K. Sun, J. Huang, M.P. Nielsen, F. Ji, C. Sha, S. Yuan, X. Zhang, C. Yan, X. Liu, H. Deng, Y. Lai, J. Seidel, N. Ekins-Daukes, F. Liu, H. Song, M. Green, X. Hao, Quasi-vertically-orientated antimony sulfide inorganic thin-film solar cells achieved by vapor transport deposition, *ACS Appl. Mater. Interfaces* 12 (20) (2020) 22825–22834, <https://doi.org/10.1021/acsaami.0c02697>.
- [20] N.N. Syrbu, V.V. Zalamai, I.G. Stavom, S.I. Beril, Excitonic and electronic transitions in Me–Sb<sub>2</sub>Se<sub>3</sub> structures, *Beilstein J. Nanotechnol.* 11 (2020) 1045–1053, <https://doi.org/10.3762/bjnano.11.89>.
- [21] L. Jiajun, L. Jianming, L. Congqiang, L. Wenquan, L. Shirong, S. Wenchao, Mineralogy of the stibnite-antimonoselite series, *Int. Geol. Rev.* 41 (11) (1999) 1042–1050, <https://doi.org/10.1080/00206819909465189>.
- [22] R. Kondrotas, C. Chen, X. Liu, B. Yang, J. Tang, Low-dimensional materials for photovoltaic application, *J. Semiconduct.* 42 (2021), 031701, <https://doi.org/10.1088/1674-4926/42/3/031701>.
- [23] R. Tang, X. Wang, W. Lian, J. Huang, Q. Wei, M. Huang, Y. Yin, C. Jiang, S. Yang, G. Xing, S. Chen, C. Zhu, X. Hao, M.A. Green, T. Chen, Hydrothermal deposition of antimony selenosulfide thin films enables solar cells with 10% efficiency, *Nat. Energy* 5 (2020) 587–595, <https://doi.org/10.1038/s41560-020-0652-3>.
- [24] N. Fleck, T.D.C. Huxson, C.N. Savory, J. Buckering, T.D. Veal, M.R. Correia, D. O. Scanlon, K. Durose, F. Jäckel, Identifying Raman modes of Sb<sub>2</sub>Se<sub>3</sub> and their symmetries using angle-resolved polarised Raman spectra, *J. Mater. Chem.* 8 (2020) 8337–8344, <https://doi.org/10.1039/D0TA01783C>.
- [25] P. Sereni, M. Musso, P. Knoll, P. Blaha, K. Schwarz, G. Schmidt, Polarization-dependent Raman characterization of stibnite (Sb<sub>2</sub>S<sub>3</sub>), *AIP Conf. Proc.* 1267 (2010) 1131, <https://doi.org/10.1063/1.3482339>.
- [26] Y.A. Sorb, V. Rajaji, P.S. Malavi, U. Subbarao, P. Halappa, S.C. Peter, S. Karmakar, C. Narayana, Pressure-induced electronic topological transition in Sb<sub>2</sub>Se<sub>3</sub>, *J. Phys. Condens. Matter* 28 (2016), 015602, <https://doi.org/10.1088/0953-8984/28/1/015602>.
- [27] M. Birkett, W.M. Linhart, J. Stoner, L.J. Phillips, K. Durose, J. Alaria, J.D. Major, R. Kudrawiec, T.D. Veal, Band gap temperature-dependence of close-space sublimation grown Sb<sub>2</sub>Se<sub>3</sub> by photo-reflectance, *Appl. Mater.* 6 (2018), 084901, <https://doi.org/10.1063/1.5027157>.
- [28] T. Schmidt, K. Lischka, W. Zulehner, Excitation-power dependence of the near-band-edge photoluminescence of semiconductors, *Phys. Rev. B* 45 (1992) 8989, <https://doi.org/10.1103/PhysRevB.45.8989>.
- [29] K. Huang, A. Rhys, Theory of light absorption and non-radiative transitions in F-centres, *Proc. R. Soc. A* 204 (1950) 406–423, [https://doi.org/10.1142/9789812793720\\_0007](https://doi.org/10.1142/9789812793720_0007).
- [30] A.P. Levanyuk, V.V. Osipov, Edge luminescence of direct-gap semiconductors, *Sov. Phys. Usp.* 24 (1981) 187–215, <https://doi.org/10.1070/PU1981v024n03ABEH004770>.
- [31] F. Williams, Donor–acceptor pairs in semiconductors, *Phys. Status Solidi* 25 (1968) 493–512, <https://doi.org/10.1002/psb.19680250202>.
- [32] J. Krustok, J. Raudoja, M. Krunk, H. Mändar, H. Collan, Nature of the native deep localized defect recombination centers in the chalcopyrite and orthorhombic AgInS<sub>2</sub>, *J. Appl. Phys.* v. 88 (No 1) (2000) 205–209, <https://doi.org/10.1063/1.373644>.
- [33] F. Aousgi, M. Kanzari, Study of the optical properties of the amorphous Sb<sub>2</sub>Se<sub>3</sub> thin films, *J. Optoelectron. Adv. Mater.* 12 (2) (2010) 227–232.
- [34] J. Krustok, H. Collan, K. Hjelte, Does the low-temperature Arrhenius plot of the photoluminescence intensity in CdTe point towards an erroneous activation energy? *J. Appl. Phys.* 81 (1997) 1442–1445, <https://doi.org/10.1063/1.363903>.

## Appendix 2

### Publication II

M. E. Uslu, M. Danilson, K. Timmo, M. Grossberg-Kuusik, „The effect of tin doping on the band structure and optical properties of polycrystalline antimony selenide“, *Physica B: Condensed Matter*, 678 (2024) 415744, <https://doi.org/10.1016/j.physb.2024.415744>





# The effect of tin doping on the band structure and optical properties of polycrystalline antimony selenide

Mehmet Ender Uslu<sup>\*</sup>, Mati Danilson, Kristi Timmo, Maarja Grossberg-Kuusik

Department of Materials and Environmental Technology, Tallinn University of Technology, Ehitajate tee 5, 19086, Tallinn, Estonia

## ARTICLE INFO

**Keywords:**  
UPS study  
Sn-doped Sb<sub>2</sub>Se<sub>3</sub>  
Intrinsic Sb<sub>2</sub>Se<sub>3</sub>  
Work function

## ABSTRACT

In this study, we investigated the effect of Sn-doping on the antimony selenide (Sb<sub>2</sub>Se<sub>3</sub>) polycrystalline material to alter its optical properties and electronic band structure. Sb<sub>2</sub>Se<sub>3</sub> polycrystals were isothermally annealed at 350 °C, 400 °C, 450 °C, and 500 °C, in the presence of tin diselenide (SnSe<sub>2</sub>) in degassed quartz ampoules to introduce Tin (Sn) into the material. X-ray diffraction (XRD), Raman scattering, and energy-dispersive X-ray spectroscopy measurements confirmed the single phase of the Sb<sub>2</sub>Se<sub>3</sub> samples. Successful doping of the surface of the Sb<sub>2</sub>Se<sub>3</sub> polycrystals with Sn was confirmed by X-ray photoelectron spectroscopy for the samples annealed at 400 °C, 450 °C, and 500 °C in the presence of SnSe<sub>2</sub>. An ultraviolet photoelectron spectroscopy (UPS) study revealed a decrease in the work function ( $\phi$ ) of the Sb<sub>2</sub>Se<sub>3</sub> polycrystals from 4.34 eV to 3.14 eV due to Sn doping implemented at 500 °C. Moreover, a small shift of the Fermi level towards the valence band maximum (VBM) by 30 meV resulted from Sn-doping at 500 °C as was detected by UPS, indicating a slightly enhanced p-type behaviour of the surface region of the Sb<sub>2</sub>Se<sub>3</sub> polycrystals. Ultraviolet–visible spectroscopy (UV–Vis) confirmed that Sn doping did not change the bandgap energy of Sb<sub>2</sub>Se<sub>3</sub> polycrystals, being 1.25 eV at room temperature (RT) for the undoped as well as Sn-doped material.

## 1. Introduction

Antimony selenide (Sb<sub>2</sub>Se<sub>3</sub>) is an inorganic binary semiconductor compound from the V<sub>2</sub>–VI<sub>3</sub> group with highly anisotropic properties due to a quasi-one-dimensional nanoribbon structure. Sb<sub>2</sub>Se<sub>3</sub> is being developed as an emerging absorber material for thin film solar cells due to its low toxicity, an optimal bandgap energy for solar energy conversion (around 1.2 eV at room temperature), and an absorption coefficient higher than 10<sup>4</sup> cm<sup>-1</sup> at visible wavelengths. Power conversion efficiency close to 11 % has recently been achieved with Sb<sub>2</sub>Se<sub>3</sub>/CdS-based thin film solar cells, being at about one-third of the theoretical maximum efficiency [1,2]. There are many challenges to be solved to improve the performance of Sb<sub>2</sub>Se<sub>3</sub>-based solar cells including its complex defect chemistry and intrinsic carrier concentration of 1.8 × 10<sup>13</sup> cm<sup>-3</sup> [3] which is considered low for an optimal photovoltaic absorber material. One way to tackle the problem of low carrier concentrations in Sb<sub>2</sub>Se<sub>3</sub> is to introduce extrinsic dopants to the material. Despite being a single-phase compound with a binary chemical composition, the unit cell of Sb<sub>2</sub>Se<sub>3</sub> consists of 20 atoms, which makes its defect structure rather complicated and still not fully understood. Ribbon-like structured

Sb<sub>4</sub>Se<sub>6</sub> atomic chains shown in Fig. 1 have two inequivalent Sb sites, and three inequivalent Se sites labelled Sb1, Sb2, Se1, Se2, and Se3, respectively [4,5]. In the defect-free ideal case, Sb1 is supposed to be bonded with five Se atoms around, while Sb2 is bonded with two neighbouring Se atoms. Stable antimony ions can have a charge state of +5 or +3, while antimony's valence electron configuration is 5s<sup>2</sup>5p<sup>3</sup>. Computational density functional theory calculations predict that Sb gives the three 5p<sup>3</sup> electrons to neighbouring Se atoms as Sb-5p states form unoccupied conduction bands, but the Sb-5s states create hybrid bonds with Se-4p states in the valence band of antimony selenide [4]. It is also suggested by Chen et al. [4] that Se<sub>Sb1</sub> and Se<sub>Sb2</sub> defect sites have -1 charge states acting as an antibonding acceptor close to the valence band (VB) edge, being a hole trap. However, both types of Se<sub>Sb</sub> and Sb<sub>Se1</sub> sites are pointed out by Savory et al. [5] as amphoteric defects (+1/-1), which could be acting as recombination centres with mid-band gap transition levels. The mid-band gap defect of the close donor-acceptor pair (DAP) is also reported experimentally by temperature and power-dependent photoluminescence (PL) studies on Sb<sub>2</sub>Se<sub>3</sub> [6,7]. Extrinsic dopants might passivate such complex defects and therefore reduce the recombination losses in the absorber material. For instance,

<sup>\*</sup> Corresponding author.

E-mail address: [meuslu@taltech.ee](mailto:meuslu@taltech.ee) (M.E. Uslu).

<https://doi.org/10.1016/j.physb.2024.415744>

Received 11 January 2024; Received in revised form 29 January 2024; Accepted 3 February 2024

Available online 6 February 2024

0921-4526/© 2024 Elsevier B.V. All rights reserved.

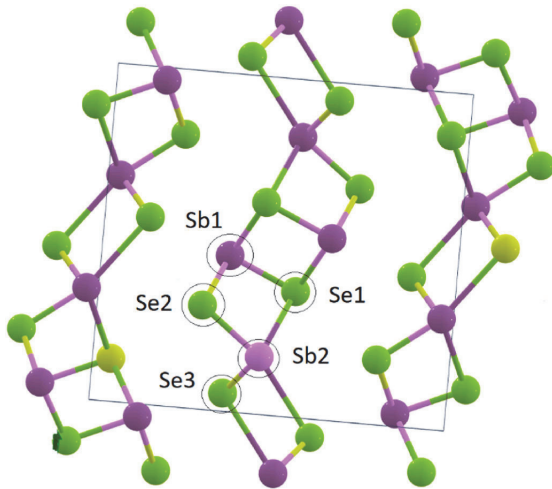


**Fig. 1.** Ribbon-like crystal structure of  $\text{Sb}_2\text{Se}_3$ . The non-equivalent Sb and Se atomic sites in an atomic chain are labelled as Sb1, Sb2, Se1, Se2, and Se3, respectively. The borders of the unit cell are indicated with the black lines. The figure is adapted from <https://next-gen.materialsproject.org/materials/mp-2160/>.

Tin (Sn) from the IV<sub>A</sub> group can be an outstanding substitutional dopant in  $\text{Sb}_2\text{Se}_3$  with chemical and physical properties comparable to Antimony (Sb). Substituting Sb with Sn is expected to increase the hole concentration in  $\text{Sb}_2\text{Se}_3$  since Sn has one less valence electron. However, it must be considered that in the case of sufficient concentration of Sn, several stable phases with selenium can form, such as  $\alpha$ -SnSe (orthorhombic) [8],  $\pi$ -SnSe (cubic) [9] and SnSe<sub>2</sub> (hexagonal) [10,11]. Nevertheless, introducing Sn doping into a (Zr,Hf)Co(Sb<sub>1-x</sub>Sn<sub>x</sub>) system was found to increase the hole mobility and p-type electrical conductivity of the compound [12]. Moreover, photo-electrochemical measurements on  $(\text{Sn}_x\text{Sb}_{1-x})_2\text{Se}_3$ , where x was up to 0.1, revealed fourteen times higher photoelectric current and ten times higher dark current as a result of Sn introduction to  $\text{Sb}_2\text{Se}_3$  [13]. Patel et al. [14] and Hobson et al. [15] have also detected improved p-type conductivity of Sn-doped  $\text{Sb}_2\text{Se}_3$  from temperature-dependent resistance measurements and Hall measurements, respectively. However, the ultraviolet photoelectron spectroscopy (UPS) of Sn-doped  $\text{Sb}_2\text{Se}_3$  has not been studied, which would add valuable information about the influence of Sn doping on the electronic band structure of  $\text{Sb}_2\text{Se}_3$ . A detailed comparative study of undoped and Sn-doped  $\text{Sb}_2\text{Se}_3$  polycrystals using UPS, and ultraviolet-visible (UV-Vis) spectroscopy to gain knowledge about the influence of Sn doping on the optical properties and electronic structure of  $\text{Sb}_2\text{Se}_3$  is conducted in this work.

## 2. Materials and methods

Polycrystalline antimony selenide  $\text{Sb}_2\text{Se}_3$  was synthesized from Sb and Se elemental precursors of 5 N purity from Alfa Aesar at 500 °C in degassed and sealed quartz ampoules. From the synthesized polycrystalline  $\text{Sb}_2\text{Se}_3$  powder 200 mg portions of material were extracted for Sn doping, which was achieved by isothermal post-annealing of the four portions of  $\text{Sb}_2\text{Se}_3$  material at 350 °C, 400 °C, 450 °C, 500 °C, respectively, together with 0.04 g of SnSe<sub>2</sub> pellets (self-synthesized) for 30 min in degassed and sealed 0.06 m long quartz ampoules.  $\text{Sb}_2\text{Se}_3$  and SnSe<sub>2</sub> are placed non-attached at a 0.05 m distance in the ampoules.

## 3. Experimental

The elemental compositions of the synthesized polycrystals were

determined by energy-dispersive X-ray spectroscopy (EDS) using a Bruker Esprit 1.8 system on Zeiss Merlin high-resolution scanning electron microscope. The phase composition of  $\text{Sb}_2\text{Se}_3$  polycrystals was studied by using room-temperature micro-Raman analysis with Horiba's LabRam HR800 spectrometer with a 532 nm laser line and with a spot size of 10  $\mu\text{m}$  in diameter. The Raman analysis was complemented by the powder X-ray diffraction (XRD) analysis using a Rigaku Ultima IV diffractometer operating with the silicon strip detector D/tEX Ultra. Sn-doping of the  $\text{Sb}_2\text{Se}_3$  polycrystals was confirmed for the samples annealed in the presence of SnSe<sub>2</sub> at 400 °C, 450 °C and 500 °C by X-ray photoelectron spectroscopy (XPS) using the Kratos Analytical AXIS ULTRA DLD spectrometer fitted with the monochromatic Al K $\alpha$  X-rays source and the achromatic Mg K $\alpha$ /Al K $\alpha$  dual anode X-ray source. The depth profiling of elemental composition was obtained by Ar<sup>+</sup> ion sputtering using Ta<sub>2</sub>O<sub>3</sub> reference sample with known thickness for evaluation of the sputtering depth.

UPS analysis was performed using an Axis Ultra DLD photoelectron spectrometer (Kratos Analytical) fitted with a helium discharge lamp. The He discharged lamp with resonance line He(I) ( $h\nu = 21.22$  eV) was used to obtain UPS spectra. Before the measurement, the Ag foil and the  $\text{Sb}_2\text{Se}_3$  and  $\text{Sb}_2\text{Se}_3$ :Sn polycrystalline sample surfaces were cleaned by argon ion sputtering (4 keV, 10 mA) for 2 min. A bias of  $-9.124$  V was used to separate the analyser and the secondary edges of the sample, and the bias was optimized to shift the Ag spectrum into the linear region of the analyser (kinetic energy of 0–10 eV). A spectrometer with a pass energy of 5 eV and a large area aperture of 300  $\mu\text{m} \times 700 \mu\text{m}$  was used. Under these conditions, the energy resolution of the spectra was measured at the Fermi edge of the clean Ag foil at room temperature (RT). Energy band gaps of the samples were determined by ultraviolet-visible spectroscopy using a Shimadzu UV-1800 spectrophotometer equipped with a specular reflector.

## 4. Results and discussion

The four different samples, which were post-annealed at temperatures ranging from 350 °C to 500 °C in the presence of SnSe<sub>2</sub> were labelled as SbSe\_350, SbSe\_400, SbSe\_450, and SbSe\_500 based on the processing temperatures. The un-annealed and un-doped reference sample was labelled as SbSe\_0. As shown in Fig. 2, no secondary phases nor  $(\text{Sb}_x\text{Sn}_{1-x})_2\text{Se}_3$  alloy formation could be detected by XRD using an ICDD 01-083-7430 data card in the Rietveld analysis. Room temperature micro-Raman (shown in Fig. 1S) as well as EDS analysis results presented in Table 1 also confirmed the uniform single-phase composition of the  $\text{Sb}_2\text{Se}_3$  polycrystals. EDS analysis revealed the slightly Sb-rich composition of the  $\text{Sb}_2\text{Se}_3$  samples. The error margin of EDS analysis was around 1.5 atomic %. Therefore, it is expected that EDS and either XRD analysis do not indicate any tin content in the samples since the doping concentration of tin should be sufficiently small, so unwanted secondary phases did not form in  $\text{Sb}_2\text{Se}_3$  because of the post-thermal process with SnSe<sub>2</sub>. On the other hand, the highly sensitive XPS analysis enabled to detect the presence of Sn on the surface of the thermally processed  $\text{Sb}_2\text{Se}_3$  polycrystals. The Sn 3d<sub>5/2</sub> and Sn 3d<sub>3/2</sub> peaks at 486 eV and 495 eV, respectively, were detected by the XPS as shown in Fig. 3a as reported by Karuna K. Nanda et al. [16]. However, after 60 s of Argon ion sputtering (corresponding to 5 nm thickness of the material), only the SbSe\_500 sample showed significant intensity of the Sn 3d<sub>5/2</sub> and Sn 3d<sub>3/2</sub> peaks (see Fig. 3b) and was therefore chosen for further analysis. The XPS survey spectra of  $\text{Sb}_2\text{Se}_3$  polycrystalline samples before and after Argon ion sputtering are shown in Fig. 2S. The XPS peaks of  $\text{Sb}_2\text{Se}_3$  are in correspondence with the ones presented by C. H. Don et al. [17].

To learn about the influence of Sn-doping on the electronic band structure of  $\text{Sb}_2\text{Se}_3$  polycrystals, an UPS study was conducted on the SbSe\_0 and SbSe\_500 samples. For the UPS measurements, the pressure of the Helium lamp is optimized for maximum signal and stability. The UV excitation intensity and the angle of the sample plane with the UV

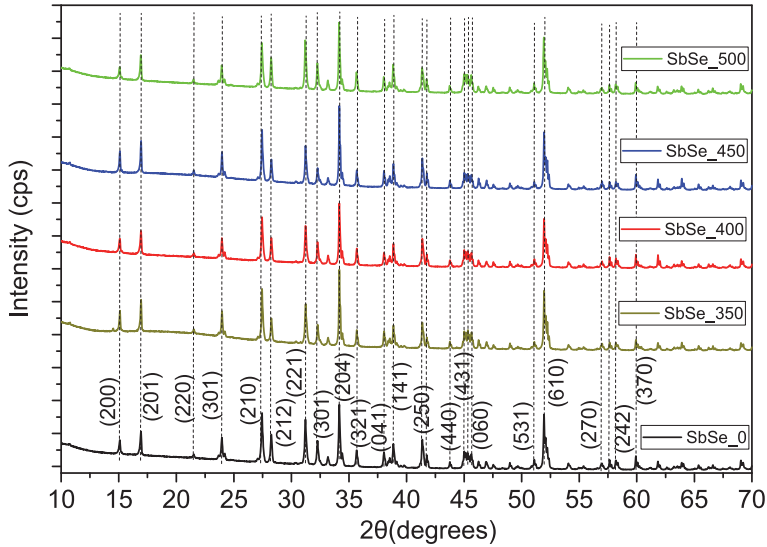


Fig. 2. XRD patterns of the Sn doped and reference  $\text{Sb}_2\text{Se}_3$  polycrystals showing single-phase material composition matching the reference  $\text{Sb}_2\text{Se}_3$  on ICDD 01-083-7430.

Table 1

Elemental compositions of the studied  $\text{Sb}_2\text{Se}_3$  and Sn-doped  $\text{Sb}_2\text{Se}_3$  polycrystalline samples determined by EDS.

	SbSe_0	SbSe_350	SbSe_400	SbSe_450	SbSe_500
Antimony [at.%]	41.31 ± 1.5	40.41 ± 1.4	40.11 ± 1.6	40.35 ± 1.4	40.97 ± 1.5
Selenium [at.%]	58.69 ± 1.4	59.59 ± 1.4	59.89 ± 1.6	59.65 ± 1.4	59.03 ± 1.4

source were kept identical for both SbSe\_0 and SbSe\_500. Fig. 4a and b presents a comparison of the combined He(I)-UPS spectra for SbSe\_0 and SbSe\_500 at the binding energy and kinetic energy scales, to see a relative difference between their work functions, as  $\Phi_{\text{SbSe}_0} = E_{\text{vacuum}} - E_f$ , SbSe\_0 and  $\Phi_{\text{SbSe}_500} = E_{\text{vacuum}} - E_f$ , SbSe\_500, respectively. Further to that, work functions of SbSe\_0 and SbSe\_500 were accurately calculated by using Equation (1), as pointed out respectively in Fig. 5a and b.

$$\Phi = hv - E_{\text{cutoff}} \quad (1)$$

where  $\Phi$  is the work function,  $hv$  is the excitation energy of He(I) line = 21.22 eV, and  $E_{\text{cutoff}}$  is the secondary electron cutoff energy extracted with a linear fitting at the high binding energy spectra in Fig. 4. From Equation (1), the work function of SbSe\_0 is  $\Phi = 21.22 \text{ eV} - 16.83 \text{ eV} = 4.39 \text{ eV}$  on the surface and  $\Phi = 21.22 \text{ eV} - 16.88 \text{ eV} = 4.34 \text{ eV}$  beneath the surface after Ar-sputtering, while lower values were obtained for SbSe\_500, namely  $\Phi = 21.22 \text{ eV} - 17.92 \text{ eV} = 3.3 \text{ eV}$  on the surface and  $\Phi = 21.22 \text{ eV} - 18.08 \text{ eV} = 3.14 \text{ eV}$  after the Ar-sputtering.

The Sn-doping process also altered the valence band onset ( $VB_{\text{onset}}$ ) in polycrystalline  $\text{Sb}_2\text{Se}_3$ . With the binding energy spectrum plotted regarding the Fermi level (0 eV) in Fig. 5a and b for SbSe\_0 and SbSe\_500, respectively, the  $VB_{\text{onset}}$  values were also determined by drawing tangent lines at the cutoff and the baselines [18]. In the tangent lines obtained by linear fittings, slope values from the binding energy spectra of SbSe\_500 decrease compared to those of SbSe\_0. Therefore, the energetic distance between the valence band maximum (VBM) and Fermi level on the surface is determined as  $E_f - E_{\text{VB}} = 0.46 \text{ eV}$  and  $0.40 \text{ eV}$  for SbSe\_0 and SbSe\_500, respectively. After cleaning the sample

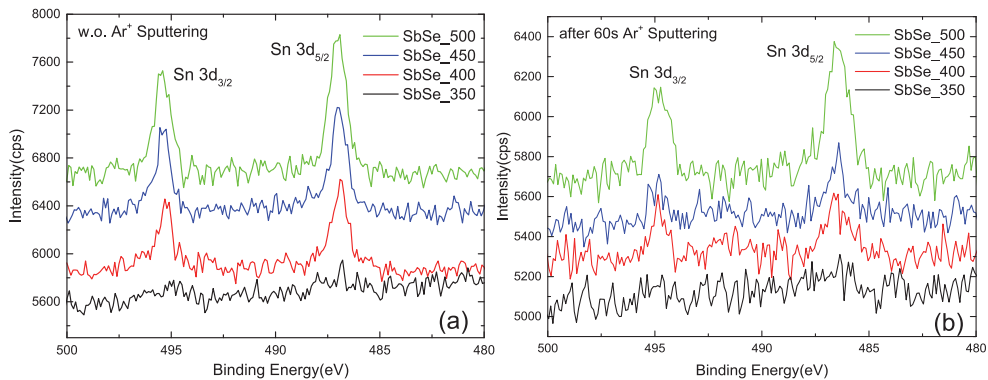


Fig. 3. Sn - 3d doublets determined by XPS a) from the surface of the Sn-doped  $\text{Sb}_2\text{Se}_3$  polycrystals and b) after 60 s of Argon-ion sputtering corresponding to the removal of 0.5 nm of the surface layer.

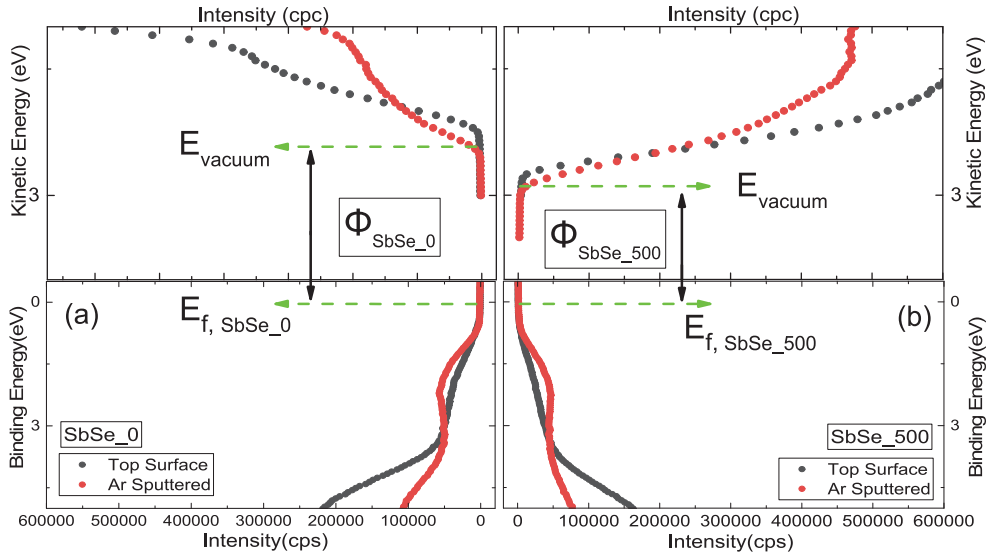


Fig. 4. Work function ( $\phi$ ) shown by using the combined UPS spectra referring to the Fermi level (0 eV) for a) the SbSe<sub>0</sub> (reference) sample, and b) the SbSe<sub>500</sub> sample, which is Sn-doped at 500 °C.

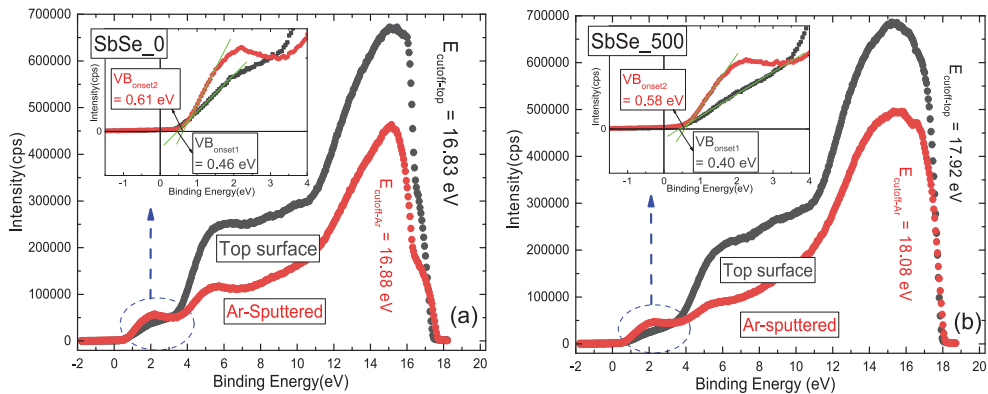


Fig. 5.  $E_{cutoff}$  values linearly fitted on the UPS spectra in binding energy scale before and after Ar-ion sputtering, and the onset of the valence band ( $VB_{onset}$ ) at low binding energy a) for the SbSe<sub>0</sub> reference sample and b) for the SbSe<sub>500</sub>, Sn-doped sample.

surfaces by Ar-sputtering,  $E_f - E_{VB} = 0.61$  eV and 0.58 eV beneath the surface for SbSe<sub>0</sub> and SbSe<sub>500</sub>, respectively. For SbSe<sub>500</sub>, the Fermi level is positioned closer to the valence band, both on the material's surface and beneath the surface. The difference between the Fermi levels is relatively small but still indicates that higher Sn contents could lead to more enhanced p-type conductivity. For that alternative Sn doping procedures could be developed enabling enhanced Sn doping levels.

In addition, in Fig. 4, the UPS measurement at kinetic energy takes the cutoff at the low binding energy of the Ag foil in the sample holder as the reference (0 eV). However, if we had calculated the UPS ionization energies based on the vacuum level, then, due to its lower work function value, the band structure of SbSe<sub>500</sub> would have arranged in lower ionization energies than the band structure of SbSe<sub>0</sub> does. Therefore, SbSe<sub>500</sub> might have no spike-like energy barrier for photo-excited electrons in an energy band alignment with cadmium sulphide (CdS) buffer layer in a typical thin film solar cell since the work function of CdS thin film is reported to be around 3.91 eV [19].

Any post-thermal treatment can alter the crystallinity and defect structure of a semiconductor material. The Sn doping method, which we applied on SbSe<sub>0</sub> (reference sample) using annealing at different temperatures in the presence of SnSe<sub>2</sub> pellets is also a thermal process. To understand if the differences in the Fermi energy level, and the work function derived from the UPS data on SbSe<sub>500</sub> are related only to Sn-doping, or to which there is also a contribution by the process temperature, the UPS analysis was repeated on a parallel series of Sb<sub>2</sub>Se<sub>3</sub> polycrystals which were annealed at the same temperatures and duration without the presence of SnSe<sub>2</sub> pellets. The post-thermally treated un-doped Sb<sub>2</sub>Se<sub>3</sub> revealed a decreased work function by around 0.3 eV compared to SbSe<sub>0</sub>, while the difference in work functions between SbSe<sub>0</sub> and SbSe<sub>500</sub> was more than 1 eV. This indicates that there is also an effect of temperature on the band structure of Sb<sub>2</sub>Se<sub>3</sub>, which is however significantly smaller than the effect of Sn-doping. Additionally, although  $E_f - E_{VB}$  was smaller in SbSe<sub>500</sub> than it was in SbSe<sub>0</sub>, the difference of  $E_f - E_{VB} = 0.62$  meV in SbSe<sub>0</sub> remained unchanged for the

undoped  $\text{Sb}_2\text{Se}_3$  post-thermally treated at 500 °C. On the other hand, to compare the post-thermal treatment and tin doping method of  $\text{Sb}_2\text{Se}_3$  for an identical process temperature, it is important to consider their partial chemical pressures.  $\text{Sb}_2\text{Se}_3$  and  $\text{SnSe}_2$  have partial pressures of 0.45 Torr [20] and 0.75 Torr [21], respectively, at 500 °C, where other partial pressures from elemental Sb and Sn are negligible. The partial pressure of selenium, originating from  $\text{SnSe}_2$  or  $\text{Sb}_2\text{Se}_3$  sources, at 500 °C is the highest since it is quite a volatile material with high pressures at elevated temperatures. However, the partial pressure of selenium either from  $\text{Sb}_2\text{Se}_3$  or from  $\text{SnSe}_2$  is much less than the pressure that would be sourced from pure selenium [22]. The reported values above imply that partial pressures originating from the dopant  $\text{SnSe}_2$  can outbalance the partial pressures from  $\text{Sb}_2\text{Se}_3$  in the tin doping method applied in this study. There is no balancing pressure for  $\text{Sb}_2\text{Se}_3$  in the post-thermal treatment in vacuum at 500 °C, in which partial pressure from elemental selenium would tend to generate selenium vacancy. Therefore, we conclude that the results from the UPS analysis on  $\text{SbSe}_0$ , regarding the reference sample ( $\text{SbSe}_0$ ), mainly arise from Sn introduction in  $\text{Sb}_2\text{Se}_3$ .

In the final step, UV–Vis spectroscopy in reflection measurement mode was used to determine the band gap energy of the studied samples  $\text{SbSe}_0$  and  $\text{SbSe}_0.500$ . Transmittance spectra could not be measured due to the high absorption coefficient of  $\text{Sb}_2\text{Se}_3$  in the visible range, and the large particle size of the polycrystalline powder samples ranging from 50 to 100  $\mu\text{m}$  in diameter. The absorption coefficient, which matches values reported in the literature [23,24], for both samples was calculated as  $4.5 \times 10^4 \text{ cm}^{-1}$ . As shown in Fig. 6, the same band gap energy value of 1.25 eV at room temperature was found from the reflectance spectra by using the Tauc plot of Kubelka–Munk transformation ( $F(R)$ ) [25,26] for both samples. The band gap energy of  $\text{Sb}_2\text{Se}_3$  does not change after the Sn-doping process since the level of Sn involvement in  $\text{SbSe}_0.500$  remained sufficiently small as was shown by the XRD, EDS and XPS analyses.

To summarize, we have shown in this study that Sn-doping could be a way to improve the p-type conductivity of the  $\text{Sb}_2\text{Se}_3$  absorbers, which have been shown to suffer from low carrier concentrations [3]. The information about the work function of undoped and Sn-doped  $\text{Sb}_2\text{Se}_3$  absorber enables more precise design of the p-n junction interface between the undoped as well as doped  $\text{Sb}_2\text{Se}_3$  absorber and possible n-type buffer layer. An optimized p-n junction interface is another critical prerequisite for high-performance solar cells in addition to optimal carrier concentration and low recombination losses.

## 5. Conclusion

The UPS study showed that tin-doped  $\text{Sb}_2\text{Se}_3$  has a much smaller work function and a Fermi level slightly closer to the VBM although intrinsic  $\text{Sb}_2\text{Se}_3$  ( $\text{SbSe}_0$ ) and tin-doped  $\text{Sb}_2\text{Se}_3$  ( $\text{SbSe}_0.500$ ), both samples having the same band gap of around 1.25 eV as detected by UV–Vis spectroscopy. It can be concluded that tin-doping enabled slight improvement in the p-type conductivity of the surface region of the  $\text{Sb}_2\text{Se}_3$  and could be further tested in different types of  $\text{Sb}_2\text{Se}_3$  samples using alternative doping procedures, which would enable higher doping concentrations and accordingly stronger effect of Sn-doping.

## CRedit authorship contribution statement

**Mehmet Ender Uslu:** Writing – review & editing, Writing – original draft, Visualization, Validation, Software, Methodology, Investigation, Formal analysis, Data curation, Conceptualization. **Mati Danilson:** Writing – review & editing, Validation, Formal analysis, Data curation. **Kristi Timmo:** Writing – review & editing, Methodology, Investigation, Conceptualization. **Maarja Grossberg-Kuusk:** Writing – review & editing, Validation, Supervision, Software, Resources, Methodology, Investigation, Funding acquisition, Conceptualization.

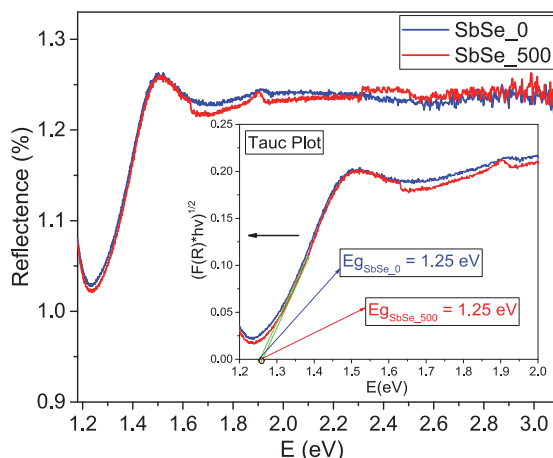


Fig. 6. Photoreflectance (in percentage, %) measured by UV–Vis spectroscopy and energy bandgap values calculated by using the Tauc plot for  $\text{SbSe}_0$ , and for  $\text{SbSe}_0.500$ .

## Declaration of competing interest

The authors declare that they have no known competing financial interests or personal relationships that could have appeared to influence the work reported in this paper. Maarja Grossberg-Kuusk reports financial support was provided by Estonian Research Council. If there are other authors, they declare that they have no known competing financial interests or personal relationships that could have appeared to influence the work reported in this paper.

## Data availability

Data will be made available on request.

## Acknowledgements

This work was supported by the Estonian Research Council [grant number PRG1023]; and M-ERA.net project [grant number MNHA23040].

## Appendix A. Supplementary data

Supplementary data to this article can be found online at <https://doi.org/10.1016/j.physb.2024.415744>.

## References

- [1] Yuqi Zhao, Tao Chen, Xudong Xiao, Jianmin Li, et al., Regulating deposition kinetics via a novel additive-assisted chemical bath deposition technology enables fabrication of 10.57%-efficiency  $\text{Sb}_2\text{Se}_3$  solar cells, *Energy Environ. Sci.* 15 (2022) 5118–5128, <https://doi.org/10.1039/D2EE02261C>.
- [2] Yaohua Mai, Zhiqiang Li, et al.,  $\text{Sb}_2\text{Se}_3$  thin-film solar cells Exceeding 10% power conversion efficiency enabled by injection vapor deposition technology, *Adv. Mater.* 34 (2022) 2202969, <https://doi.org/10.1002/adma.202202969>.
- [3] T.A.N.G. Jiang, Chao Chen, et al., Characterization of basic physical properties of  $\text{Sb}_2\text{Se}_3$  and its relevance for photovoltaics, *Front. Optoelectron.* 10 (1) (2017) 18–30, <https://doi.org/10.1007/s12200-017-0702-z>.
- [4] Shiyu Chen, et al., Complicated and unconventional defect properties of the quasi-dimensional photovoltaic semiconductor  $\text{Sb}_2\text{Se}_3$ , *ACS Appl. Mater. Interfaces* 11 (2019) 15564–15572, <https://doi.org/10.1021/acsami.9b01220>.
- [5] Christopher N. Savory, Davis O. Scaldon, The complex defect chemistry of antimony selenide, *J. Mater. Chem. A* 7 (2019) 10739, <https://doi.org/10.1039/C9TA02022E>.
- [6] M. Grossberg, et al., *J. Alloys Compd* 817 (2020) 152716, <https://doi.org/10.1016/j.jallcom.2019.152716>. *J. Alloys Compd.* 817 (2020) 152716.

- [7] M.E. Uslu, et al., Study of the optical properties of  $\text{Sb}_2(\text{Se}_{1-x}\text{S}_x)_3$  ( $x = 0-1$ ) solid solutions, *Materials Science in Semiconductor Processing* 144 (2022) 106571, <https://doi.org/10.1016/j.mssp.2022.106571>.
- [8] M. Taniguchi, R.L. Johnson, J. Ghijsen, M. Cardona, Core excitons and conduction-band structures in orthorhombic GeS, GeSe, SnS, and SnSe single crystals, *Phys. Rev. B* 42, 3634. <https://doi.org/10.1103/PhysRevB.42.3634>.
- [9] Yuval Golan, et al., A new nanocrystalline binary phase: synthesis and properties of cubic tin monoselenide, *CrystEngComm* 18 (2016) 1918–1923, <https://doi.org/10.1039/c5ce02437d>.
- [10] E.P. Mukhokosi, S.B. Krupanidhi, K.K. Nanda, Band gap engineering of hexagonal  $\text{SnSe}_2$  nanostructured thin films for infra-red photodetection, *Sci. Rep.* 7 (2017) 1–10, <https://doi.org/10.1038/s41598-017-15519-x>.
- [11] Vidya Nand Singh, et al., Tin-selenide as a futuristic material: properties and applications, *RSC Adv* 11 (2021) 6477, <https://doi.org/10.1039/D0RA09807H>.
- [12] S.R. Culp, J.W. Simonson, et al., (Zr,Hf)Co(Sb,Sn) half-Heusler phases as high-temperature ( $>700^\circ\text{C}$ ) p-type thermoelectric materials, *Appl. Phys. Lett.* 93 (2008) 022105, <https://doi.org/10.1063/1.2959103>.
- [13] Xianping Fan, Xianghua Zhang, et al., Enhanced electrical conductivity and photoconductive properties of Sn-doped  $\text{Sb}_2\text{Se}_3$  crystals, *J. Mater. Chem. C* 6 (2018) 6465, <https://doi.org/10.1039/C8TC01683F>.
- [14] H.M. Patel, B.P. Modi, et al., Recent advances to enhance electrical and photoelectrical properties of antimony selenide crystals via tin doping, *Journal of Electronic Materials* 52 (2023) 196–208, <https://doi.org/10.1007/s11664-022-09963-3>.
- [15] Theodore D.C. Hobson, et al., P-type conductivity in Sn-doped  $\text{Sb}_2\text{Se}_3$ , *J. Phys. Energy* 4 (2022) 045006, <https://doi.org/10.1088/2515-7655/ac91a6>.
- [16] Karuna K. Nanda, et al., Band gap engineering of hexagonal  $\text{SnSe}_2$  nanostructured thin films for infra-red photodetection, *Scientific Reports* 7 (2017), <https://doi.org/10.1038/s41598-017-15519-x>. Article number: 15215.
- [17] Christopher H. Don, Tim D. Veal, et al., Sb  $5s^2$  lone pairs and band alignment of  $\text{Sb}_2\text{Se}_3$ : a photoemission and density functional theory study, *J. Mater. Chem. C* 8 (2020) 12615, <https://doi.org/10.1039/D0TC03470C>.
- [18] James E. Whitten, Ultraviolet photoelectron spectroscopy: practical aspects and best practices, *Applied Surface Science Advances* 13 (2023) 100384, <https://doi.org/10.1016/j.apsadv.2023.100384>.
- [19] Tim D. Veal, et al., Natural band alignments and band offsets of  $\text{Sb}_2\text{Se}_3$  solar cells, *ACS Appl. Energy Mater.* 3 (12) (2020) 11617–11626, <https://doi.org/10.1021/acsaem.0c01477>.
- [20] Xincheng Liu, Tang Jiang, et al., Thermal evaporation and characterization of  $\text{Sb}_2\text{Se}_3$  thin film for substrate  $\text{Sb}_2\text{Se}_3/\text{CdS}$  solar cells, *ACS Appl. Mater. Interfaces* 6 (2014) 10687–10695, <https://doi.org/10.1021/am502427s>.
- [21] Liyong Yao, Jianping Ao, Ming-Jer Jeng, et al., CZTSe solar cells prepared by electrodeposition of Cu/Sn/Zn stack layer followed by selenization at low Se pressure, *Nanoscale Res Lett* 9 (1) (2014) 678, <https://doi.org/10.1186/1556-276X-9-678>.
- [22] E.H. Baker, The vapour pressure and resistivity of selenium at high temperatures, *J. Chem. Soc. A* (1968) 1089–1092, <https://doi.org/10.1039/J19680001089>.
- [23] Xincheng Liu, Tang Jiang, et al., Thermal evaporation and characterization of  $\text{Sb}_2\text{Se}_3$  thin film for substrate  $\text{Sb}_2\text{Se}_3/\text{CdS}$  solar cells, *ACS Appl. Mater. Interfaces* 6 (2014) 10687–10695, <https://doi.org/10.1021/am502427s>.
- [24] Job Jea Woong, Jae Ko Min, et al., The Enhanced photovoltaic performance of solution-processed  $\text{Sb}_2\text{Se}_3$  thin film solar cells by optimizing device structure, *Current Applied Physics* 20 (2020) 282–287, <https://doi.org/10.1016/j.cap.2019.11.018>.
- [25] Prince George, Pradip Chowdhury, Prince George, Pradip Chowdhury, *Analyst* 144 (2019) 3005–3012, <https://doi.org/10.1039/c8an02257g>.
- [26] P. Falaras, et al., Nitrogen modified nanostructured titania: electronic, structural and visible-light photocatalytic properties, *phys. stat. sol. (RRL)* 2 (No. 2) (2008) 83–85, <https://doi.org/10.1002/pssr.200802006>.

## Appendix 3

### Publication III

M. E. Uslu, K. Muska, M. Pilvet, S. Bereznev, V. Mikli, M. Kauk-Kuusik, M. Grossberg-Kuusik, „Enhanced grain orientation in  $\text{Sb}_2\text{Se}_3$  thin films deposited on Mo/BSG substrates via RF-sputtering and selenization“, Materials Science in Semiconductor Processing, 184 (2024) 108835, <https://doi.org/10.1016/j.mssp.2024.108835>





Contents lists available at ScienceDirect

## Materials Science in Semiconductor Processing

journal homepage: [www.elsevier.com/locate/mssp](http://www.elsevier.com/locate/mssp)

## Enhanced grain orientation in Sb<sub>2</sub>Se<sub>3</sub> thin films deposited on Mo/BSG substrates via RF-sputtering and selenization

Mehmet Ender Uslu<sup>\*</sup>, Katri Muska, Maris Pilvet, Sergei Bereznev, Valdek Mikli, Marit Kauk-Kuusik, Maarja Grossberg-Kuusik

Department of Materials and Environmental Technology, Tallinn University of Technology, Ehitajate Tee 5, 19086, Tallinn, Estonia

### ABSTRACT

The alignment of the Sb<sub>2</sub>Se<sub>3</sub> absorber grains along the *c*-axis, resulting from their quasi-1D ribbon-like growth, has been found to enhance current density, thereby enabling high power conversion efficiencies in Sb<sub>2</sub>Se<sub>3</sub>-based thin film solar cells. This study presents a controllable method for depositing Sb<sub>2</sub>Se<sub>3</sub> thin films with highly oriented grains and a compact morphology, making them suitable for large-scale solar cell applications. A combination of magnetron sputtering and post-deposition isothermal selenization techniques was used. This process involved sputtering antimony onto Mo-coated Borosilicate glass (BSG) substrates, followed by selenizing the films at different temperatures in argon-gas filled quartz ampoules. The influence of several partial Ar-gas pressures and selenization temperatures on the grain growth was studied to achieve enhanced preferred grain orientations and compact morphology of the Sb<sub>2</sub>Se<sub>3</sub> thin films. Selenization at 380 °C resulted in dominant vertical grain orientations with respect to the substrate surface of the Sb<sub>2</sub>Se<sub>3</sub>, as confirmed by scanning electron microscopy and X-ray diffraction analysis, without compromising surface compactness. Although occasional micro-voids remain in the films, further optimization could eliminate these imperfections. The developed sequential method, where Sb layer was deposited by RF-sputtering process, followed by an annealing at elevated temperature in the presence of Se and argon gas pressure, holds potential for large-scale production and the fabrication of other quasi-1D chalcogenide thin films.

### 1. Introduction

Antimony selenide (Sb<sub>2</sub>Se<sub>3</sub>) is emerging as a compelling contender in the field of thin-film solar cell technologies, driven by its unique properties. Positioned within the V<sub>2</sub>-VI<sub>3</sub> group, its quasi-one-dimensional (1D) nanoribbon-like grain structure provides it with unusual anisotropic properties, setting it apart from conventional absorber materials. This structural configuration, coupled with its optimal bandgap energy, ranging in literature from 1.16 eV [1] to 1.2 eV [2], and an exceptional absorption coefficient exceeding 10<sup>4</sup> cm<sup>-1</sup> [3,4] across visible wavelengths, positions Sb<sub>2</sub>Se<sub>3</sub> as a promising thin film absorber material for efficient solar energy conversion.

Recent advances in research have highlighted the potential of Sb<sub>2</sub>Se<sub>3</sub>, as evidenced by power conversion efficiencies reaching close to 11 % in the case of Sb<sub>2</sub>Se<sub>3</sub>/CdS-based thin-film solar cells [5,6]. While this marks significant progress, it still falls short of the theoretically predicted efficiency, suggesting the existence of untapped potential for further enhancement. However, the journey toward unlocking the full capabilities of Sb<sub>2</sub>Se<sub>3</sub>-based solar cells is not without its challenges. Complexities arising from its defect chemistry [7–10] and relatively low intrinsic carrier concentration, which has been measured at 1.8 × 10<sup>13</sup> cm<sup>-3</sup> [11], present obstacles to achieving high solar cell device

performance. These challenges underscore the need for continued research and innovation in this field to overcome these limitations and realize the potential of Sb<sub>2</sub>Se<sub>3</sub> as a viable absorber material for efficient solar energy conversion.

The maximum power conversion efficiencies of Sb<sub>2</sub>Se<sub>3</sub>-based solar cells have been attributed to the enhanced current density resulting from the improved alignment of the grains in particular directions, including (221), (211), and particularly (001) due to its 1D ribbon-like grain structure [12]. However, the boundaries between these grains, stacked together by van der Waals forces, create obstructive spaces that degrade charge-carrier transport in (hk0) directions [13]. Consequently, the anisotropic crystal structure represents the third limiting factor for the energy conversion efficiency of Sb<sub>2</sub>Se<sub>3</sub>-based solar cells. To address this challenge, several studies are focusing on enhancing the crystal quality and controlling the grain orientation. Methods such as utilizing a MoSe<sub>2</sub> interlayer to facilitate Sb<sub>2</sub>Se<sub>3</sub> nanorod array growth [14], growing Sb<sub>2</sub>Se<sub>3</sub> nanowires on a two-dimensional (2D) WS<sub>2</sub> monolayer [15], constructing SnO<sub>2</sub>/Sb<sub>2</sub>Se<sub>3</sub> heterojunctions [16], and using a 20 nm Sb<sub>2</sub>S<sub>3</sub> seed layer to assist the vertical growth of Sb<sub>2</sub>Se<sub>3</sub> grains [17] have been explored.

However, achieving a Sb<sub>2</sub>Se<sub>3</sub> thin film with highly oriented grains along the preferred directions, closely aligning the *c*-axis, often results in

<sup>\*</sup> Corresponding author.

E-mail address: [meuslu@taltech.ee](mailto:meuslu@taltech.ee) (M.E. Uslu).

<https://doi.org/10.1016/j.mssp.2024.108835>

Received 13 June 2024; Received in revised form 19 July 2024; Accepted 19 August 2024

Available online 22 August 2024

1369-8001/© 2024 Elsevier Ltd. All rights are reserved, including those for text and data mining, AI training, and similar technologies.

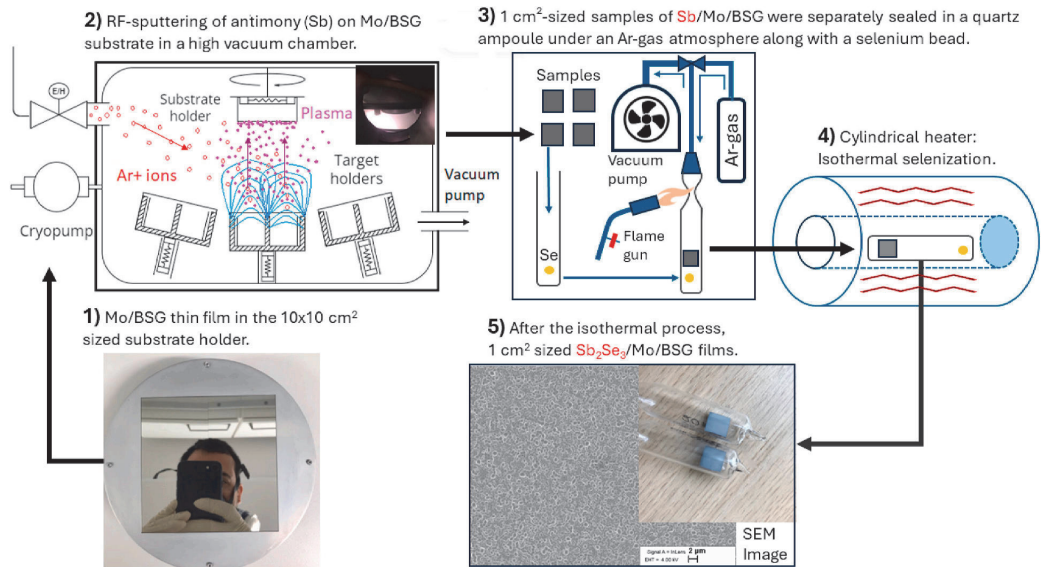


Fig. 1. Technological route developed in this study for the preparation of Sb<sub>2</sub>Se<sub>3</sub> thin films.

a particularly irregular morphology, with deep grain boundaries and even micro-voids on the surface. This inhomogeneous morphology poses a challenge in building Sb<sub>2</sub>Se<sub>3</sub>-based thin film solar cells, as these micro-voids can act as shunts, suppressing the photocurrent. Therefore, this study focuses on developing a more controllable and easier method for fabricating optimal Sb<sub>2</sub>Se<sub>3</sub> thin films with highly oriented grains along the *c*-axis and compact morphology suitable for solar cell applications.

## 2. Experimental

In this study, molybdenum (Mo) and antimony (Sb) thin films were deposited using an Angstrom Engineering Evovac 030 magnetron sputtering system equipped with three sputtering sources with glow discharge. Mo and Sb targets with 99.99 % purity from Testbourne Inc. were used. At first, a 1.2 μm thick Mo thin film was sputtered onto borosilicate glass (BSG) using a DC power of 200 W, a substrate temperature of 300 °C and an ionized argon (Ar<sup>+</sup> gas) pressure of  $5 \times 10^{-3}$  Torr in a chamber. After reference deposition of Mo, the sheet resistance of  $10 \times 10$  cm<sup>2</sup> Mo/BSG thin film was measured to be only a few ohms over

the entire surface. The Sb sputtering process was run continuously under high vacuum without removing the Mo/BSG substrate from the vacuum chamber of the magnetron sputtering system, after the substrate temperature had been cooled to room temperature (RT) for one day. Sb was sputtered with an RF power of 60 W onto Mo/BSG substrate ( $10 \times 10$  cm<sup>2</sup>) at RT, an Ar<sup>+</sup> gas flow of 20 sccm and pressure of  $5 \times 10^{-6}$  Torr. Then the 10 cm<sup>2</sup> Sb/Mo/BSG thin film was removed from the deposition chamber and cut into 1 cm<sup>2</sup> pieces, which underwent the selenization process in sealed quartz ampoules at different temperatures. For the selenization process, the Sb/Mo/BSG thin films were placed into 8 cm-long quartz ampoules together with the elemental selenium (Se) beads of 5N purity from Alfa Aesar. The quartz ampoules were then degassed and filled with argon gas at different pressures at RT before being sealed. The described technological route is illustrated in Fig. 1. A cylindrical furnace was used for the isothermal selenization process to ensure heat uniformity on the thin film samples. The distance between a Se-bead and a Sb/Mo/BSG thin film inside an ampoule was maintained at 7 cm, identical for all the samples. The samples in the closed ampoules were placed individually in the furnace preheated to a target temperature.

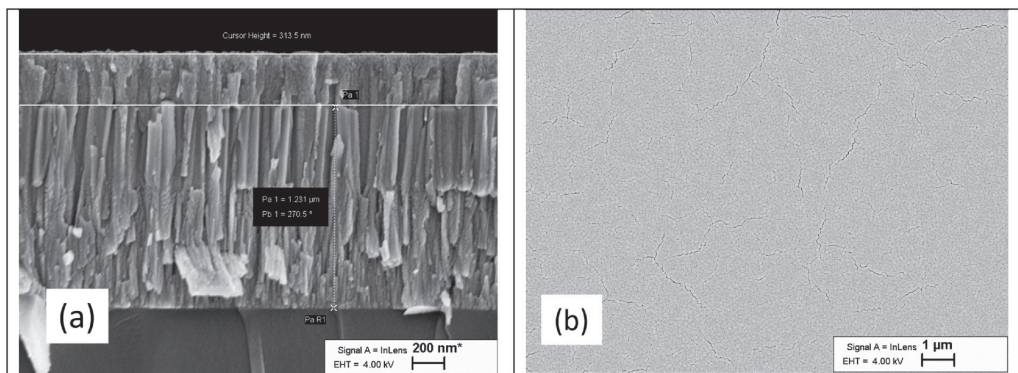


Fig. 2. SEM images of (a) cross section and (b) top-view of sputtered Sb film on Mo/BSG.

**Table 1**  
Selenization process parameters of Sb/Mo/BSG thin films.

Sample name	Selenization temperature, °C	Ar pressure at RT, Torr
SbSe_380-200	380	200
SbSe_380-300	380	300
SbSe_400-200	400	200
SbSe_400-300	400	300

The selenization time was kept constant at 30 min, while the selenization temperature and argon gas pressure were varied. After the 30 min of selenization, the ampoules with the samples were taken out of the furnace and allowed to cool naturally to room temperature.

The elemental compositions of the synthesized thin films were determined by energy-dispersive X-ray spectroscopy (EDS) using a Bruker Esprit 1.8 system on a Zeiss Merlin high-resolution scanning electron microscope (SEM). The phase composition of Sb<sub>2</sub>Se<sub>3</sub> thin films was studied by using room-temperature (RT) micro-Raman spectroscopy with Horiba's LabRam HR800 spectrometer, employing a 532 nm laser line, 0.42 mW power, and a laser spot size of 10 μm in diameter. The Raman analysis was complemented by the powder X-ray diffraction (XRD) analysis using a Rigaku Ultima IV diffractometer operating with the silicon strip detector D/teX Ultra.

To test the developed Sb<sub>2</sub>Se<sub>3</sub> thin films in a solar cell device, a pulsed laser deposition (PLD) system by Neocera equipped with a COMPex laser with λ = 248 nm was employed to deposit a 50 nm cadmium sulfide (CdS) buffer layer on top of the Sb<sub>2</sub>Se<sub>3</sub>/Mo/BSG thin films at a substrate temperature of 200 °C, deposition pressure of 2 × 10<sup>-3</sup> Torr, using 3000 pulses at 10 Hz, and with 200 mJ energy of each pulse. To complete the solar cell devices, 350 nm Al:ZnO was deposited on top of the CdS by radio frequency magnetron sputtering. To measure the I–V curves and determine the energy conversion efficiency of Al:ZnO/CdS/Sb<sub>2</sub>Se<sub>3</sub>/Mo/BSG solar cells, a Keithley 2400 source meter under standard test conditions (AM1.5, 100 mW/cm<sup>2</sup>) using a Newport Oriol Class A 91195A solar simulator were used. The measurements of the external quantum efficiency (EQE) spectra were performed on a commercial EQE measurement system from Scientech Inc.

### 3. Results and discussion

The RF-sputtered Sb film on the Mo/BSG substrate had a thickness of approximately 315 nm, as determined from the cross-section SEM image shown in Fig. 2a. The uniform surface morphology of the Sb film can be seen in Fig. 2b. These Sb films were subsequently selenized at different temperatures ranging from 380 °C to 420 °C, using different Ar-pressures ranging from 200 to 300 Torr to obtain Sb<sub>2</sub>Se<sub>3</sub> thin films. The optimal selenization temperature was found to be between 380 °C–400 °C.

A higher selenization temperature of 420 °C may result in better vertical growth with the preferred orientation, as J. Tang et al. [13] also suggests that the preferred grain orientations (221), (211), and (001) of Sb<sub>2</sub>Se<sub>3</sub> to the substrate's surface require higher surface energies (J/m<sup>2</sup>) than other non-preferred ones. However, the enhanced vertical growth of Sb<sub>2</sub>Se<sub>3</sub> grains at higher selenization temperature can disturb the surface compactness, potentially leading to shunt paths in a Sb<sub>2</sub>Se<sub>3</sub>/CdS-based thin film solar cell, as can be seen from the SEM image in Fig. 1S. Therefore, finding an optimal balance between grain orientation and surface compactness is crucial. In the following, four samples were chosen based on the uniformity and repeatability of the Sb<sub>2</sub>Se<sub>3</sub> films for further study. The selected Sb/Mo/BSG thin films were selenized at 380 °C and 400 °C for 30 min, accompanied by two different Ar-pressures. The samples labelled as SbSe\_380-200, SbSe\_400-200, SbSe\_380-300, SbSe\_400-300 are described in Table 1.

It was found that selenization of Sb/Mo/BSG films without the presence of any inert gas, such as argon, leads to elemental Se reacting very aggressively with Sb in the selenization temperature range used in

**Table 2**  
Elemental compositions and the thickness of the Sb<sub>2</sub>Se<sub>3</sub> film in the studied Sb<sub>2</sub>Se<sub>3</sub> thin-film samples determined by EDS.

	Antimony at. %	Selenium at. %	Thickness, nm
SbSe_380-200	37.5 ± 1.1	62.5 ± 1.2	640
SbSe_380-300	41.5 ± 1.3	58.5 ± 1.3	660
SbSe_400-200	40.6 ± 1.1	59.4 ± 1.1	1310
SbSe_400-300	38.1 ± 1.0	61.9 ± 1.1	870

this study. This results in severe surface degradation and detachment of the Sb<sub>2</sub>Se<sub>3</sub> layer from the Mo/BSG substrates an example is shown in Fig. 2S. With the reference to Table 1, when 200 Torr and 300 Torr of Ar-pressures are filled into 25 ml quartz ampoules at RT, the pressure at 380 °C should reach approximately 440 Torr and 660 Torr, respectively. At 400 °C, the pressure should be around 453 Torr and 675 Torr, respectively, assuming the ideal gas behavior in an isolated system. On the other hand, the Se vapor pressure originating from elemental Se-bead at 380 °C and 400 °C is lower than the partial Ar-pressure at the same temperatures. This is because the boiling point of Se at 1 atm (760 Torr) is approx. 685 °C [18]. It is expected that the difference between partial pressures of Se vapor and Ar gas inside the quartz ampoule will influence the Se–Sb reaction rate on the Mo/BSG substrate and the Se saturation in the Sb<sub>2</sub>Se<sub>3</sub> thin film. Therefore, the elemental composition of the studied Sb<sub>2</sub>Se<sub>3</sub> thin films was determined by EDS analysis and is shown in Table 2. Although the difference in the Se/Sb ratio among the studied samples remains close to the margin of EDS measurement error, the extreme samples SbSe\_380-200 and SbSe\_400-300 exhibit slightly more Se-rich compositions.

Figs. 3 and 4 show the top view and cross-sectional SEM images of Sb<sub>2</sub>Se<sub>3</sub> thin films prepared by varying the selenization temperature and Ar-pressure. All studied samples have columnar and highly crystallized grain structures. Namely, the samples SbSe\_400-200 (Fig. 4a–c) and SbSe\_400-300 (Fig. 4b–d), selenized at higher temperature of 400 °C, exhibit irregular morphology with micro-voids in the Sb<sub>2</sub>Se<sub>3</sub> film. However, these films also feature longer columnar grains with the lengths up to 2 μm and width of up to 700 nm. On the other hand, a lower selenization temperature of 380 °C for the samples SbSe\_380-200 (Fig. 3a–c) and SbSe\_380-300 (Fig. 3b–d) resulted in more densely packed grains. The isothermally selenized samples, which were prepared using lower Ar-pressure of 200 Torr, SbSe\_380-200 and SbSe\_400-200, showed narrower columnar grains with widths up to 570 nm.

The compactness and thickness of the Sb<sub>2</sub>Se<sub>3</sub> films are influenced by selenization temperature and the applied Ar-pressure. The film thickness is found to be largest for the SbSe\_400-200 sample, with a thickness of 1310 nm, as detected from the cross-sectional SEM image shown in Fig. 4c. Samples SbSe\_380-200, SbSe\_380-300, and SbSe\_400-300 have thicknesses of 640 nm, 660 nm, and 870 nm, respectively. It can be concluded that the change in the selenization temperature has a greater influence on the surface morphology than partial Ar-pressure. Achieving uniform and compact Sb<sub>2</sub>Se<sub>3</sub> thin films is more challenging at selenization at temperatures higher than 380 °C. The irregular surface morphology with large micro-voids in SbSe\_400-200 and SbSe\_400-300 is a significant drawback for Sb<sub>2</sub>Se<sub>3</sub>-based thin-film solar cell applications. Therefore, the samples with more compact morphology, SbSe\_380-200 and SbSe\_380-300, were chosen for further analysis in this study.

The room temperature micro-Raman spectra, measured by scanning multiple spots on the surfaces of the samples, were found to be identical across the surface of each sample. The resolved Raman spectra of SbSe\_380-200 and SbSe\_380-300, with Lorentzian peaks used for the fitting shown in Fig. 5, indicate that the crystallinity of both samples is satisfactory. This conclusion is based on the narrow full width at half maximum (FWHM) values of the main Raman shift ( $A_g^2$ ) at 191 cm<sup>-1</sup>, as demonstrated by the comparison between amorphous and crystalline thin films of Sb<sub>2</sub>Se<sub>3</sub> shown by O. L. Muskens et al. [19]. Angle-resolved

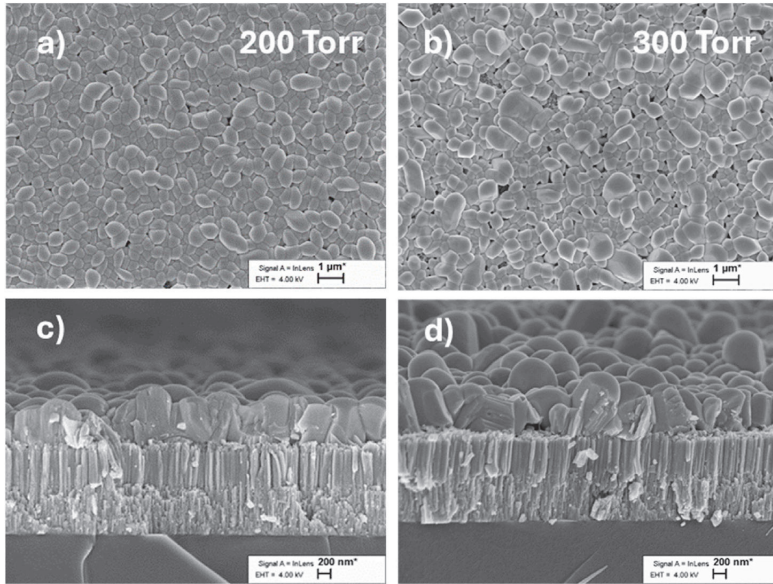


Fig. 3. SEM images of surface (a, b) and corresponding cross-sections (c, d) of  $\text{Sb}_2\text{Se}_3$  thin film selenized at  $380^\circ\text{C}$  under different Ar-pressure.

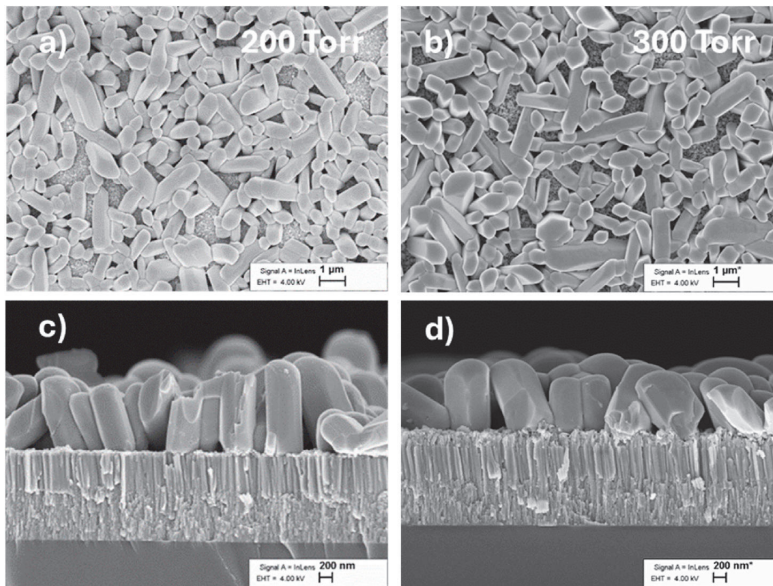


Fig. 4. SEM images of surface (a, b) and corresponding cross-sections (c, d) of  $\text{Sb}_2\text{Se}_3$  thin film selenized at  $400^\circ\text{C}$  under different Ar-pressure.

and polarized Raman spectra of  $\text{Sb}_2\text{Se}_3$  studied by F. Jäckel et al. [20], suggested that the relative decrease in the intensity of the  $B_{2g}^1$  peak at  $155\text{ cm}^{-1}$  and, at the same time, a relative enhancement of the intensity of the  $B_{2g}^2$  peak at  $205\text{ cm}^{-1}$  [21], are linked to the preferred grain orientation of  $\text{Sb}_2\text{Se}_3$  in the (001) direction. The study of F. Jäckel et al. [20] also showed that it is possible to detect the grain orientation of (001) from the XRD analysis by using its equivalent counterpart indexed with (002) [22]. However, to gather more information about the

crystallinity of the  $\text{SbSe}_{380-200}$  and  $\text{SbSe}_{380-300}$  samples, the XRD analysis was performed using ICDD 00-015-0861 card in the Rietveld analysis for  $\text{Sb}_2\text{Se}_3$ , as shown in Fig. 6a. No secondary phases were detected, confirming by EDS, Raman, and XRD analysis that the studied thin film samples consist only of orthorhombic  $\text{Sb}_2\text{Se}_3$ . As seen in Fig. 6a, the relative XRD peak intensity of (002) along the  $c$ -axis dominates in both samples. The XRD peaks of (hk1), (0k1), and particularly (002) are representative of vertically oriented  $\text{Sb}_2\text{Se}_3$  grains, as reported in the literature [20,22–24]. To comprehend better the relative XRD

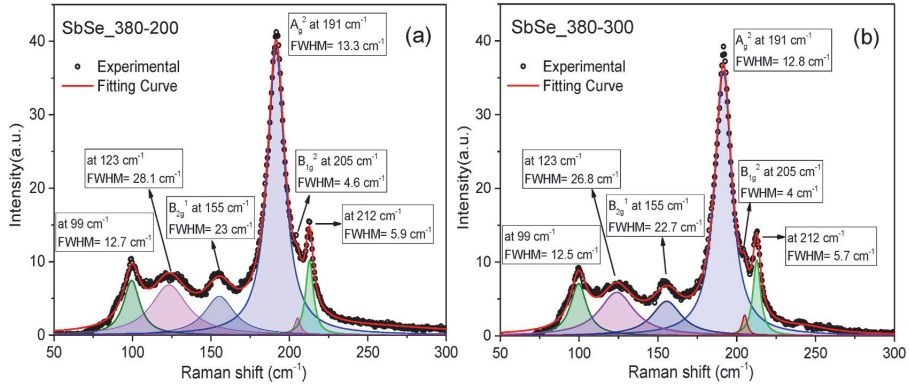


Fig. 5. The resolved Raman spectra of (a)  $Sb_2Se_3/Mo/BSG$  thin-film synthesized at 380 °C under Ar-pressure 200 Torr-Ar at RT, (b)  $Sb_2Se_3/Mo/BSG$  thin-film synthesized at 380 °C under Ar-pressure 300 Torr-Ar at RT.

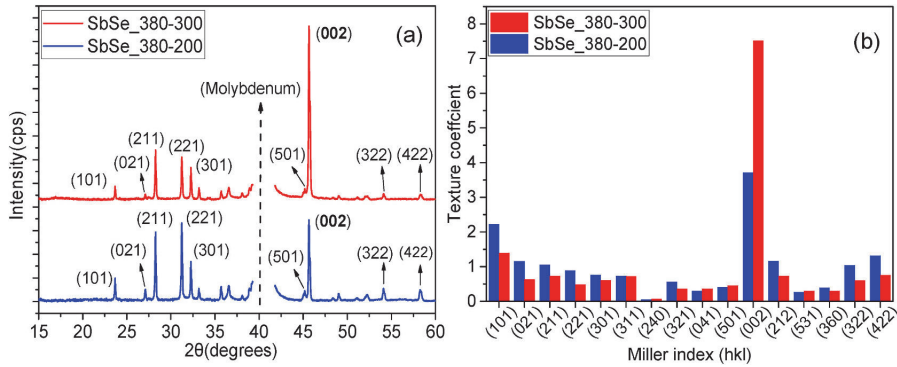


Fig. 6. (a) XRD pattern of  $SbSe_{380-200}$  with blue, and  $SbSe_{380-300}$  with red. (b) XRD texture coefficients (TC) for sample  $SbSe_{380-200}$  (blue), and  $SbSe_{380-300}$  (red).

intensities, the texture coefficients (TC) of sixteen XRD peaks in Fig. 6b were calculated using the following equation [22]:

$$TC_{hkl} = \frac{I(hkl)}{I_0(hkl)} \bigg/ \left( \frac{1}{N} \sum_{i=1}^N \frac{I_i(hkl)}{I_0(hkl)} \right),$$

Where (hkl) indicates a miller index for a particular crystallite orientation, N is total number of all XRD peaks resolved in the Rietveld analysis,  $I_0(hkl)$  are standard intensities (a.u.) from the reference ICDD 00-015-0861 card, and  $I(hkl)$  are their corresponding intensities from the XRD measurement on  $Sb_2Se_3$  thin films samples in this study. As a result, the sum of those preferred TC indexed (101), (021), (211), (221), (002), based on the sixteen XRD peaks ( $N = 16$ ), is 9 for  $SbSe_{380-200}$ , and 10.2 for  $SbSe_{380-300}$ . Therefore, as shown in Fig. 6b, the texture coefficients of the preferred orientations cumulatively dominate the XRD spectra by 56 % and 63 % for  $SbSe_{380-200}$  and  $SbSe_{380-300}$ , respectively. The results of the XRD analysis complement the observations made from the SEM images in Fig. 3, confirming the enhanced grain orientations aligning with the c-axis of the  $Sb_2Se_3/Mo/BSG$  thin films. Unexpectedly, the texture coefficient in Fig. 6b shows that the sample selenized at higher Ar-pressure,  $SbSe_{380-300}$ , has grain orientation (002) enhanced stronger and it exhibits relatively larger grains as observed on the SEM images in Fig. 3. Nevertheless, some micro-voids located distinctly on the surfaces of  $SbSe_{380-200}$  and  $SbSe_{380-300}$  thin films were still observed on the SEM images. This

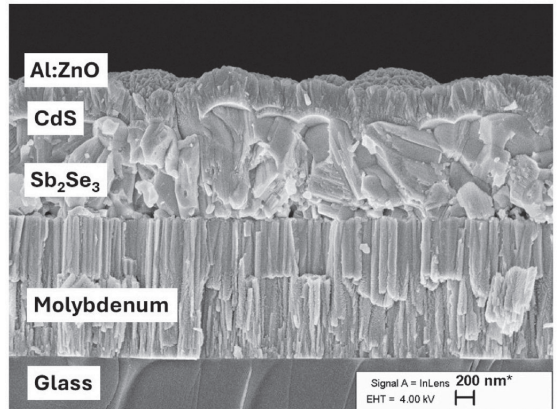


Fig. 7. Cross-section SEM image of a Al:ZnO/CdS/ $Sb_2Se_3/Mo/BSG$  solar cell based on  $SbSe_{380-300}$  thin film.

challenge arises from the high anisotropy of  $Sb_2Se_3$  crystallites. It can be concluded that thicker RF-sputtered Sb and a lower selenization temperature of 380 °C can further enhance the surface compactness of

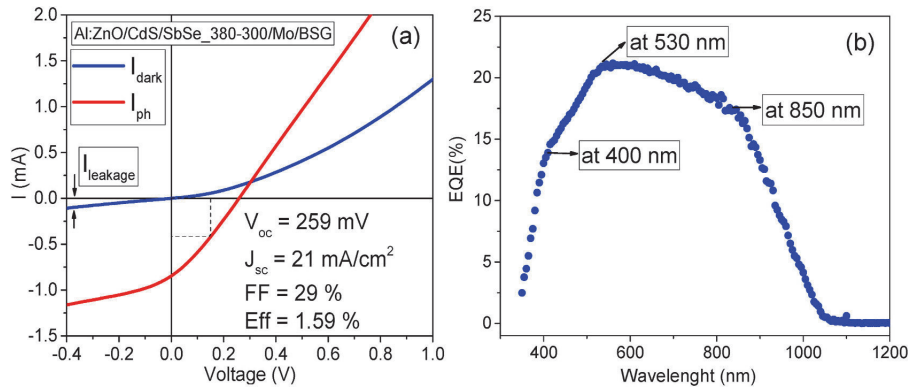


Fig. 8. (a) I–V curve of the solar cell based on Sb<sub>2</sub>Se<sub>3</sub>\_380-300 thin film, (b) its EQE spectrum.

#### Sb<sub>2</sub>Se<sub>3</sub> thin films.

To test the Sb<sub>2</sub>Se<sub>3</sub> thin film with enhanced grain orientation in a solar cell device, a complete solar cell structure of Al:ZnO/CdS/Sb<sub>2</sub>Se<sub>3</sub>/Mo/BSG was fabricated as described in the experimental details of the manuscript. The cross-sectional SEM image of a complete device is presented in Fig. 7.

The I–V curve of the solar cell shown in Fig. 8a reveals a reverse leakage current of 0.1 mA and exhibits high serial resistance. The reverse leakage current observed in the I–V curve may be attributed to micro-voids on the surface of the Sb<sub>2</sub>Se<sub>3</sub> thin film. The EQE spectra of the solar cell shown in Fig. 8b exhibits a reduced response in the wavelength range between 400 nm and 530 nm, as well as a diminished red response at wavelengths longer than 850 nm. The EQE reduction between 400 nm and 530 nm may be due to the recombination of photo-generated electron-hole pairs (EHPs) in the CdS/Sb<sub>2</sub>Se<sub>3</sub> junction area. Moreover, the reduced red response in the EQE suggests recombination of EHPs at the Sb<sub>2</sub>Se<sub>3</sub>/Mo back contact interface. This implies the need for a suitable hole transport layer in Sb<sub>2</sub>Se<sub>3</sub>/CdS-based solar cells [25]. Optimization of the complete thin film solar cell structure was not the focus of this study. However, a decent photocurrent density of 21 mA/cm<sup>2</sup> was achieved using SbSe\_380-300 with improved grain orientation as an absorber. This confirms the importance of the grain orientation for enhancing current production in the Sb<sub>2</sub>Se<sub>3</sub> based solar cells.

Other Sb<sub>2</sub>Se<sub>3</sub> absorbers thin films developed in this study resulted in shunted devices and are therefore not presented here.

#### 4. Conclusion

The desired grain orientation along the *c*-axis in Sb<sub>2</sub>Se<sub>3</sub>/Mo/BSG thin films was successfully achieved using magnetron sputtering method combined with post-deposition isothermal selenization technique, as confirmed by the texture coefficient and SEM analysis. A balance between the preferred grain orientation and the surface compactness of the thin films was found to be crucial for their use in thin film solar cell applications. It was observed that enhanced grain orientations closely aligning with the *c*-axis (indexed (101), (021), (211), (221), (002)) by 63 % in the Sb<sub>2</sub>Se<sub>3</sub> thin film, selenized at 380 °C after being placed in a 300 Torr of Ar-pressure environment at RT, were achieved without compromising the surface compactness of the film. However, further optimization is still necessary to eliminate all possible micro-voids on the Sb<sub>2</sub>Se<sub>3</sub> thin film surface. Additionally, the developed method could pave the way for the fabrication of other quasi-1D chalcogenide thin films.

#### CRedit authorship contribution statement

**Mehmet Ender Uslu:** Writing – review & editing, Writing – original draft, Visualization, Validation, Methodology, Investigation, Formal analysis, Data curation, Conceptualization. **Katri Muska:** Methodology, Investigation. **Maris Pilvet:** Methodology. **Sergei Bereznev:** Methodology. **Valdek Mikli:** Investigation, Data curation. **Marit Kauk-Kuusik:** Writing – review & editing, Validation, Software, Resources. **Maarja Grossberg-Kuusk:** Writing – review & editing, Validation, Resources, Project administration, Funding acquisition.

#### Declaration of competing interest

The authors declare that they have no known competing financial interests or personal relationships that could have appeared to influence the work reported in this paper. Maarja Grossberg-Kuusk reports financial support was provided by Estonian Research Council. If there are other authors, they declare that they have no known competing financial interests or personal relationships that could have appeared to influence the work reported in this paper.

#### Data availability

Data will be made available on request.

#### Acknowledgements

This work was supported by the Estonian Research Council [grant number PRG1023]; M-ERA.net project LightCell [grant number MNHA23040]; and GREENTECH Project [grant number TK210].

#### Appendix A. Supplementary data

Supplementary data to this article can be found online at <https://doi.org/10.1016/j.mssp.2024.108835>.

#### References

- [1] H. Maghraoui-Meherzi, T. Ben Nasr, M. Dachraoui, Synthesis, structure and optical properties of Sb<sub>2</sub>Se<sub>3</sub>, Mater. Sci. Semicond. Process. 16 (2013) 179–184, <https://doi.org/10.1016/j.mssp.2012.04.019>.
- [2] Xinsheng Liu, Jie Chen, Luo Miao, Meiyong Leng, Zhe Xia, Ying Zhou, Sikai Qin, Ding-Jiang Xue, Lv Lu, Han Huang, Dongmei Niu, Jiang Tang, Thermal evaporation and characterization of Sb<sub>2</sub>Se<sub>3</sub> thin film for substrate Sb<sub>2</sub>Se<sub>3</sub>/CdS solar cells, ACS Appl. Mater. Interfaces 6 (2014) 10687–10695, <https://doi.org/10.1021/am502427s>.
- [3] Mehmet Ender Uslu, Mati Danilson, Kristi Timmo, Maarja Grossberg-Kuusk, The effect of tin doping on the band structure and optical properties of polycrystalline

- antimony selenide, *Phys. B Condens. Matter* 678 (2024) 415744, <https://doi.org/10.1016/j.physb.2024.415744>.
- [4] Jea Woong Job, Taifeng Ju, Bonkee Koo, Jea Woong Jo, Min Jae Ko, Enhanced photovoltaic performance of solution-processed  $\text{Sb}_2\text{Se}_3$  thin film solar cells by optimizing device structure, *Curr. Appl. Phys.* 20 (2020) 282–287, <https://doi.org/10.1016/j.cap.2019.11.018>.
- [5] Jianmin Li, Yuqi Zhao, Shaoying Wang, Chuang Li, Bo Che, Xueling Chen, Hongyi Chen, Rongfeng Tang, Xiaomin Wang, Guilin Chen, Ti Wang, Junbo Gong, Tao Chen, Xudong Xiao, Jianmin Li, Regulating deposition kinetics via a novel additive-assisted chemical bath deposition technology enables fabrication of 10.57%-efficiency  $\text{Sb}_2\text{Se}_3$  solar cells, *Energy Environ. Sci.* 15 (2022) 5118–5128, <https://doi.org/10.1039/d2ee02261c>.
- [6] Zhaoteng Duan, Xiaoyang Liang, Feng Yang, Haiya Ma, Baolai Liang, Ying Wang, Shiping Luo, Shufang Wang, Ruud E.I. Schropp, Yaohua Mai, Zhiqiang Li,  $\text{Sb}_2\text{Se}_3$  thin-film solar cells exceeding 10% power conversion efficiency enabled by injection vapor deposition technology, *Adv. Mater.* 34 (2022) 2202969, <https://doi.org/10.1002/adma.202202969>.
- [7] Menglin Huang, Peng Xu, Dan Han, Jiang Tang, Shiyou Chen, Complicated and unconventional defect properties of the quasi-one-dimensional photovoltaic semiconductor  $\text{Sb}_2\text{Se}_3$ , *ACS Appl. Mater. Interfaces* 11 (2019) 15564–15572, <https://doi.org/10.1021/acsami.9b01220>.
- [8] Christopher N. Savory, David O. Scanlon, The complex defect chemistry of antimony selenide, *J. Mater. Chem. A* 7 (2019) 10739, <https://doi.org/10.1039/C9TA02022E>.
- [9] M. Grossberg, O. Volobujeva, A. Penezko, R. Kaupmees, T. Raadik, J. Krustok, *J. Alloys Compd.* 817 (2020) 152716, <https://doi.org/10.1016/j.jallcom.2019.152716>.
- [10] Xinwei Wang, Sean R. Kavanagh, David O. Scanlon, Aron Walsh, Four-electron negative- $U$  vacancy defects in antimony selenide, *Phys. Rev. B* 108 (2023) 134102, <https://doi.org/10.1103/PhysRevB.108.134102>.
- [11] Chao Chen, David C. Bobela, Ye Yang, Shuaicheng Lu, Kai Zheng, Cong Ge, Bo Yang, Liang Gao, Zhao Yang, Matthew C. Beard, Jiang Tang, Characterization of basic physical properties of  $\text{Sb}_2\text{Se}_3$  and its relevance for photovoltaics, *Front. Optoelectron.* 10 (1) (2017) 18–30, <https://doi.org/10.1007/s12200-017-0702-z>.
- [12] Zhiqiang Li, Xiaoyang Liang, Gang Li, Haixu Liu, Huiyu Zhang, Jianxin Guo, Jingwei Chen, Kai Shen, Xingyuan San, Wei Yu, Ruud E.I. Schropp, Yaohua Mai, 9.2%-efficient core-shell structured antimony selenide nanorod array solar cells, *Nat. Commun.* 10 (2019) 125, <https://doi.org/10.1038/s41467-018-07903-6>.
- [13] Ying Zhou, Liang Wang, Shiyou Chen, Sikai Qin, Xinsheng Liu, Jie Chen, Ding-Jiang Xue, Luo Miao, Yuanzhi Cao, Yibing Cheng, Edward H. Sargent, Jiang Tang, Thin-film  $\text{Sb}_2\text{Se}_3$  photovoltaics with oriented one-dimensional ribbons and benign grain boundaries, *Nat. Photonics* 9 (2015) 409–415, <https://doi.org/10.1038/nphoton.2015.78>.
- [14] Si-Nae Park, Se-Yun Kim, Sang-Ju Lee, Shi-Joon Sung, Kee-Jeong Yang, Jin-Kyu Kang, Dae-Hwan Kim, Facile growth of a  $\text{Sb}_2\text{Se}_3$  nanorod array induced by a  $\text{MoSe}_2$  interlayer and its application in 3D p-n junction solar cells, *Mater. Adv.* 3 (2022) 978–985, <https://doi.org/10.1039/D1MA00804H>.
- [15] Guangzhuang Sun, Bo Li, Li Jia, Zhengwei Zhang, Huifang Ma, Peng Chen, Zhao Bei, Ruixia Wu, WeiQi Dang, Xiangdong Yang, Xuwan Tang, Dai Chen, Ziwai Huang, Yuan Liu, Xidong Duan, Xiangfeng Duan, Direct van der Waals epitaxial growth of 1D/2D  $\text{Sb}_2\text{Se}_3/\text{WS}_2$  mixed-dimensional p-n heterojunctions, *Nano Res.* 12 (5) (2019) 1139–1145, <https://doi.org/10.1007/s12274-019-2364-1>.
- [16] Jing Zhou, Dan Meng, Tinghe Yang, Xintong Zhang, Zheqing Tang, Yu Cao, Jian Ni, Jianjun Zhang, Ziyang Hu, Jinbo Pang, Enhanced charge carrier transport via efficient grain conduction mode for  $\text{Sb}_2\text{Se}_3$  solar cell applications, *Appl. Surf. Sci.* 591 (2022) 153169, <https://doi.org/10.1016/j.apsusc.2022.153169>.
- [17] Al Amin, Dian Li, Xiaomeng Duan, S.N. Vijayaraghavan, Harigovind G. Menon, Wall Jacob, Mark Weaver, Mark Ming-Cheng Cheng, Yufeng Zheng, Li Lin, Feng Ya, Enhanced efficiency and stability in  $\text{Sb}_2\text{S}_3$  seed layer buffered  $\text{Sb}_2\text{Se}_3$  solar cells, *Adv. Mater. Interfaces* 9 (2022) 2200547, <https://doi.org/10.1002/admi.202200547>.
- [18] E.H. Baker, The vapour pressure and resistivity of selenium at high temperatures, *J. Chem. Soc. A* (1968) 1089–1092, <https://doi.org/10.1039/J19680001089>.
- [19] Matthew Delaney, Ioannis Zeimpekis, Daniel Lawson, Daniel W. Hewak, Otto L. Muskens, A new family of ultralow loss reversible phase-change materials for photonic integrated circuits:  $\text{Sb}_2\text{S}_3$  and  $\text{Sb}_2\text{Se}_3$ , *Adv. Funct. Mater.* 30 (2020) 2002447, <https://doi.org/10.1002/adfm.202002447>.
- [20] Nicole Fleck, Theodore D.C. Hobson, Christopher N. Savory, John Buckeridge, Tim D. Veal, Maria R. Correia, David O. Scanlon, Ken Durose, Frank Jackel, Identifying Raman modes of  $\text{Sb}_2\text{Se}_3$  and their symmetries using angle-resolved polarised Raman spectra, *J. Mater. Chem. A* 8 (2020) 8337, <https://doi.org/10.1039/D0TA01783C>.
- [21] Pedro Vidal-Fuentes, Maxim Guc, Xavier Alcobe, Tariq Jawhari, Marcel Placidi, Alejandro Pérez-Rodríguez, Edgardo Saucedo, Victor Izquierdo Roca, Multiwavelength excitation Raman scattering study of  $\text{Sb}_2\text{Se}_3$  compound: fundamental vibrational properties and secondary phases detection, *2D Mater.* 6 (2019) 045054, <https://doi.org/10.1088/2053-1583/ab4029>.
- [22] F. Pattini, S. Rampino, F. Mezzadri, D. Calestani, G. Spaggiari, M. Sidoli, D. Delmonte, A. Sala, E. Gilioli, M. Mazzer, Role of the substrates in the ribbon orientation of  $\text{Sb}_2\text{Se}_3$  films grown by Low-Temperature Pulsed Electron Deposition, *Sol. Energy Mater. Sol. Cells* 218 (2020) 110724, <https://doi.org/10.1016/j.solmat.2020.110724>.
- [23] R. Krautmann, N. Spalatu, R. Gunder, D. Abou-Ras, T. Unold, S. Schorr, M. Krunks, I. Oja Acik, Analysis of grain orientation and defects in  $\text{Sb}_2\text{Se}_3$  solar cells fabricated by close-spaced sublimation, *Sol. Energy* 225 (2021) 494–500, <https://doi.org/10.1016/j.solener.2021.07.022>.
- [24] Jimin Kim, Woosook Yang, Yunjung Oh, Hyungsoo Lee, Seonhee Lee, Hyunjung Shin, Joosun Kim, Jooho Moon, Analysis of grain orientation and defects in  $\text{Sb}_2\text{Se}_3$  solar cells fabricated by close-spaced sublimation, *J. Mater. Chem. A* 5 (2017) 2180–2187, <https://doi.org/10.1039/C6TA09602F>.
- [25] Roberto Jakomin, Stefano Rampino, Giulia Spaggiari, Michele Casappa, Giovanna Trevisi, Elena Del Canale, Enos Gombia, Matteo Bronzoni, Kodjo Kekeli Sossue, Francesco Mezzadri, Francesco Pattini, Cu-doped  $\text{Sb}_2\text{Se}_3$  thin-film solar cells based on hybrid pulsed electron deposition/radio frequency magnetron sputtering growth techniques, *Solar* 4 (2024) 83–98, <https://doi.org/10.3390/solar4010004>.

# Curriculum vitae

## Personal data

Name: Mehmet Ender Uslu  
Date of birth: 18.07.1984  
Place of birth: Türkiye  
Citizenship: Turkish

## Contact data

E-mail: meuslu@taltech.ee

## Education

2019–2024 Tallinn University of Technology, PhD  
2017–2019 Tallinn University of Technology, Materials and processes for sustainable Energetics (cum laude), MSc  
2008–2014 Polytechnic University of Milan, Electronic engineering, BSc  
1998–2001 Tavşanlı Teknik ve Endüstri Meslek Lisesi, High school

## Language competence

Turkish Native  
English Proficient  
Italian Proficient

## Participation in conferences

2023 European Materials Research Society (EMRS) Spring Meeting 2023, Strasbourg, France. Poster presentation.  
2022 The Latsis Symposium on Earth-Abundant Materials for Future Photovoltaics, Lausanne, Switzerland. Poster presentation.  
2019–2021 Graduate School of Functional Materials and Technologies (GSFMT), Tallinn University of Technology and Tartu University, Estonia. Oral and poster presentations.

## Professional employment

2019–2024 Laboratory of Photovoltaic Materials, Tallinn University of Technology, early-stage researcher  
2015–2016 Alstom transport, engineer  
2014–2015 Enel enerji elektronik A.Ş., engineer

## List of Publications

1. Enhanced grain orientation in  $\text{Sb}_2\text{Se}_3$  thin films deposited on Mo/BSG substrates via RF-sputtering and selenization, *Materials Science in Semiconductor Processing* 184 (2024) 108835. <https://doi.org/10.1016/j.mssp.2024.108835>
2. The Effect of Tin Doping on the Band Structure and Optical Properties of Polycrystalline Antimony Selenide, *Physica B: Condensed Matter* 678 (2024) 415744. <https://doi.org/10.1016/j.physb.2024.415744>
3. Study of the Optical Properties of  $\text{Sb}_2(\text{Se}_{1-x}\text{S}_x)_3$  ( $x = 0-1$ ) Solid Solutions. *Materials Science in Semiconductor Processing* 144 (2022) 106571. <https://doi.org/10.1016/j.mssp.2022.106571>

# Elulookirjeldus

## Isikuandmed

Nimi: Mehmet Ender Uslu  
Sünniaeg: 18.07.1984  
Sünnikoht: Türgi  
Kodakondsus: Türgi

## Kontaktandmed

E-post: meuslu@taltech.ee

## Hariduskäik

2019–2024 Tallinna Tehnikaülikool, PhD  
2017–2019 Tallinna Tehnikaülikool, Materjalid ja protsessid jätkusuutlikus  
energeetikas (cum laude), MSc  
2008–2014 Polytechnic University of Milan, Elektroonika, BSc  
1998–2001 Tavşanlı Teknik ve Endüstri Meslek Lisesi, keskkharidus

## Keelteoskus

Türgi keel Emakeel  
Inglise keel Kõrgtase  
Itaalia keel Kõrgtase

## Osalemine konverentsidel

2023 European Materials Research Society (EMRS) Spring Meeting 2023,  
Strasbourg, Prantsusmaa. Posterettekanne.  
2022 The Latsis Symposium on Earth-Abundant Materials for Future  
Photovoltaics, Lausanne, Šveits. Posterettekanne.  
2019-2021 Funktsionaalsete materjalide ja tehnoloogiate doktorikool  
(GSFMT), Tallinna Tehnikaülikool ja Tartu ülikool, Eesti. Suulised ja  
posterettekanded.

## Teenistuskäik

2019–2024 Päikeseenergeetika materjalide teaduslabor, Tallinna  
Tehnikaülikool, doktorant-nooremteadur  
2015–2016 Alstom transport, insener  
2014–2015 Enel energi elektronik A.Ş., insener

## Publikatsioonid

- Enhanced grain orientation in  $\text{Sb}_2\text{Se}_3$  thin films deposited on Mo/BSG substrates via RF-sputtering and selenization, *Materials Science in Semiconductor Processing* 184 (2024) 108835. <https://doi.org/10.1016/j.mssp.2024.108835>
- The Effect of Tin Doping on the Band Structure and Optical Properties of Polycrystalline Antimony Selenide, *Physica B: Condensed Matter* 678 (2024) 415744. <https://doi.org/10.1016/j.physb.2024.415744>
- Study of the Optical Properties of  $\text{Sb}_2(\text{Se}_{1-x}\text{S}_x)_3$  ( $x = 0-1$ ) Solid Solutions. *Materials Science in Semiconductor Processing* 144 (2022) 106571. <https://doi.org/10.1016/j.mssp.2022.106571>

ISSN 2585-6901 (PDF)  
ISBN 978-9916-80-230-4 (PDF)